SOME INVESTIGATIONS OF PHASE TRANSITIONS IN ROD-LIKE MACRO-MOLECULES AND FIBROUS GELS

Chuanpeng Sun

A DISSERTATION

in

Mechanical Engineering and Applied Mechanics

Presented to the Faculties of the University of Pennsylvania

in

Partial Fulfillment of the Requirements for the

Degree of Doctor of Philosophy

2022

Supervisor of Dissertation

Prashant K. Purohit,
Professor, Mechanical Engineering and Applied Mechanics

Graduate Group Chairperson

Jennifer R. Lukes,
Professor, Mechanical Engineering and Applied Mechanics

Dissertation Committee

Pedro Ponte Castañeda, Professor and Raymond S. Markowitz Faculty Fellow, Mechanical Engineering and Applied Mechanics
John L. Bassani, Professor, Mechanical Engineering and Applied Mechanics, Materials Science and Engineering
Prashant K. Purohit, Professor, Mechanical Engineering and Applied Mechanics

SOME INVESTIGATIONS OF PHASE TRANSITIONS IN ROD-LIKE MACRO-MOLECULES AND FIBROUS GELS

To my one and only love, my dearest Zitong.

ACKNOWLEDGEMENT

I never see myself as one of those emotional beings. Yet I cannot hide excitement of reaching this level. Looking back at the past five years, I am full of gratitude.

First of all, I acknowledge the funding for a series of works in this thesis through an NIH grant NIH R01 HL 135254. I also appreciate University of Pennsylvania and the Department of Mechanical Engineering and Applied Mechanics for providing an excellent academic experience.

This thesis and all that came along with it would not exist without the guidance of Prof. Prashant Purohit, who, as my advisor, leads me in the path of seeking unknown. I am very inspired by his wide vision, rich knowledge, and sharp mind in maths, physics, and mechanics. I am also grateful for his friendship, patience, and empathy. It is a great honor to have the 5 years working in his group.

I would like to express my deep thanks to my committee Prof. Pedro Ponte Castañeda, Prof. John Bassani, and Prof. Celia Reina, for their devoted engagement, inspiring comments, and critical questions.

I appreciate the enjoyable collaboration with Prof. John Weisel, Dr. Irina N. Chernysh, and Mr. Shenglin Huang. I also thank my other colleges and friends who provide help and give support during my study, research, and thesis writing. Particularly, I thank Dr. Dawei Song, Dr. Xiaoguai Li, Dr. ChenChen Liu, Dr. Jaspreet Singh, Dr. Russell Spiewak for the enlightening discussions. I thank Dr. Xinyu Liao, Mr. Konstantinos Garyfallogiannis, and Mr. Angelos Garsen for the assist during the pandemic.

Lastly, it is never easy traveling across the sea and pursuing a degree at the other side of the earth. None of this would have happened without the support and understanding of my family. I am extremely grateful for my parents Mr. Dekui Sun and Mrs. Hongmei Xu. I give my deepest love to my dearest Zitong Zhang.

ABSTRACT

SOME INVESTIGATIONS OF PHASE TRANSITIONS IN ROD-LIKE MACRO-MOLECULES AND FIBROUS GELS

Chuanpeng Sun

Prashant K. Purohit

Two problems pertaining to solid-solid phase transitions are presented here. First, we conduct Langevin dynamics calculations on a chain of masses and bistable springs in a viscous fluid, and extract a temperature dependent kinetic relation by observing that the dissipation at a phase boundary can be estimated by performing an energy balance. Using this kinetic relation we solve boundary value problems for a bistable bar immersed in a constant temperature bath and show that the resultant force-extension relation matches very well with the Langevin dynamics results. We estimate the force fluctuations at the pulled end of the bar due to thermal kicks from the bath by using a partition function. We also show rate dependence of hysteresis in cyclic loading of the bar arising from the stick-slip kinetics. we also extract equilibrium and non-equilibrium information from an over-damped Langevin system using fluctuation theorems. Second, we use a double-well stored energy function in a chemo-elastic model of gels to capture the existence of two phases of the network. We model cyclic compression/decompression experiments on fibrous gels and show that they exhibit propagating interfaces and hysteretic stress-strain curves that have been observed in experiments. We can capture features in the rate-dependent response of these fibrous gels without recourse to finite element calculations. We also use the model to study the rheological behavior of fibrous gels. We obtain the storage and loss modulus of fibrous gels by performing small amplitude oscillatory compression around various levels of deformation.

TABLE OF CONTENTS

LIST OF TABLES

LIST OF ILLUSTRATIONS

CHAPTER 1

Introduction

Stress-induced solid-to-solid phase transitions form a large class of phase transitions in nature. They occur in materials that can exhibit different crystal structures under different conditions (stress and temperature), and thus exist in more than one solid phase. When the stress and temperature condition changes, the material may undergo a transformation from one phase to another. In this family are a variety of materials including alloys [1, 2], polymers [3, 4] and ceramic materials [5]. Phase transitions are also observed in macromolecues [6–8], nano-materials [9, 10], and origami structures [11, 12]. Understanding the behavior of solid-to-solid transitions can facilitate the application of these materials in metallurgy, earth science, medical science, etc.

Despite its considerable potential in application, some fundamental aspects about the basic physical mechanisms of stress-induced solid–solid phase transitions remain poorly understood. They have been modeled in continuum theory by assuming a strain energy function of the form $\psi(\mathbf{F}, \theta)$ characterizing the thermoelasticity of the material. The strain energy function ψ depends on the deformation gradient tensor $\mathbf{F}$ and the absolute temperature θ. At a certain temperature θ_0, ψ is assumed to become non-convex with multiple local minima representing different states of deformation $\mathbf{F}_1$, $\mathbf{F}_2$,..etc. Each minimum corresponds to a phase (for example, austenite and martensite phases in shape-memory alloys such as NiTi) or to variants of a phase (for example, multiple variants of a tetragonal martensite phase).

The problem of an elastic bar with non-convex free energy function undergoing multi-phase deformation was first considered by Erickesn [13]. He demonstrated the importance of the one-dimensional Maxwell condition in the stability analysis. Following this analysis, a significant amount of research [14–18] was undertaken to model the stress-induced phase transitions in the continuum mechanical framework both under equilibrium and dynamic conditions. It was recognized that different phases may be separated by sharp interfaces

which can move during the deformation. It was shown that the balance laws of mass, momentum and energy cannot completely determine the evolution of the sharp interfaces, or phase boundaries; a *kinetic relation* as extra constitutive information must be supplied. The detailed form of the kinetic relation depends on the micro-scale dynamic process of the lattice transformation or molecular rearrangement.

While there is a large literature on continuum mechanical theories for solid-to-solid phase transitions, an alternative discrete approach has also been adopted in which one-dimensional chains or two-dimensional structures consisting of bi-stable elements are analyzed. Truskinovsky and collaborators made important contributions in this area, particularly in the analysis of energy landscape, energy barriers, and hysteresis. By studying the dynamics of these structures kinetic relations for a moving phase boundary can be extracted by comparing the results of impact and Riemann problems in the discrete settings with those in the continuum [19–22].

In this thesis we are particularly interested in phase transitions in macromolecules and fibrous gels.

1.0.1. Langevin dynamics of bi-stable mass-spring chains

Some rod-like macromolecules, such as DNA and coiled-coil proteins, have been observed to undergo structural transitions when subjected to large forces. For example, different phases of DNA can exist under different force and torque conditions[23] (see Fig. 1.1(a)). Double-stranded DNA can transit into two single strands under large tensile loads (> 65pN) on the molecule [24]. This transition plays an important role in DNA replication and DNA transcription. Another widely observed example (Fig. 1.1(b)) is the $\alpha-$helix to $\beta-$sheet transition in coiled-coil proteins under tensile load along the length[25]. Experiments and molecular dynamic simulations have confirmed a propagating interface between different phases during the transition. There are only a few papers in which continuum mechanical theories are used to understand these phase transitions.

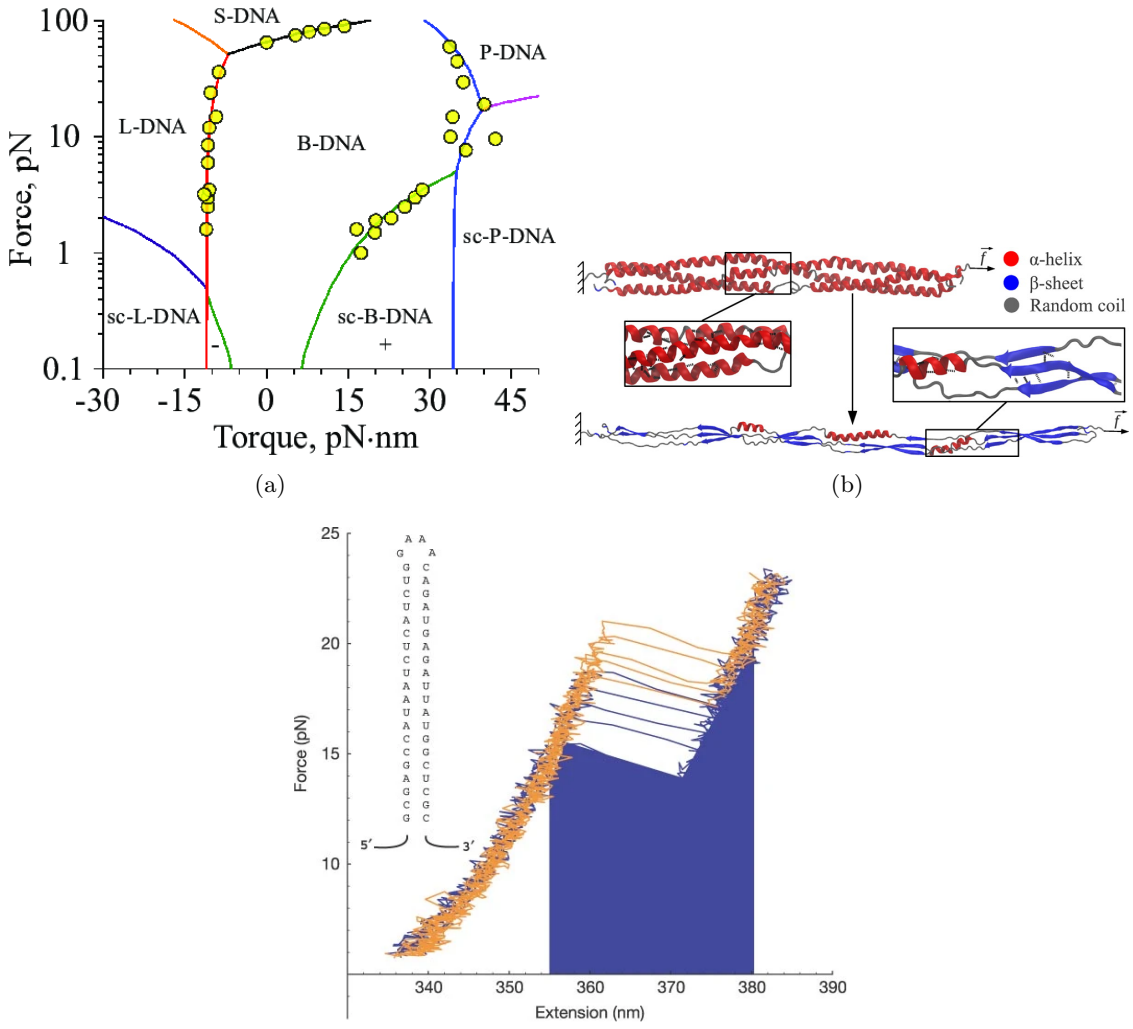

Figure 1.1: (a)DNA phase diagram under different torque and tension.[23] (b)α-helix to β-sheet transition in protein under tension. [25] (c)Unfolding and refolding force–extension curves for the RNA hairpin[26]

.

One important feature in the examples mentioned above which distinguishes them from dynamic phase transitions studied using continuum theories is that the macromolecues are in a fluid environment, and the viscous force (not inertia) and thermal fluctuations play a dominant role. An appropriate kinetic relation in this case is based on the Arrhenius law. In fact, good agreement has been shown between analytical models based on Arrhenius kinetics

and molecular dynamics simulations [27, 28]. Yet, the Arrhenius kinetics may not always be applicable to describe the evolution of the phase fractions, and therefore 'stick-slip' type kinetic laws have been proposed for phase boundary motion. Such kinetic laws are applicable for phase boundary motion through a row of imperfections[15], for propagation of a front by kink motion[29], and for phase boundary motion through a heterogeneous solid[30]. Here 'stick-slip' refers to cases in which the phase fraction evolves only when the configurational force exceeds a threshold value. Such a relation was first obtained by Atkinson and Cabrera [31] between driving force and defect velocity by considering the radiation (of energy) from a dislocation moving at constant velocity through a 1D chain of particles interacting through a periodic potential. Similar 1D lattice models with periodic potentials are also used to study nanoscale friction and it is shown how a threshold force is required for motion (as is well-known in the study of static friction) [32]. However, the role of thermal fluctuations is unclear in the kinetic law for static friction [33], and this is also true for kinetic relations for phase transition in macromolecues.

Meanwhile, the growing interest in recent years in non-equilibrium statistical mechanics could provide us with an alternative method to study the system described above, namely through the use of fluctuation theorems. These fluctuation theorems[34–37] generalize the second law of thermo-dynamics and are applicable to systems arbitrarily far from equilibrium. It has been shown by a series of works[26, 38–40] that equilibrium and non-equilibrium information can be obtained by studying the microscopic fluctuation of far from equilibrium processes. Some of these works, such as in reference[26, 38], have targeted the dynamics of macromolecues and have successfully computed free energy changes from measurements of non-equilibrium processes. For example, Collin et al. [26] justified the Crooks FT for the folding/unfolding of an RNA hairpin and an RNA three-helix junction (see Fig. 1.1(c)). This inspires us to use fluctuation theorems to extract information about phase transition from non-equilibrium processes under large thermal fluctuations. The idea is that an equality version of the second law provides another equation of motion that might obviate the need to specify the kinetic law for phase boundary motion as constitutive information. We

test this possibility by applying well-established fluctuation theorems such as the Jarzynski equality[36] and the Crooks fluctuation theorem[37] to a chain of masses and springs, including springs with bi-stable potentials.

1.0.2. Phase transitions in fibrous gels

Another class of materials of studied in this work is fibrous gels. Fibrous gels are composed of fiber networks infiltrated with fluid. Due to the interconnected fibers that form a network, these gels show the attributes of elastic solids with deformability and softness. Meanwhile, the liquid content leads to liquid-like properties of gels. Owing to their capability of absorbing large quantities of water, tissues in the human body can be regarded as biological hydrogels. In the past two decades, there has been a great deal of research applying ideas from hydrogels to areas such as tissue engineering, drug delivery, self-healing materials, biosensors, and hemostasis bandages [41–46]. The potential of broad applications has inspired advances in a nonlinear field theory of hydrogels. In this context, we are familiar with the work of Chester and Anand [47–49] whose theory is based on the kinematics of network deformation, the kinetics of water diffusion, and the thermodynamics of swelling[50, 51].

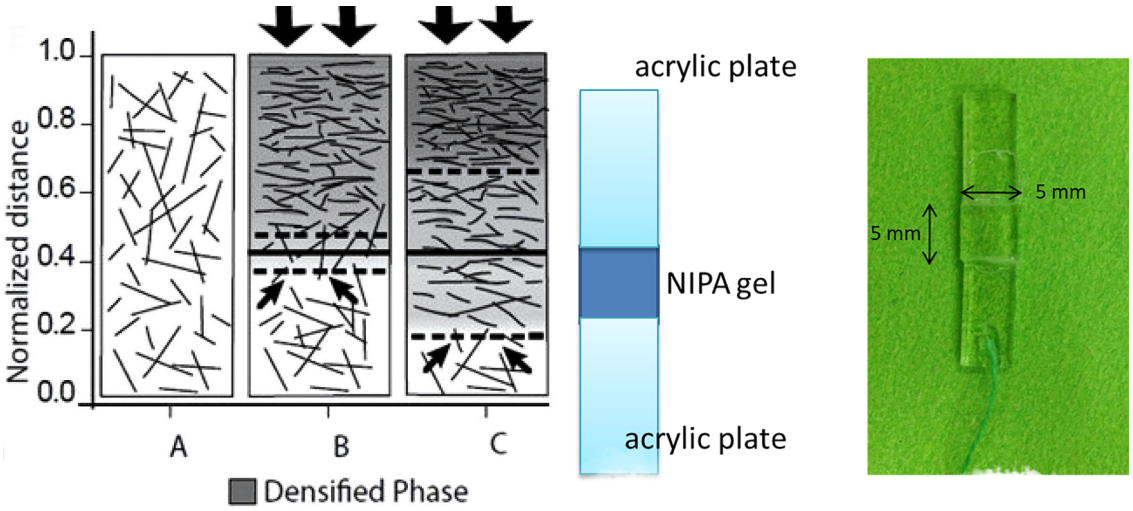

(a) (b)

Figure 1.2: (a)A schematic presentation of plasma clots with and without compression [52] showing a phase transition front. (b)Schematics of the phase transition of temperature-sensitive hydrogel triggered by uniaxial load [53].

.

Here we are particularly interested in fibrous gels in human tissues such as blood clots and cartilage [54–56]. An important feature of these gels is that the fibers buckle under compression, causing a densification of the network accompanied by a reduction in volume and release of fluid (Fig. 1.2(a)). This characteristic distinguishes them from synthetic hydrogels that deform isochorically. Experiments such as uniaxial loading tests in Fig. 1.2(b) have shown that the fiber network comprising tissues can exist in a rarefied and a densified state over a range of stresses under displacement controlled compression [52, 57]. However, the continuum chemo-elastic model of Chester and Anand [47] or Hong et al.[51] and references there-in cannot be applied directly to fibrous gels since the stored energy function of their network is based on neo-Hookean elasticity which cannot capture the buckling of fibers. A modification to the free energy function is required to capture the phase transition behavior mediated by fiber buckling.

Rheometry is a commonly used method to measure the mechanical properties of biological gels[58–60]. The storage and loss moduli can be measured by oscillation tests while biological gels are polymerized between rheometer plates. It has been shown that the storage and loss moduli changes as a function of applied compressive strain[57] of some fibrous gels decrease initially, then stay on a long plateau, and finally increase steeply as the compressive strain increases. This trend has been explained by the phase transition theory[57]. A curious observation in fibrin gels, however, is that the storage and loss moduli depend on whether a particular state of overall compressive strain is reached during loading or during unloading the sample. This observation is documented in Liang et al. [52], but it remains unresolved. In particular, if the storage and loss moduli are indeed material properties then they should not depend on how a particular state of strain is reached. We will show that material heterogeneity induced by the phase transition could be behind this observation.

1.0.3. Organization of thesis

This thesis is formatted in the following way. In chapter 2, we focus on a 'stick-slip' type kinetic law in an over-damped 1D continuum immersed in a heat bath capable of phase

transitions. We begin in section 2.2 with a review of the continuum mechanical principles for a phase boundary in a one-dimensional bar, then we review Langevin dynamics calculations on a bi-linear bi-stable mass-spring chain immersed in a heat bath. We verify that by a suitable choice of parameters in our mass-spring chain simulations we can capture the experimentally measured force-strain curves of phase changing nanowires and filamentous molecules. Next, we focus on the microscopic motion of a phase boundary in our mass-spring chains and show that plots of phase boundary position vs. time for a variety of loading rates and bath temperatures have a stair-case pattern characteristic of discrete systems. We show that the driving force computed using analytical formulae available for bilinear materials cannot be used to find a meaningful kinetic law that relates microscopic phase boundary velocity to the driving force. Fortunately, it is possible to find an averaged phase boundary velocity and a corresponding driving force using a balance of energy. The central result of this chapter appears at the end of section 2.2 and it shows that the relation between the homogenized phase boundary velocity and the driving force is of the stick-slip type and is dependent on the bath temperature. In section 2.3 we verify through Langevin dynamic simulations of our mass-spring chain that this kinetic relation can predict the final position of the phase boundary in a problem with very different initial and boundary conditions. In section 2.4 we use the kinetic relation to solve initial-boundary value problems on a 1D bar capable of phase transitions and confirm that the force-extension curve of the bar agrees quite well with those obtained from Langevin dynamics calculations on a mass-spring chain. We also show how thermal fluctuations in the force in our Langevin dynamic calculations can be quantified using statistical mechanical principles. In section 2.5 we explore the consequences of our kinetic relation on hysteresis in cyclic loading/unloading simulations on a chain, and connect to experiments that examine the temperature and loading rate dependence of hysteresis. then, we end with a brief conclusion in section 2.6.

In chapter 3, we study the application of fluctuation theorems to the over-damped 1D chain in a heat bath, as is in chapter 2. Two well-known fluctuation theorems are introduced in section 3.1. Then in section 3.2 we establish a Green-Kubo relation for Gaussian processes of

interest. In section 3.3 we present the numerical results for a mass-spring system with linear springs. The results show a perfect match with theoretical analysis lending credibility to our Langevin dynamics calculations. In section 3.4 we show the cases with phase boundary propagation and the deviation of fluctuation theorems from our numerical calculations. The causes for the deviation are discussed in section 3.5 with an outlook for future work.

In chapter 4, we adapt the continuum chemo-elastic model of elastomeric gels to fibrous gels that can exist in rarefied and densified phases at the same state of stress, and present a method to reduce the fully three-dimensional continuum theory to a one-dimensional form that can be solved without resorting to finite element calculations involving poro-elasticity. In section 4.2 we set up the continuum theory following closely the work of Chester and Anand, with modifications in the free energy function. In section 4.3 we specialize the fully three-dimensional theory to one dimension and demonstrate how it can be solved numerically to capture the hysteretic stress-strain response of fibrous gels. In section 4.4 we specialize to an axisymmetric model, which is more complex than the one-dimensional model of section 4.3, but is still numerically solvable without recourse to finite elements. Again, we show that the axisymmetric model can recover experimental observations. In section 4.5 we present experimental evidence for some key features seen in our results of sections 4.3 and 4.4, then we conclude in section 4.6.

In chapter 5, we use the same chemo-elastic continuum model introduced in chapter 4 to study the rheological behavior of fibrous gels. The continuum theory is established in section 5.2 where analytical expressions for the storage and loss modulus are given. In section 5.3 we give the numerical algorithm and two methods to obtain the storage and loss modulus. We study the effects of loading/unloading, frequency of testing, and the number of interfaces in section 5.4 by a series of numerical tests. Some experimental observations on storage and loss moduli of fibrous gels are captured by our theoretical framework, while others are not. Reasons for why some observations of loss moduli are not captured by our model are discussed. Then, we conclude in section 5.5.

In the final chapter 6 we draw the conclusion of our study.

CHAPTER 2

Stick-slip kinetics in a bistable bar immersed in a heat bath

This chapter is based on work published in [61].

2.1. Introduction

The study of mechanical behavior of macromolecules is important to understand and manipulate DNA, proteins, enzymes, etc. Some of these molecules, such as DNA and coiled-coil proteins have a rod-like structure and are known to undergo structural transitions when subjected to large forces [6–8, 62]. These structural transitions are important for the function of these molecules: for example, intermediate filaments have a coiled-coil structure and they help maintain the integrity of a cell by unfolding (a structural transition) under large forces, but coming back to their original configuration when the force is released [63, 64]. It has been observed in numerical experiments that at high strain rates, the transition proceeds by the propagation of an interface, while at low strain rates random nucleation is the main mechanism of transition [65]. One or two interfaces between different phases of DNA have been observed in single molecule experiments [66, 67], and moving interfaces between α-helix and β-sheet phases of coiled-coils have been observed in molecular dynamic simulations [27, 68], although the dicreteness at the nano- scale makes it difficult to define a sharp interface [69, 70] as assumed in some continuum theories. We note here that both ds-DNA and α-helical coiled-coils are double stranded molecules; when these undergo structural transitions the new phase may have both strands bonded to each other (through hydrogen bonds, for example) or not. Our analysis in this paper is applicable to the case when the two strands are bonded, as in the B-DNA to S-DNA transition in dsDNA [66, 71] and the α-helix to β-sheet transition in coiled-coils[27], both of which occur when the respective molecules are loaded in tension along the length. Our analysis may not be applicable if the strands are not bonded to each other (as in a B-DNA to single-stranded DNA transition [66, 71], or if the loading applied to cause the structural transition is of shear type[72].

One way to study phase transitions in long molecules is to use continuum theory. To do so, the macromolecule is modeled as a 1D continuum with an energy storage function that has multiple wells representing different phases which may be separated in the continuum by propagating interfaces[73, 74]. Such interfaces have been observed in phase change nanowires [75] and in some macromolecules as mentioned above. When the balance laws of mass, momentum and energy are applied to this continuum it is found that they are not sufficient to fully describe the propagation of phase boundaries; an additional kinetic relation is required to close the equations and usually must be supplied as constitutive information [17]. The choice of an appropriate kinetic relation has been the subject of much research. Truskinovsky and Vainchtein [19] have analytically derived a kinetic relation for a lattice model in which inertia forces drive the phase transition, and this kinetic relation has been verified numerically by Zhao and Purohit [76]. Zhao and Purohit [76] have also shown that the kinetic relation is temperature dependent, at least for low temperatures, in a solid in which inertia forces are dominant and damping is small. However, this kinetic relation cannot be applied to macromolecules since inertia forces are negiligible for macromolecules immersed in water. Instead, the viscous force due to surrounding fluid and thermal fluctuations are dominant in structural transitions of macromolecules. Hamiltonian dynamic simulations of a bi-stable chain have been carried out by Efendiev and Truskinovsky [20] with the objective of studying its thermalization and latent heat release during phase transitions. They study the equilibrium response of the chain and compute the partition function which is utilized to calculate free energies. They do not extract a kinetic relation from their simulations because they do not see phase boundaries propagating in an organized fashion unless next-to-nearest-neighbor interactions are added. Benichou and Givli [77, 78] consider overdamped dynamics of a chain with tri-linear springs and show that a single non-dimensional quantity that captures the competition between loading rate, temperature and energy barriers can predict the amount of hysteresis under various conditions. These authors also do not comment on the kinetic relation for propagating phase boundaries in the chain, and furthermore they confine their analysis to situations in which the damping

force due to fluid viscosity in the heat bath is small. Finally, a recent study by Caruel and Truskinovsky [21] examines how a micromechanical device relying on 'snap-through' or bistability can retain its functionality in an environment dominated by fluctuations by using cooperativity of several degrees of freedom. They analyze the statistical mechanics of a parallel bundle of bistable elements and are hence not concerned with propagating phase boundaries.

An appropriate kinetic relation for phase transitions in an overdamped thermal environment is based on the Arrhenius law [17]. Indeed, analytical models of structural transitions in macromolecules based on Arrhenius kinetics have been shown to agree with molecular dynamic simulations over several decades of strain-rates [27, 28]. Arrhenius kinetics also predicts the strain-rate dependence of the plateau force in a structural transition in macromolecules [73]. More recently, Arrhenius kinetics was applied to a 1D analytical model of grain boundary motion in a solid and it was shown that it predicts the evolution of stresses in a molecular dynamic simulation without any fitting parameters [79]. Yet, Arrhenius kinetics may not always be appropriate to describe the evolution of phase fractions. In a recent experiment Dittmore and Neuman [80] found that the transition from straight DNA to plectonemic DNA in a single molecule tension-torsion experiment proceeds in a jerky fashion characteristic of frictional behavior [81]. Clearly, this cannot be described within an Arrhenius kinetic law, so 'stick-slip' type kinetic laws have been proposed that have been derived for phase boundary motion through a row of imperfections [15], for propagation of a front by kink motion [29], and for phase boundary motion through a heterogeneous solid [30]. By 'stick-slip' we mean that the phase fraction evolves only when the driving force exceeds a threshold value as in Bingham type visco-elastic fluid [82, 83]. In a different context, Atkinson and Cabrera [31] obtained a relation between driving force and defect velocity by considering the radiation (of energy) from a dislocation moving at constant velocity through a 1D chain of particles interacting through a periodic potential. They computed a threshold force to start the defect moving, effectively deriving a stick-slip type kinetic law. Similar 1D lattice models [32] with a periodic potential are also used to study nanoscale friction (as oc-

curs when an atomic force microscope tip is dragged over a crystalline solid) and it is shown how a threshold force is required for motion as is well-known in the study of static friction. However, in these papers temperature and thermal fluctuations play no role. There are models of grain-boundary motion in which temperature dependent stick-slip kinetics have been explained [84], but it is not clear how these models are connected to phase boundary propagation in 1D continua, such as, the biological macromolecules mentioned earlier in this paper. Stick-slip type evolution of phase fraction in biological macromolecules was discussed in detail within a continuum theory in a recent paper by De Tommasi *et al.* [33]. The authors focused in this paper on macromolecules whose force-extension relation displays a saw-tooth pattern characterized by discrete events, and showed how a continuum limit leads to a force-extension relation with a plateau characterizing the folding/unfolding transition of the macromolecule. They also put their theory in the context of flow-rules used in plasticity [85] and explained how a theshold driving force must be reached for the phase fraction (treated as an internal variable in [83]) to evolve. If there is a threshold driving force for the evolution of phase fraction then there is hysteresis even in quasistatic loading/unloading of a phase-changing bar [17]. As a result, hysteresis in the model of De Tommasi *et al.* has both a rate-independent and a rate-dependent component. However, viscous drag due to the fluid bath surrounding a molecule and temperature dependence of phase boundary kinetices are not discussed in [33] either.

We show in this paper that stick-slip type kinetics can arise in an overdamped 1D continuum capable of phase transitions. A brief outline of our approach that led to this result follows. In section 2.2 we begin with a review of the continuum mechanical principles for a phase boundary in a one-dimensional bar, then we review Langevin dynamics calculations on a bilinear bi-stable mass-spring chain immersed in a heat bath. It has been shown in several papers in the literature that features in the evolution of phase transitions in 1D continua can be captured quite well using mass-spring chain models [17, 76, 86]. We verify that by a suitable choice of parameters in our mass-spring chain simulations we can capture the experimentally measured force-strain curves of phase changing nanowires and filamentous

molecules. Next, we focus on the microscopic motion of a phase boundary in our mass-spring chains and show that plots of phase boundary position vs. time for a variety of loading rates and bath temperatures have a stair-case pattern characteristic of discrete systems. We show that the driving force computed using analytical formulae available for bilinear materials cannot be used to find a meaningful kinetic law that relates microscopic phase boundary velocity to the driving force. Nevertheless, it is possible to find a homogenized (or average) phase boundary velocity and a corresponding driving force using a balance of energy. The central result of our paper appears at the end of section 2.2 and it shows that the relation between the homogenized phase boundary velocity and the driving force is of the stick-slip type and is dependent on the bath temperature. In section 2.3 we verify through Langevin dynamic simulations of our mass-spring chain that this kinetic relation can predict the final position of the phase boundary in a problem with very different initial and boundary conditions. In section 2.4 we use the kinetic relation to solve initial-boundary value problems on a 1D bar capable of phase transitions and confirm that the force-extension curve of the bar agrees quite well with those obtained from Langevin dynamics calculations on a mass-spring chain (in which no kinetic relation was prescribed in the first place). We also show how thermal fluctuations in the force in our Langevin dynamic calculations can be quantified using statistical mechanical principles. In section 2.5 we explore the consequences of our kinetic relation on hysteresis in cyclic loading/unloading simulations on a chain, and connect to experiments that examine the temperature and loading rate dependence of hysteresis; then, we end with a brief conclusion in section 2.6.

2.2. Study of the kinetic relation

We begin with a brief review of the evolution of phase transitions in 1-D continua and show that it can be mimicked in simulations of mass-spring chains with bistable springs. Most treatments of 1-D continua capable of phase transitions ignore viscous drag forces which are relevant to macromolecules, but we account for these drag forces and connect them to the drag imposed by the fluid bath in our Langevin dynamic simulations of a mass-spring chain. Our central result in this section is the deduction of a relation between average phase

boundary velocity in a bi-stable chain with the driving force acting on it.

2.2.1. Modeling of a rod-like molecule

We follow the development in Abeyaratne and Knowles [17]. Consider a 1-D bar occupying an interval $[0, L]$ in the reference configuration. The displacement in the deformed configuration at x at time t is denoted by $u(x,t)$. The corresponding velocity is $v(x,t) = \dot{u} = \frac{\partial u}{\partial t}$ and the strain is given by $\gamma(x,t) = u_x = \frac{\partial u}{\partial x}$. Let $\sigma(x,t)$ denote the force in the bar. Momentum balance requires a portion of the bar in $[x_1, x_2]$ to satisfy:

$$\sigma(x_2,t) - \sigma(x_1,t) + \int_{x_1}^{x_2} \rho b dx = \frac{d}{dt}\int_{x_1}^{x_2} \rho v(x,t) dx, \tag{2.1}$$

where b is the body force and ρ is a mass per unit length in the reference configuration, which is assumed a constant in our model. If v, γ and σ are smooth enough (differentiable), then the momentum balance can be re-written as:

$$\frac{\partial \sigma}{\partial x} + \rho b = \rho \frac{\partial v}{\partial t}. \tag{2.2}$$

Also the differentiability of v and γ requires that:

$$\frac{\partial v}{\partial x} = \frac{\partial \gamma}{\partial t}. \tag{2.3}$$

These two equations together with the constitutive relation,

$$\sigma(\gamma) = W'(\gamma), \tag{2.4}$$

will close the system in the absence of any discontinuity. Here, $W(\gamma)$ denotes strain energy per unit reference length as a function of strain γ.

Since our main interest is in the dynamics of a phase boundary (the moving interface separating two phases), we need to relax the continuity of some quantities. Here the displacement u is still assumed to be continuous, but $\dot{u}$, u_x and σ may have isolated discontinuities.

Assume there exists only one discontinuity at $s(t)$ at time t in the reference configuration $0 \leq s(t) \leq L$. The corresponding jump conditions at the discontinuity are

$$\begin{aligned} [|\sigma|] &= -\rho \dot{s}[|v|], \\ [|v|] &= -\dot{s}[|\gamma|]. \end{aligned} \tag{2.5}$$

Here $[|\phi|] = \phi_+ - \phi_- = \phi(s(t)^+, t) - \phi(s(t)^-, t)$ and $\dot{s}$ is the speed of the discontinuity in the reference configuration.

For a portion of the bar lying in the reference configuration between x_1 and x_2 the dissipation rate, which is defined as the difference between the rate of work done by the external forces acting on the bar and the rate of change of total mechanical energy within it, can be written as:

$$D(t) = \sigma v|_{x_1}^{x_2} - \frac{d}{dt}\int_{x_1}^{x_2} (\frac{1}{2}\rho v^2 + W(\gamma))dx. \tag{2.6}$$

Under the assumption that there is only one discontinuity in the bar and making use of the field equations and jump conditions, one can show that

$$D(t) = f(t)\dot{s}(t), \tag{2.7}$$

where $f(t)$ is the driving force acting on the discontinuity. Note that the second law of thermodynamics requires $D(t) \geq 0$. The driving force is determined by the strains immediately ahead and behind the phase boundary:

$$f = \int_{\gamma^-}^{\gamma^+} \sigma(\gamma)d\gamma - \frac{1}{2}(\sigma(\gamma^+) + \sigma(\gamma^-))(\gamma^+ - \gamma^-). \tag{2.8}$$

In order for the discontinuity to be a phase boundary the force σ cannot be a monotonically increasing function of strain γ. For simplicity, assume the constitutive relation of the bar is bi-linear:

$$\sigma(\gamma) = \begin{cases} E\gamma, & \gamma < \gamma_c, \\ E(\gamma - \gamma_t), & \gamma \geq \gamma_c. \end{cases} \tag{2.9}$$

Also, for simplicity, assume $\gamma_c = \frac{\gamma_t}{2}$, then the stored energy landscape is a double-well:

$$W = \begin{cases} \frac{1}{2}E\gamma^2, & \gamma < \gamma_c, \\ \frac{1}{2}E(\gamma - \gamma_t)^2, & \gamma \geq \gamma_c. \end{cases} \tag{2.10}$$

The system is stable in each well, and thus we call $\gamma < \gamma_c$ low strain phase, and $\gamma \geq \gamma_c$ high strain phase. By substituting the constitutive relation into the definition of driving force, one can find the following explicit form of driving force for a simple double-well material:

$$f = \frac{1}{2}E\gamma_t(\gamma^+ + \gamma^- - \gamma_t) \tag{2.11}$$

Our goal is to simulate a discrete version of a bar with the constitutive relation in eqn.(2.9) immersed in a constant temperature bath. We will perform impact experiments on the bar and follow the phase boundaries with the objective of getting an isothermal kinetic relation.

2.2.2. Constant temperature bath: Langevin dynamics

In order to realize a bar immersed in a constant temperature bath we simulate a mass-spring chain using Langevin dynamics [76]. Suppose we have $N + 1$ masses and interaction exists between only the nearest neighbors; the masses are then connected by N springs. The potential energy of the springs is double-welled,

$$W = \begin{cases} \frac{1}{2}k(x_i - a_0)^2, & x < x_c, \\ \frac{1}{2}k(x_i - a_t)^2, & x \geq x_c, \end{cases} \tag{2.12}$$

where $x_i = u_{i+1} - u_i$ is the length of the i-th spring, $x_c = \frac{1}{2}(a_0 + a_t)$ for simplicity. We assume the chain is immersed in fluid with fixed temperature T. The equations of motion for the masses are:

$$m\ddot{u}_i = -\nu\dot{u}_i - \frac{\partial\phi}{\partial u_i} + F_i(t). \tag{2.13}$$

The total potential energy of the chain is given by $\phi = \sum_{i=1}^{N} W(x_i)$. ν denotes the drag coefficient due to the fluid. For a rod of length l and radius r in a Newtonian fluid with viscosity μ, the corresponding drag coefficient is given by $d_w = \frac{2\pi\mu}{\log(l/r)-0.8}$. This formula is valid when $l/r > 10$ and should work well for long rod-like DNA and protein molecules [73]. For mass-spring representation of a bar, ν is such that the drag force on a mass is equivalent to the drag force on the interval of $[x_i, x_i + a_0]$ of the bar, $\nu = d_w a_0$ where a_0 is the distance between two masses in the reference configuration. The force $F_i(t)$ denotes a time-dependent random force exerted by the bath on each mass due to thermal fluctuation, which averages to 0 and is assumed to be delta-function correlated in time [87]:

$$\langle F_i(t) \rangle = 0, \quad \langle F_i(t) F_i(t') \rangle = 2\nu k_B T \delta(t - t'), \tag{2.14}$$

where k_B is the Boltzmann constant, T is the absolute temperature and $\langle \cdot \rangle$ denotes ensemble average.

We use a symplectic method to integrate eqn.(2.13) [76, 88]:

$$\begin{aligned}
v_{1,i,k} &= g(\frac{\tau}{2}; v_{i,k}), \\
u_{1,i,k} &= u_{i,k} + \frac{\tau}{2} v_{1,i,k}, \\
v_{2,k} &= v_{1,i,k} + \tau \frac{F(x_{1,i+1,k}, x_{1,i,k})}{m} + \frac{\tau^{1/2}}{m} \sigma \xi, \\
v_{i,k+1} &= g(\frac{\tau}{2}; v_{2,i,k}), \\
u_{i,k+1} &= u_{1,i,k} + \frac{\tau}{2} v_{2,i,k}, ,
\end{aligned} \tag{2.15}$$

where τ is the time step, k denotes the k-th time step, and i denotes the i-th particle, $g(t, v) = ve^{-\nu t/m}$, $\sigma = \sqrt{2\nu k_B T}$ and ξ is a Gaussian random number with mean 0 and variance 1. The above numerical scheme remains valid for $T = 0$ when thermal fluctuation is not considered or $\nu = 0$ which corresponds to zero fluid drag. In fact, Zhao and Purohit [76] had used this scheme for an isothermal chain in which inertia forces played a significant role, but damping was small. The temperature T in those simulations was small enough

that although thermal fluctuations were apparent the chain dynamics were similar to one with $T = 0$. As a result, the inferred kinetic relation was of a form derived analytically for a purely mechanical chain [19], but it showed a weak dependence on temperature [76]. In this paper we have the opposite situation in which the inertia forces are negligible and damping is significant as is the case for a long biomolecule immersed in water.

In our simulations the chain is fixed at one end ($i = 1$) and stretched at a constant rate v_p at the other end ($i = N + 1$). Such a case corresponds to the impact problem in a continuum bar, where a constant velocity is applied to a semi-infinite bar. It has been shown in molecular simulations [68] that the springs at the moving end first transit into the high strain phase, and a phase boundary appears at that end, then propagates towards the other end. We wish to obtain the kinetic relation for such a phase boundary.

2.2.3. Non-dimensionalization

Here we choose the initial length of springs a_0, the stiffness of the springs k, and the mass m as the independent variables. These three variables are all internal properties of the mass-spring chain. Once the material is chosen, the characteristic variables are determined. Let variables for the bar be the characteristic parameters:

$$\begin{aligned}
\bar{c} &= a_0\sqrt{\frac{k}{m}} && \text{(characteristic velocity)},\\
\bar{t} &= \sqrt{\frac{m}{k}} && \text{(characteristic time)},\\
\bar{\nu} &= \sqrt{km} && \text{(characteristic viscosity)},\\
\bar{E} &= k{a_0}^2 && \text{(characteristic energy)},\\
\bar{T} &= \frac{k{a_0}^2}{k_B} && \text{(characteristic temperature)}.
\end{aligned} \tag{2.16}$$

We notice that the characteristic velocity is in fact the sonic wave speed of the mass-spring chain, $c = a_0\sqrt{k/m}$. The corresponding dimensionless variables (variables with $*$) are given by:

$$u_i^* = \frac{u_i}{a_0}, \quad \tau^* = \frac{\tau}{\bar{t}}, \quad v_p^* = \frac{v_p}{c}, \quad \nu^* = \frac{\nu}{\bar{\nu}}, \quad T^* = \frac{T}{\bar{T}}, \quad W^* = \frac{W}{\bar{E}}. \tag{2.17}$$

It can be easily shown that these dimensionless variables satisfy the same governing equations and boundary conditions as the original equations. For example, the non-dimensional Langevin equation is:

$$\ddot{u_i^*} = -\nu^* \dot{u_i^*} - \frac{\partial \phi^*}{\partial u_i^*} + F_i^*(t).$$

Since our interest is in long molecules, consider a coiled-coil protein [89]. The corresponding characteristic variables are:

$$\bar{a_0} = 2 \times 10^{-10} m, \qquad \bar{k} = 5N/m, \qquad \bar{m} = 4.3 \times 10^{-25} Kg.$$

These parameters are obtained from the force-strain relation, the length and the linear density of a coiled-coil protein [89]. The non-dimensional double-well potential is assumed to be (this may not be characteristic of a coiled-coil protein):

$$W^* = \begin{cases} \frac{1}{2}(x_i^* - 1)^2, & x^* < 2.5, \\ \frac{1}{2}(x_i^* - 4)^2, & x^* \geq 2.5. \end{cases}$$

The ratio of length l and radius r is approximated as 20 [89]. We ignore the effect of temperature on the viscosity of the fluid and use the viscosity of water at $300K$ and 1 atm, $\nu = 1.01 \times 10^{-3}$ [90]. The non-dimensional viscosity is $\nu^* = 0.400$. We used these parameters to carry out a simulation in which a mass-spring chain was pulled at a constant velocity. The results are plotted in Fig. 2.1 for two pulling velocities. We see the same mechanical behavior as was observed in experiments and molecular dynamic simulations [28, 89] on coiled-coil proteins. In particular, there are three regions of the force-strain curve – a low strain region in which all springs are in the low strain well, a high strain region in which all springs are in the high strain well and a plateau region in which some springs are in the low strain well and others in the high strain well. In particular, the slope of the plateau region increases with increasing pulling velocity as observed in molecular dynamic simulations [28] as well as in experiments [64]. Note also that there is significant fluctuation in the force F_e

measured at the end being pulled. We will quantify these fluctuations later in the paper.

Although we will mostly confine ourselves to the non-dimensional spring paramaters chosen above while changing the pulling velocity v_p and bath temperature T, we emphasize that our mass-spring model can capture force-strain plots with plateaus in various materials. To demonstrate this we modify our energy potential slightly as shown below to account for different well depths in the unloaded state:

$$W^* = \begin{cases} \frac{1}{2}k^*(x_i^* - x_0^*)^2, & x^* < x_c^*, \\ \frac{1}{2}k^*(x_i^* - x_t^*)^2 + W_t^*, & x^* \geq x_c^*. \end{cases}$$

We set $k^* = 120$, $x_0^* = 1$, $x_c^* = 1.005$, $x_t^* = 1.0055$, and $W_t^* = 2.97 \times 10^{-4}$ and show in Fig. 2.1(c) that we can match the experimental stress-strain curves of Guo *et al.* for vanadium oxide nanowires [75]. The experimental stress-strain curves were obtained by *in situ* uniaxial tension of these nanowires in a transmission electron microscope. Guo *et al.* show by using X-ray diffraction techniques that there is co-existence of two phases in the plateau region of the force-strain curve, but there is only one phase in the low-strain region, hence establishing that a phase transition is responsible for the characteristic form of their stress-strain curve. In our simulations we used room temperature, a low drag coefficient, and a very slow pulling speed to mimic the experimental conditions of Guo *et al.* [75]. The output of our mass-spring simulations is a force at the pulled end but it can be converted to a stress since the cross-sectional area of the nanowires used in [75] can be inferred from their experimental daata. Next, we set $k^* = 1$, $x_0^* = 1$, $x_c^* = 1.2$, $x_t^* = 1.9$, and $W_t^* = -0.225$ and show in Fig. 2.1(d) that we can match experimental force-strain curves of Block *et al.* for vimentin intermediate filaments [64]. In this figure we show that the same set of parameters can reproduce the experimental data for two different pulling rates. The experiments of Block *et al.* are performed using optical traps within a micro-fluidic device and it is shown that an α-helix to β-sheet transition occurs during pulling. In our simulations we used room temperature and drag coefficient appropriate for a filament immersed in water.

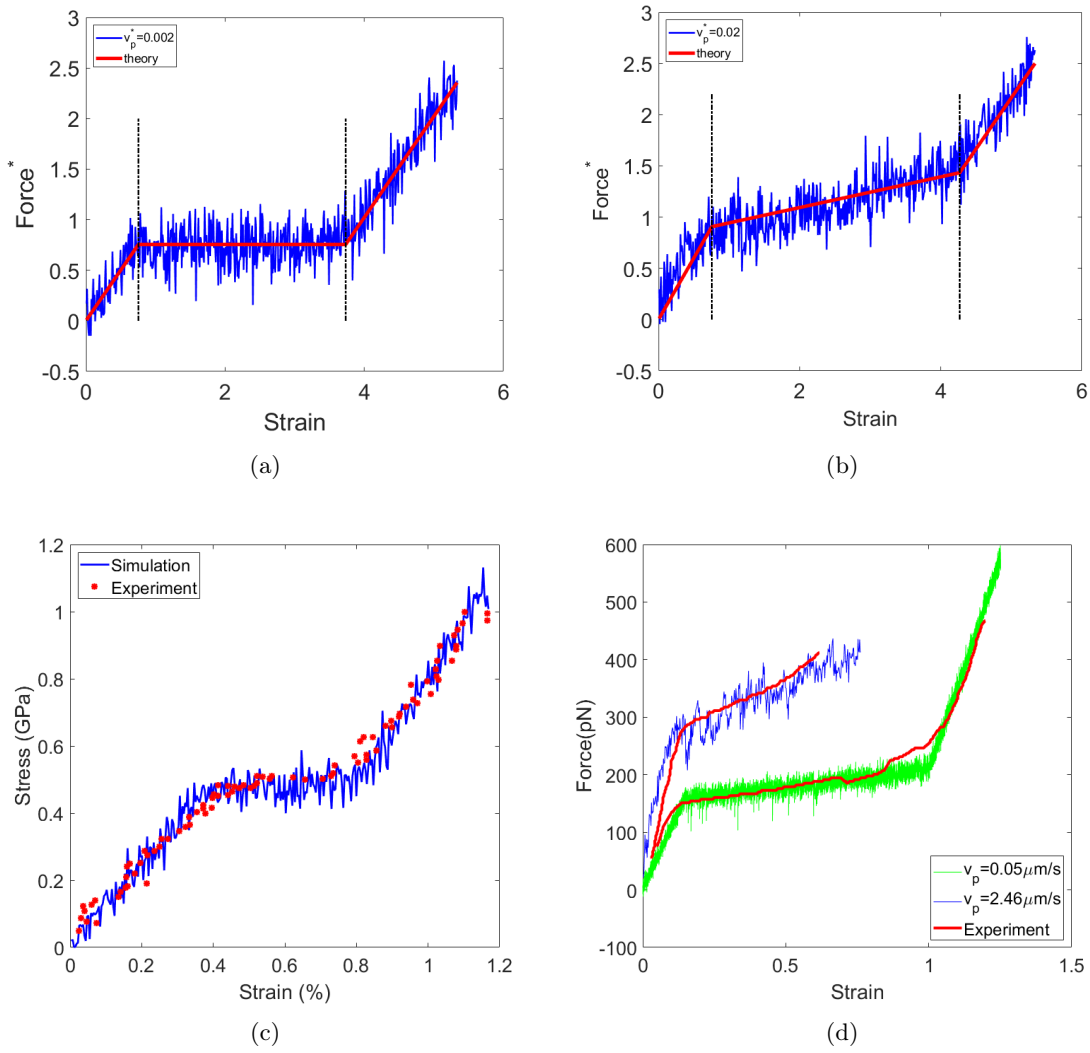

Figure 2.1: The force-strain relation for a chain with $N = 100$ at pulling rate of (a) $v_p^* = 0.002$ and (b) $v_p^* = 0.02$. We find three regions demarcated by dashed vertical lines above: a linearly increasing region in low strain phase, a plateau denoting phase transition process, and a second linearly increasing region in high strain phase. Such behaviors have been observed in experiments and molecular dynamic simulations. There is significant fluctuation in the force measured at the Nth mass. (c) Stress-strain curve of vanadium oxide sample undergoing phase transition (blue dots) [75] matched by our Langevin dynamics simulation of a mass-spring chain (red curve) with appropriate parameters. (d) Force-strain curves at two different pulling speeds of vimentin intermediate filaments immersed in fluid [64] matched by our Langevin dynamic simulations with appropriate parameters. We fit the parameters of the energy landscape (green curve) to the experimental data (red curve) at the lower pulling speed. Then, we change to higher pulling speed and show that our Langevin dynamics simulations (blue curve) match with experimental data (red curve). The experimental curves in this figure are averages of multiple pulls (see [64]), so fluctuations are not apparent. Here the strain $\gamma = \frac{L-L_0}{L_0}$ is the ratio of the extension $L - L_0$ and the initial length L_0 of the whole chain.

Having shown the versatitility of our mass-spring simulations we turn our attention back to phase boundary propagation in the next section.

2.2.4. Homogenized phase boundary velocity

In our simulations we find a single propagating phase boundary when pulling velocity v_p is sufficiently high. Although we focus here on situations with a single propagating boundary, we acknowledge that in both experiments and simulations one may also find multiple phase boundaries[28, 66, 68]. In particular, if non-nearest neighbor interactions between masses are included [91, 92] then the number of phase boundaries is determined by the boundary conditions as shown for biomolecules in [93]. In our simulations multiple phase boundaries are seen at low pulling velocities as shown in section 3, but we focus on one propagating phase boundary here because we want to deduce the kinetic relation for it. We have found that the average (or homogenized) velocity $\dot{s}$ of this phase boundary is nearly constant throughout the simulation if the pulling velocity v_p is constant. There are small fluctuations about this average. To see this we refer the reader to Fig. 2.2(a) in which we plot the phase boundary position for three combinations of pulling velocity v_P and bath temperature T. In each case we find a 'stair-case pattern' for the phase boundary position as a function of time. The phase boundary moves in discrete steps which are not all of the same length. This may be understood by considering the following three time scales – (a) the time scale $\tau_{well} = \sqrt{\frac{m}{k}}$ for in-well minimization, (b) the time scale $\tau_p = \frac{a_0}{v_p}$ associated with the loading, and (c) the time scale $\tau_{bar} = \frac{\pi m}{k}[\frac{\nu}{m} + \sqrt{(\frac{\nu}{m})^2 + 4\frac{k}{m}}]e^{\frac{Q}{k_B T}}$ associated with crossing the energy barrier Q [94]. In our case $\tau_{well} \approx 1$, $\tau_p \approx 10$ and $\tau_{bar} \approx 10^{10}$. Since, τ_{bar} is much longer than the other two time scales our hypothesis is that the phase boundary jumps from the current mass to the next when the force in the spring ahead of that mass becomes large enough to make the barrier comparable to $k_B T$. If τ_{bar} was not too large compared to τ_p then barrier crossing would occur more easily as the chain is pulled and Arrhenius kinetics would be appropriate. This is not the case for the parameters in our mass-spring chain in which the energy barrier separating the two wells is high, hence the mass oscillates inside a well until the energy landscape is tilted sufficiently by the loading to cause a jump. This is why the

microscopic motion of the phase boundary appears like a stair-case pattern. Nevertheless, the dashed lines through each stair-case show that there is a 'homogenized' constant velocity of the phase boundary as it moves from one end of the chain to the other. Let t_1 denote the time the phase boundary appears and t_2 the time it reaches the other end and vanishes, then by definition, the homogenized phase boundary velocity is given by

$$\dot{s} = \frac{Na_0}{t_2 - t_1}. \tag{2.18}$$

There are multiple ways for finding the driving force. Eqn.(2.11) gives an explicit form of driving force for double-welled potentials, where γ^+ and γ^- denote the strain right behind and right in front of the phase boundary, respectively. Here, the strain is defined as $\gamma_i = \frac{x_i}{a_0}$. However, in practice, we find it difficult to evaluate the exact value of the two strains due to the inevitable thermal fluctuation from the surrounding heat bath and possible oscillation of the springs. In spite of this difficulty, the driving force evaluated using eqn.(2.11) is plotted as a function of time for each of three combinations of pulling velocity and bath temperature used Fig. 2.2(a) in the three panels Fig. 2.2(b,c,d). These plots show that the driving force obtained using eqn.(2.11) cannot yiled a meaningful kinetic law if plotted together with instantaneous phase boundary velocity. However, the driving force in these plots seems to be fluctuating around a constant value suggesting that it may be possible to evaluate an average driving force that is conjugate to the homogenized phase boundary velocity using a different method. The method we use here is based on energy balance which gives the dashed lines in Fig. 2.2(b,c,d) and is explained below.

2.2.5. Energy balance method

Consider a bar occupying an interval of $[0, L]$ in reference configuration. At time t_s, an external force F_e is applied to the bar such that the $x = L$ end is moving at a constant rate v_p in the deformed configuration while the $x = 0$ end is fixed. At time t_e we stop pulling so

that both ends are fixed. Then the following energy balance holds:

$$W_e = \Delta K_m + Q, \tag{2.19}$$

where W_e denotes the work input to the system due to F_e, ΔK_m is the change in mechanical energy of the bar and Q is the total dissipation over time interval (t_s, t_e). For the mass-spring chain, applying Newton's law on the $(N+1)$-th mass, we get

$$F_e = \nu v_p + \sigma_N,$$

where σ_N is the tension in the N-th spring. Therefore, the total work done on the system is given by the integration of the force F_e with respect to displacement:

$$W_e = \int_{t_s}^{t_e} F_e v_p dt = \int_{t_s}^{t_e} (\nu v_p^2 + \sigma_N v_p) dt. \tag{2.20}$$

We use the trapezoidal rule to do the numerical integration. Let j denote the j-th time step, then the total external work is the summation of work done for each step:

$$W_e = \sum_j \tau v_p (\frac{\sigma_{N,j-1} + \sigma_{N,j}}{2} + \nu v_p).$$

The mechanical energy is the sum of the kinetic energy of all masses and potential energy of all springs:

$$\Delta K_m = \{\sum_{i=1}^{N+1} \frac{1}{2} m v_i^2 + \sum_{i=1}^{N} W(x_i)\}|_{t_s}^{t_e}. \tag{2.21}$$

The total dissipation involves two parts: (1) dissipation due to propagation of the phase boundary, and (2) dissipation due to the drag of the fluid. The dissipation rate for part (1) is given by eqn.(2.7), under the assumption that there is only one phase boundary propagating. Thus, the total dissipation due to phase boundary is

$$D_p = \int_{t_s}^{t_e} f(t)\dot{s}(t) dt.$$

If the phase boundary velocity and the driving force are constant, the above equation can be simplified to

$$D_p = fL, \tag{2.22}$$

where L is the length of the bar in the reference configuration. The dissipation due to viscous drag is given by the following:

$$D_v = \sum_i \int_{t_s}^{t_e} (\nu \dot{u}_i^2 - F_i \dot{u}_i) dt. \tag{2.23}$$

Note that the random force must be included in the equation above because thermal fluctuation and viscous dissipation are intimately connected through the fluctuation-dissipation theorem[87]. To see how, consider the following decomposition of velocity $\dot{u}_i = \langle \dot{u}_i \rangle + \hat{\dot{u}}_i$, where $\langle \cdot \rangle$ denotes the ensemble average and $\langle \hat{\dot{u}}_i \rangle = 0$. Taking the ensemble average of eqn.(2.23), we have:

$$\begin{aligned} \langle D_v \rangle &= \sum_i \int_{t_s}^{t_e} (\nu \langle \dot{u}_i^2 \rangle - \langle F_i \dot{u}_i \rangle) dt \\ &= \sum_i \int_{t_s}^{t_e} (\nu \langle \dot{u}_i \rangle^2 + \nu \langle \hat{\dot{u}}_i^2 \rangle - \langle F_i \hat{\dot{u}}_i \rangle) dt \\ &= \sum_i \int_{t_s}^{t_e} \nu \langle \dot{u}_i \rangle^2 dt. \end{aligned} \tag{2.24}$$

The last step assumes an isothermal system, for which $\nu \langle \hat{\dot{u}}_i^2 \rangle - \langle F_i \hat{\dot{u}}_i \rangle = 0$, from the fluctuation-dissipation theorem in Langevin dynamics for free particles and harmonic oscillators [87]. Finally, the driving force can be obtained from the energy balance through:

$$f = \frac{1}{L}(W_e - \langle D_v \rangle - \langle \Delta K_m \rangle). \tag{2.25}$$

Here D_v denotes the work done by viscous forces and is given by eqn.(2.24).

Our method of computing the driving force f using eqn.(2.25) is reminiscent of an energy method used by Abeyaratne, Chu and James (ACJ)[14]. In the problem studied by ACJ the

energy of the entire system $E(s)$ is considered and the driving force is given by $f = -\frac{\partial E}{\partial s}$. The energy of their system consists of elastic energy in the bar, the energy of a dead loading device, the interfacial energy of the phase boundary and the energy of the imperfections. Then, the driving force is obtained by determining how much this total energy changes when s changes by an infinitesimal amount. In eqn.(2.25), we consider the energy of all masses and springs, but unlike the stress σ in ACJ which is constant all over the bar, the force in our springs is not the same in all springs due to viscous drag. Also, viscous drag leads to a dissipation other than that caused by phase boundary motion (which was the only dissipating mechanism in ACJ). Therefore, we subtract out the energy dissipated due to viscous drag D_v before computing how much the energy of the masses and springs changed as the phase boundary moved in eqn.(2.25). We let the phase boundary move the entire length L of the chain because we show in Fig. 2.2 that the plot of phase boundary position vs. time for several combinations of bath temperature and pulling speed shows a stair-case pattern suggesting that the microscopic phase boundary velocity fluctuates around a constant (homogenized) value and that the driving force computed using eqn.(2.11) also fluctuates around a constant (homogenized) value as the phase boundary traverses the entire chain. Here we caution the reader that although the microscopic motion of the phase boundary looks like a 'stick-slip' motion due to the discreteness of the chain, we use the term 'stick-slip' in this paper to refer to the macroscopic kinetic law relating a homogenized driving force to a homogenized phase boundary velocity, which is like a Bingham type viscoelastic fluid in which a threshold driving force must be reached for time evolution to occur.

Before we start our computations to get a kinetic relation, we need to first show that the energy balance method of eqn.(2.25) gives reasonable results for our mass-spring chain. To verify the energy balance method, we first consider the impact problem of a mass-spring chain with linear springs. In this case there is no phase boundary and the corresponding energy balance is given by

$$W_e - \langle D_v \rangle - \langle \Delta K_m \rangle = 0.$$

Table 2.1: Enegy balance for a chain of linear springs.

Temperature	pulling velocity	ΔK_m $\times 10^{-3}$	$W_e - \langle D_v \rangle$ $\times 10^{-3}$	$\frac{(W_e - \langle D_v \rangle - \Delta K_m)}{\Delta K_m} \times 100\%$
$T = 460K$	$v_p = 0.05c$	2.4295	2.4281	-0.056%
	$v_p = 0.11c$	4.6999	4.6893	-0.011%
$T = 260K$	$v_p = 0.05c$	2.4281	2.4291	-0.041%
	$v_p = 0.11c$	4.6881	4.6892	-0.023%

In practice, we equilibrate the chain with the heat bath and mechanically stretch the chain at a constant rate. Then we compute the total external work and viscous work and compare them with the change of internal energy. The calculation is conducted at two different temperatures $T = 460K$ and $T = 260K$($T^* = 0.032$ and $T^* = 0.018$, correspondingly), and two different pulling velocities $v_p = 0.05c$ and $v_p = 0.11c$ ($v_p^* = 0.05$ and $v_p^* = 0.11$, correspondingly). Each case is repeated 300 times to make an ensemble average. We observe in our simulations that the change in kinetic energy of the chain is much smaller than the change in potential energy. Therefore, for simplicity, we ignore the kinetic energy in the mechanical energy change. Table 2.1 shows that the energy balance works well for a chain of linear springs.

Next, we come back to a chain with double-well springs and compare the driving force that we find from energy balance with that known analytically. As we have illustrated above, it is difficult to find the strains right behind and right in front of the phase boundary when the thermal fluctuation is large. Therefore, we set the temperature low enough such that the energy balance can be done with small non-zero thermal fluctuations.

We set $v_p^* = 0.08$ and $T^* = 0.001$. In this case there is only one phase boundary propagating (see Fig. 2.3(a)). The thermal fluctuation is small enough for us to find the strains right in front of and right behind the phase boundary, γ^- and γ^+, respectively. We obtain the strains for each time step and average over all time steps and over all replicas of the system. The result shows $\gamma^+ = 3.504$ and $\gamma^- = 0.949$. By eqn.(2.11) the corresponding driving force is $f_c = 2.179$. The driving force from the energy balance method eqn.(2.25) gives $f_e = 2.153$. The error is within 1%, which shows that the energy balance method agrees with analytical

expressions, at least for small thermal fluctuations.

2.2.6. Kinetic relation

Having verified that our energy balance method works we now want to use it to get the kinetic relation for a bi-stable chain at various bath temperatures. We carry out a series of computations for the impact problem under different pulling velocities and different temperatures. The temperature of the heat bath varies from $260K$ to $460K$ ($T^* = 0.018$ to $T^* = 0.032$), and the pulling velocity varies from 90m/s to 200m/s ($v_p^* = 0.05$ to $v_p^* = 0.11$). We showed above that the energy balance method is valid in this range.

Under these conditions there is only one phase boundary propagating through the bar. The phase boundary (see Fig. 2.3 (b),(c),(d)) moves in such a way that the spring right in front of the phase boundary jumps into the high strain state first and then the phase boundary "follows up" to the next mass. We had explained the reasons behind the jerky motion of the phase boundary which resulted in the plots of Fig. 2.2 earlier. The plots for the corresponding driving forces computed using eqn.(2.11) also fluctuated so much as to make it impossible to find the microscale kinetic law relating the driving force to the phase boundary velocity. However, we can still find the average driving force from eqn.(2.25) and homogenized phase boundary velocity from eqn.(2.18). These will enter a macroscopic kinetic relation just as emerges from spatial homogenization or time averaging in earlier works [14, 82, 83].

Fig. 2.4(a) and 2.4(b) show driving force and phase boundary velocities for two different temperatures T^* as blue dots. We generate such data for a large number of T^* values. We notice the following four facts: (1) at fixed pulling velocity, the phase boundary velocity suffers a tiny increase due to increasing temperature; (2) under same heat bath temperature, the phase boundary velocity increases with increasing driving force; (3) at the same phase boundary velocity, the driving force increases with increasing temperature, indicating a larger dissipation rate due to the phase transition; (4) at the same driving force, the phase boundary velocity decreases with increasing temperature, indicating a smaller dissipation rate due to the propagation of phase boundary. We postulate a kinetic relation in the

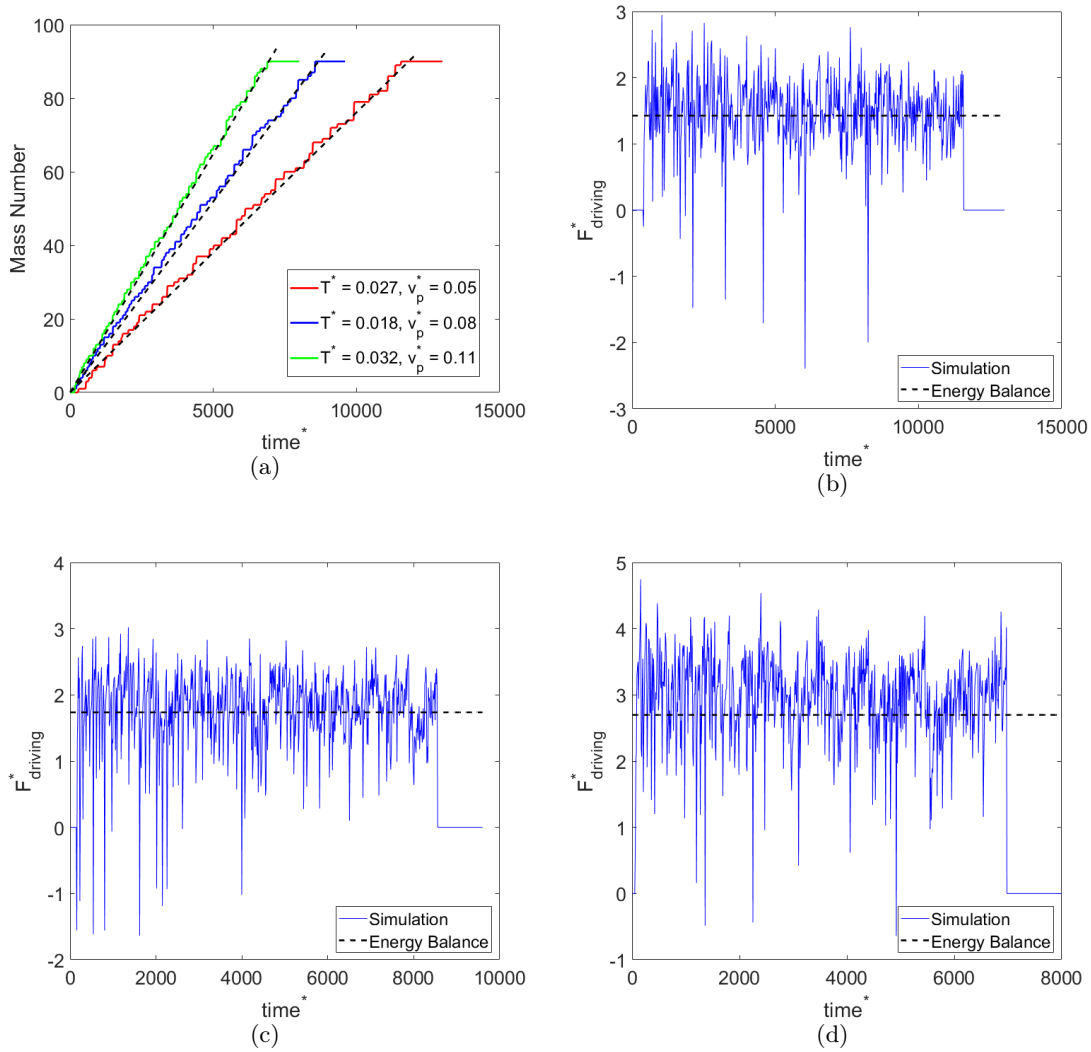

Figure 2.2: Homogenized phase boundary velocity and driving force. (a) Phase boundary position plotted as a function of time for three cases (1) $T^* = 0.027$, $v_p^* = 0.05$ (red curve), (2) $T^* = 0.018$, $v_p^* = 0.08$ (blue curve), and (3) $T^* = 0.032$, $v_p^* = 0.11$ (green curve). In each case we see a stair-case pattern characteristic of a discrete system. The dashed line through each stair-case has a constant slope which shows that there is a homegenized phase boundary velocity that is constant for constant v_p^*. (b,c,d) Plots of the driving force computed using eqn.(2.11) versus time for each of the three cases in (a). This figure shows that a meaningful relation between driving force and microscopic phase boundary velocity cannot be extracted.

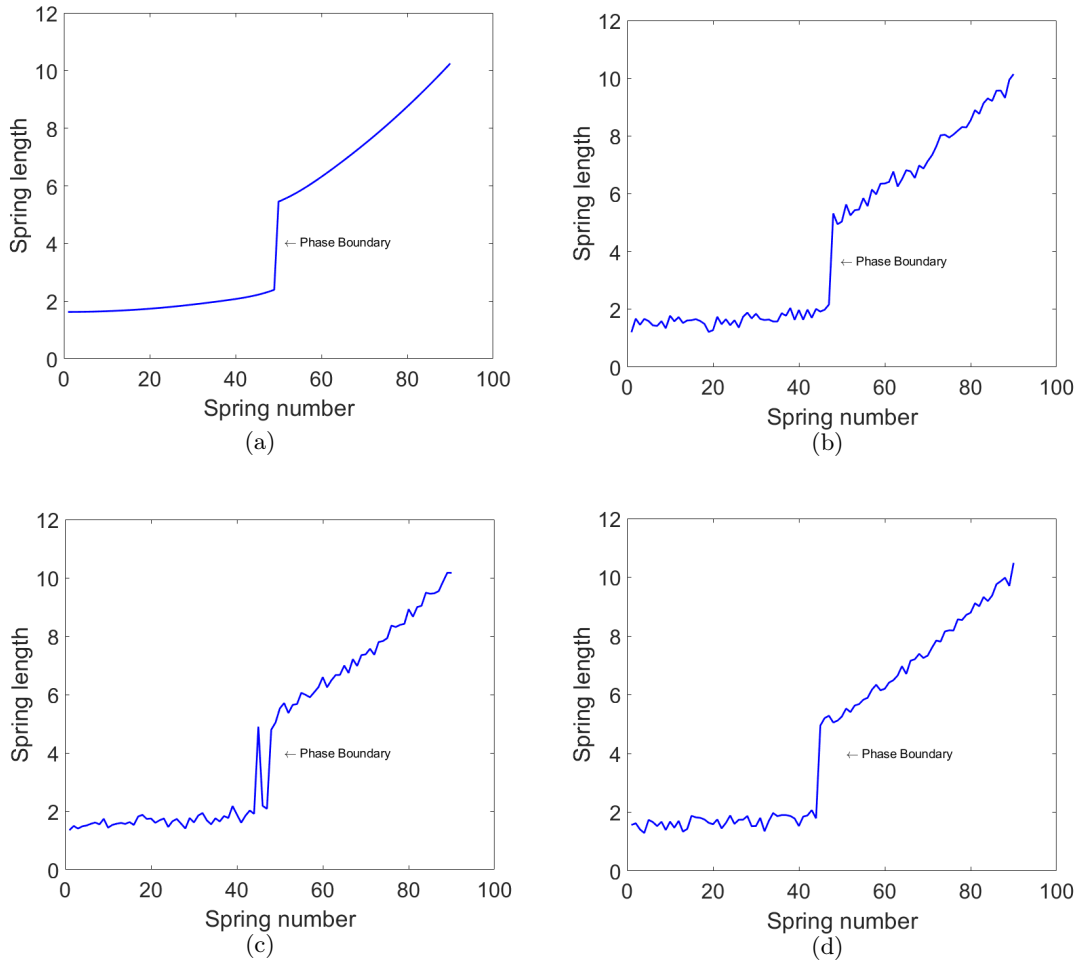

Figure 2.3: Snapshots of a chain with a phase boundary moving from right to left. (a) Snapshot for $T^* = 0.001$, $v_p^* = 0.08$. (b,c,d) Snapshots at three times showing the propagation of phase boundary for $T^* = 0.024$ and $v_p^* = 0.08$. In (b) the phase boundary is at mass number 48, in (d) it is at mass number 45. The instantaneous phase boundary velocity cannot be determined in a straight forward manner from snapshots b,c,d.

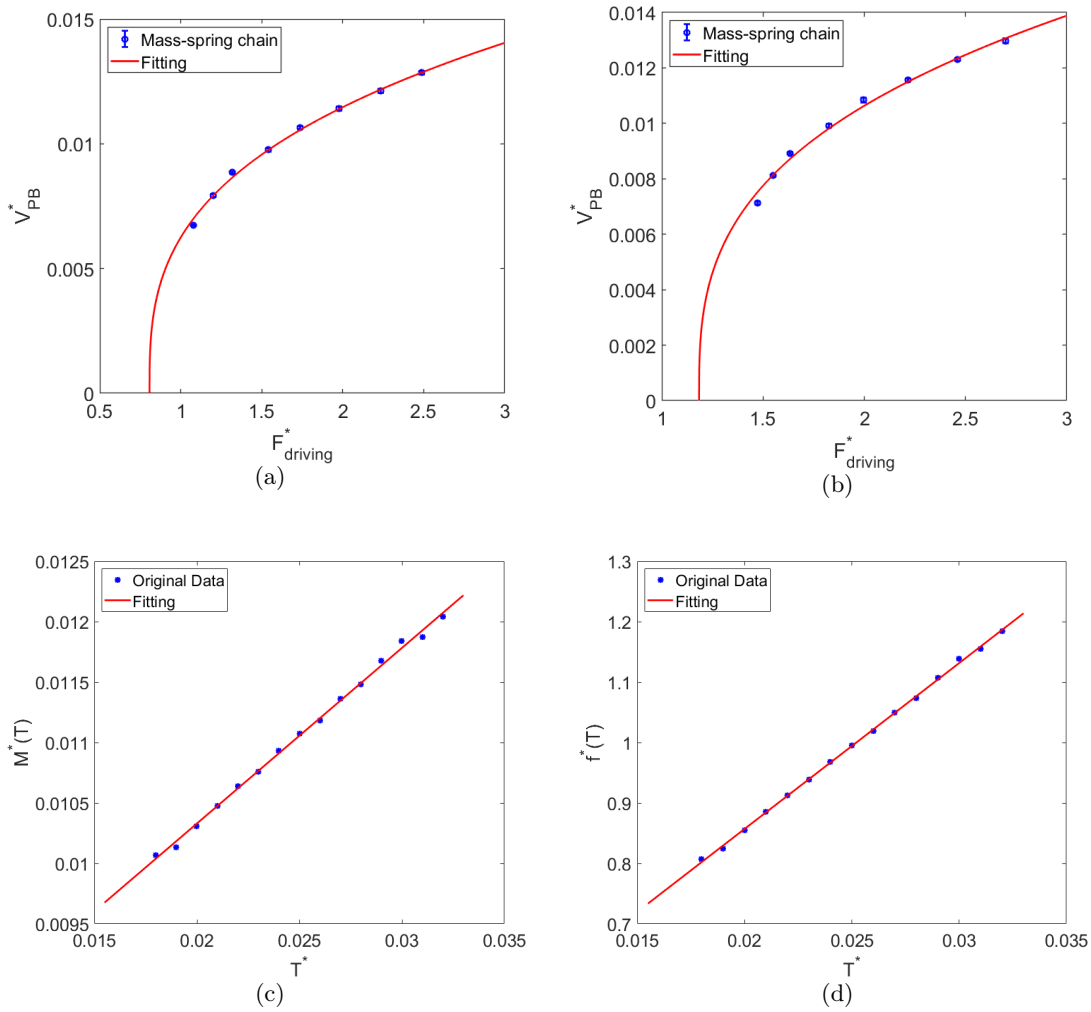

Figure 2.4: The kinetic relation at various temperatures. (a) $T^* = 0.018$ and (b) $T^* = 0.032$. The red lines are fitting based on eqn.(2.26). (c) M^* is a linear function of temperature. The correlation coefficient is $r^2 = 0.9974$. (d) $\hat{f}^*$ is also a linear function of temperature with correlation coefficient $r^2 = 0.9993$.

following form:

$$\dot{s}^* = M^*(T)(\frac{f^*}{\hat{f}^*(T)} - 1)^{\alpha}. \tag{2.26}$$

Here $\dot{s}^*$ denotes the non-dimensional phase boundary velocity, f^* is the non-dimensional driving force. $M^*(T)$ and $\hat{f}^*(T)$ both depend on temperature T. Fits of this equation to the data from our simulations is shown in Fig. 2.4(a) and 2.4(b) as red lines. A similar fitting exercise was carried out for all bath temperatures tested. We find $\alpha \approx \frac{1}{3}$, which is independent of temperature. Here M^* is a constant (it is like a mobility), and $\hat{f}^*$ is the minimum driving force to activate the propagation, or the minimum driving force to maintain the phase boundary. We find that both M^* and $\hat{f}^*$ are linear functions of non-dimensional temperature T^* as shown in Fig. 2.4(c) and Fig. 2.4(d), respectively:

$$M^* = 0.1453T^* + 0.007424, \tag{2.27}$$

$$\hat{f}^* = 27.44T^* + 0.3083. \tag{2.28}$$

The dimensional kinetic relation can be easily obtained from the above:

$$\dot{s} = M(T)(\frac{f}{\hat{f}(T)} - 1)^{1/3},\ M = 0.006838T + 5.063,\ \hat{f} = 1.894T + 308.3, \tag{2.29}$$

where f is units of picoNewton, M is in units of m/s, and T is in units of Kelvin.

A power law kinetic relation whose plots look similar to those in Fig. 2.4(b) has been studied by Abeyaratne, Chu and James [15]. They analyze the propagation of the phase boundary through a row of imperfections and find that in the limit of a large number of small imperfections the effective kinetic relation has a stick-slip type form. Thus, there is a critical value of driving force, a, such that the phase boundary moves only when $f > a$. a is a measure of energy associated with the imperfections. The slope of the graph of $\dot{s}$ versus f is infinite at $f = a$ in the kinetic relation of Abeyaratne, Chu and James [15], just as it is at $f^* = \hat{f}^*$ in our analytical form in eqn.(2.26). Temperature does not enter the analysis of Abeyaratne, Chu and James [15], rather they assume that at the microscopic

level the kinetic law governing the increase in a phase fraction is linear in the driving force. In a subsequent paper Abeyaratne and Vedantam [29] obtained a stick-slip kinetic law by analyzing a Frenkel-Kontorova type discrete model for kink motion in a crystalline solid and considering its implications at the continuum scale. They followed the methods of Atkinson and Cabrera [31] in which the dispersion relation of a defect moving at constant velocity through a lattice is analytically computed in the Fourier domain assuming that the lattice is subject to a constant externally imposed stress. Abeyaratne and Vedantam computed their own dispersion relation and specialized it to long wave-length waves (long in comparison to the lattice spacing) and showed how a stick-slip type kinetic law for phase boundary motion emerges. Inertia forces were important in their analysis, but the effects of temperature were not considered. A stick-slip type kinetic relation has also been obtained by Bhattacharya for phase boundary propagation in heterogeneous bodies [95]. He shows that irrespective of the microscopic kinetic law one ends up with a jerky motion of the phase boundary at macroscopic length scales if the material properties are heterogeneous. Temperature does not enter Bhattacharya's analysis either. Finally, De Tommasi *et al.* [33] inferred a stick-slip type kinetic law for the folding/unfolding transitions in macromolecules, but even they did not consider the effects of temperature and viscous drag. However, bath temperature effects both M and $\hat{f}$ in our simulations and our chain is homogeneous.

An example of a problem in which a phase fraction evolves in a jerky manner in a thermal environment has to do with plectoneme formation in DNA under high ionic concentrations [81]. This paper puts forth an explanation based on nanoscale friction for the experimentally observed jerky growth of the plectoneme phase when a long DNA molecule is twisted while subject to tension. The torque in the DNA increases as it is twisted while the plectoneme does not grow; the system is stuck at the bottom of an energy well. As the torque increases the energy barrier preventing exit from the well due to a random thermal kick becomes smaller. Min and Purohit [81] find a critical torque for causing plectoneme growth by equating the energy barrier to the thermal energy scale $k_B T$ and show that all experimental observations can be captured. Another example concerns jerky motion of a grain boundary

subject to shear loads in a thermal environment as has been observed in molecular dynamic simulations [84] . This paper also gives an explanantion for the jerky motion of the grain boundary by considering how energy barriers change in response to shear stresses and how a critical shear stress is required for the barrier to be surmounted at both zero or non-zero temperature. Motivated by these analyses we followed the methods of Puglisi and Truskinovsky [22] to obtain the free energy landascape from which we can obtain a critical force to move the phase boundary. However, this estimate of the critical force ignores the effects of fluid drag and thermal fluctuations on the chain and does not agree with the results from our simulations. We anticipate that an analysis based on the Fokker-Planck equation [96] will be necessary to explain the mechanisms behind our kinetic relation and it is beyond the scope of the present work.

2.3. Simulations with initial phase boundary

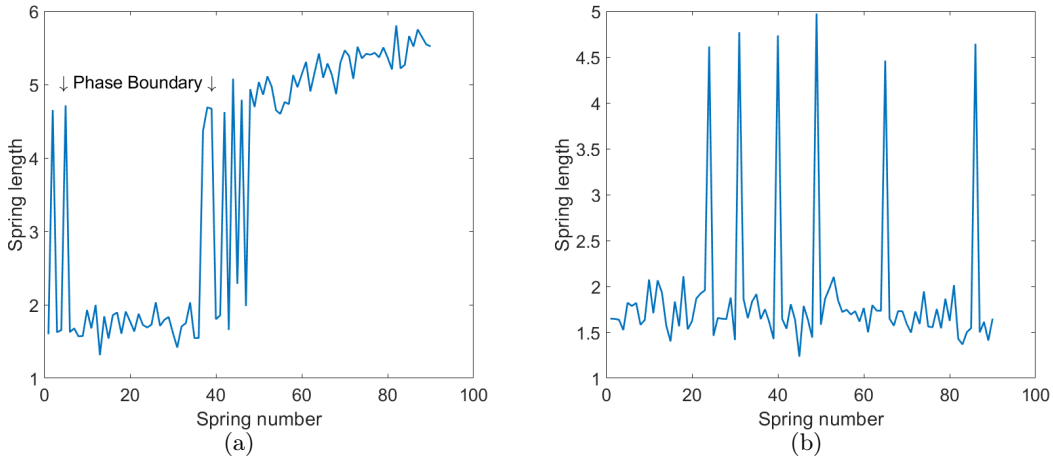

Figure 2.5: Failure of the energy balance method at low pulling velocities. (a) At $v_p^* = 0.01$, a second phase boundary appears at the left end and propagates rightward. It is cumbersome to apply the energy balance method with two propagating phase boundaries. (b) At $v_p^* = 0.002$, the phase transition proceeds through nucleation at random positions. The kinetic relation is irrelevant in this case.

In the previous section we found a kinetic relation which seems to be a power law after a threshold driving force to initiate motion is crossed; the coefficients $M(T)$ and $\hat{f}(T)$ are both increasing functions of temperature. The main goal of this section is to verify that this

kinetic relation is meaningful even if the boundary and initial conditions are different from the pulling (or impact) experiments considered before. Recall that $\hat{f}$ is the minimum driving force that maintains a phase boundary. However, in our simulations it is almost impossible to observe such a low driving force. To reach low driving forces we need to decrease the pulling velocity, but when the pulling velocity is smaller than $v_p^* = 0.02$, a second phase boundary appears (see Fig. 2.5(a)), and thus the assumption of one phase boundary fails. This is somewhat similar to the results of Atkinson and Cabrera [31] who show that multiple modes get excited at low defect velocities in their 1D chain, so that the relation between driving force and defect velocity is jagged for low velocities. However, our chain is different from that of Atkinson and Cabrera because it is immersed in a constant temperature bath (which imposes thermal kicks) and viscous drag (rather than inertia forces) dominates its mechanics. If we further decrease the pulling velocity then the phase transition is dominated by nucleation events (see Fig. 2.5(b)) in which random portions of the bar change to the high strain phase. The same phenomenon can be observed when we fix the pulling velocity and increase the temperature. For high temperatures and low pulling velocities the elongation is closer to a quasi-static process, resulting in a smaller dissipation rate.

In order to verify that the previous kinetic relation is valid for driving force smaller than $\hat{f}^*$, we study the motion of a phase boundary that is inserted into the bar as part of the initial conditions. Consider a bar occupying an interval of $[-L, L]$ in the reference configuration. The motion of the bar is governed by eqns.(2.2),(2.3),(2.4). Initially, the left half of the bar is in the low strain phase and the right half is in the high strain phase:

$$\gamma(x,0) = \begin{cases} \gamma_0^-, & -L \le x < 0, \\ \gamma_0^+, & 0 < x \le L. \end{cases} \tag{2.30}$$

The motion of the bar satisfies the following boundary conditions:

$$\gamma(-L,t) = \gamma_0^-, \qquad \gamma(L,t) = \gamma_0^+. \tag{2.31}$$

There is a phase boundary at $x = 0$ at $t = 0$. We would like to observe the evolution of this phase boundary and compare it with the prediction from the kinetic relation eqn.(2.26). To do this, we use the model of a mass-spring chain to simulate the motion of the bar. Suppose we have $2N+1$ masses and $2N$ springs with an energy landscape as described by eqn.(2.12). The motion of the masses is governed by the Langevin equation (eqn.(2.13)). Initially, the left N springs are in low strain phase, and the right N springs are in high strain phase:

$$\begin{aligned} x_i &= a_0(1+\gamma_0^-), \qquad i = 1, 2, ..., N, \\ x_i &= a_0(1+\gamma_0^+), \qquad i = N+1, N+2, ..., 2N, \end{aligned} \tag{2.32}$$

with the lengths at the two ends fixed throughout the simulation.

In our simulation we first fix the 2nd, the $N+1$th, and the $2N$th masses and equilibrate the chain with the heat bath. Then, we set free the whole chain and observe the evolution of the phase boundary. We first notice that there exist steady-state solutions under the above boundary conditions by solving the averaged Langevin equations. The whole chain moves at a constant velocity in steady state:

$$\dot{u_i} = \dot{u} = \frac{a_0(\gamma^+ - \gamma^-) + a_0 - a_t}{(2N-1)\nu} k, \quad i = 1, 2, ..., 2N+1. \tag{2.33}$$

However, without the kinetic relation, we cannot determine the position of the phase boundary, and thus the length of each spring in steady state is unknown. Let the $(q+1)$th mass be the location of the phase boundary, then lengths of the springs are:

$$\begin{aligned} x_i &= a_0(1+\gamma^-) + \frac{\nu\dot{u}}{k}(i-1), && i = 1, 2, ..., q, \\ x_i &= a_0(1+\gamma^+) - \frac{\nu\dot{u}}{k}(2N-i), && i = q+1, q+2, ..., 2N. \end{aligned} \tag{2.34}$$

In steady state, the phase boundary velocity must go to zero. Thus, from the kinetic relation eqn.(2.26), the driving force at the phase boundary must be f^* at steady state. Combining

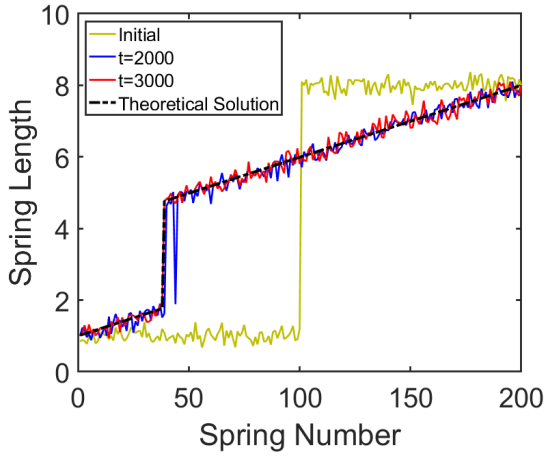

Figure 2.6: An example of the verification of eqn.(2.35) at $T^* = 0.028$. The black line shows the theoretical steady state solution given by eqn.(2.35). The yellow line represents the spring length initially. There is very little difference between $t = 2000$ (blue line) and $t = 3000$ (red line), which implies that the chain reaches steady state (black dashed line) at $t = 3000$.

eqn.(2.26) with eqn.(2.34) and eqn.(2.11), we find an analytical form for q:

$$q = N + \frac{f^*}{\mu\dot{u}}\frac{a_0}{a_t} - \frac{1}{2\mu\dot{u}}ka_0(\gamma^+ + \gamma^- - \gamma_t) = N - \frac{f_i - f^*}{\mu\dot{u}}\frac{a_0}{a_t}, \tag{2.35}$$

where $f_i = \frac{1}{2}ka_t(\gamma^+ + \gamma^- - \gamma_t)$ denotes the initial driving force. Notice that if the initial driving force is too large, then the phase boundary will keep moving leftwards and finally disappear at the left end if N is not large enough.

Hoping to verify the above analysis we carried out the simulations with $N = 100$ for different choices of γ^+ and γ^-. Generally, we find three possibilities – (1) a moving phase boundary under large driving force, (2) a stationary phase boundary when driving force is smaller than the critical, and (3) nucleation dominated phase transition when the chain is close to mechanical equilibrium. Fig. 2.6 shows an example in which two of these possibilities are seen. The calculation is carried out at $T^* = 0.028$, with initial strains $\gamma^- = 0.0$ and $\gamma^+ = 7.0$. In this case, the steady state phase boundary position is $q = 38$ by eqn.(2.35). In the beginning, the phase boundary stands in the middle at $q = 100$ (the yellow line) and moves leftwards at a relatively large velocity. After $t = 2000$, the phase boundary slows

down and nucleation events occur (see the blue line). The numerical results at $t = 2000$ and $t = 3000$ are both close to the theoretical solution eqn.(2.35), which implies that the kinetic relation eqn.(2.26) gives a good prediction.

2.4. Continuum and statistical mechanical analysis

Having verfied our kinetic relation we now want to input it as constitutive information for a continuum 1-D bar capable of phase transitions in an isothermal bath. Note that there is no reference to thermal fluctuations in the continuum mechanical description of the 1-D bar, so we expect that with the help of this kinetic relation we should be able to quantify the average force-extension response of the bar. We will check if the average force-extension relation of the bar matches that of a mass-spring chain immersed in an isothermal bath (in which no kinetic relation is specified).

2.4.1. Using the kinetic relation in a finite difference scheme

In this section we use a finite difference method to simulate the stretching of a 1-D bar and compare the force-extension relation with the result from our mass-spring chain in a heat bath. The constitutive relation for the bar satisfies eqn.(2.9). The motion of the phase boundary is described by the kinetic relation that we found in the previous section (eqn.(2.26)). Here f is the driving force on the phase boundary, given by eqn.(2.11) for bi-linear materials and $s(t)$ is the position of the phase boundary in the reference configuration. The 1-D continuum is discretized into several elements as described in Zhao and Purohit [97].

For nodes away from the phase boundary, the motion is governed by:

$$\frac{\partial \sigma}{\partial x} = d_w \dot{u}, \tag{2.36}$$

where $u(x,t)$ is the position of the material point x at time t, $\sigma(x,t)$ is the force at that point and d_w is a drag coefficient. We neglect inertia effects and assume that the surrounding fluid is static. The drag coefficient is the same as the one we used in a previous section on Langevin dynamics, $d_w = \frac{2\pi\mu}{\log l/r - 0.8}$. We then discretize eqn.(2.36) for numerical calculation

as:

$$\frac{\sigma^i_{j+\frac{1}{2}} - \sigma^i_{j-\frac{1}{2}}}{\Delta x} = d_w \frac{u^{i+1}_j - u^i_j}{\Delta t}. \tag{2.37}$$

Here i denotes the i-th time step and j denotes the j-th node. Δx is the element length and Δt is the time step. For the stability of the numerical method, the two must satisfy $\Delta t < \frac{(\Delta x)^2}{2}\frac{d_w}{k}$.

To numerically integrate the continuum equations of the bar, we need to consider two situations: (1) nodes away from the phase boundary, and(2) nodes close to the phase boundary. We assume that the forces in each element $\sigma^i_{j-\frac{1}{2}}$ at time instant i are known for $j = 1, 2, 3, ..., N+1$, together with the postion of the nodes u^i_j. Hence, the position u^{i+1}_j can be computed using eqn.(2.37). For nodes away from the phase boundary, the forces in each element can be updated by eqn.(2.9). For nodes close to a phase boundary the above scheme does not work. Let s denote the position of the phase boundary in the reference configuration and assume that it is between node l and node $l+1$. To describe the propagation of the phase boundary, we need equations to update the positions of nodes l, $l+1$ and s. These can be obtained from: (1) the balance of the linear momentum which requires $[|\sigma|] = 0$ across the phase boundary; (2) the total reference length between nodes l and $l+1$ is Δx; (3) the continuity of the displacement u; and (4) the kinetic relation that governs the evolution of the position $s(t)$ of the phase boundary. Using these the numerical scheme near the phase boundary is given by [97]:

$$\begin{aligned}
&\Delta x^i_- + \Delta x^i_+ = \Delta x, \\
&u^{i+1}_l = u^i_l + \frac{\Delta t}{d_w \Delta x}(\sigma^i_d - \sigma^i_{l-\frac{1}{2}}), \\
&u^{i+1}_{l+1} = u^i_{l+1} + \frac{\Delta t}{d_w \Delta x}(\sigma^i_{l+\frac{1}{2}} - \sigma^i_d), \\
&\Delta x^{i+1}_- = \Delta x^i_- - \dot{s}^i \Delta t, \\
&u^{i+1}_{l+1} - u^{i+1}_l = (\frac{\sigma^{i+1}_d}{k} + 1)\Delta x^{i+1}_- + (\frac{\sigma^{i+1}_d}{k} + 1 + \gamma_t)\Delta x^{i+1}_+,
\end{aligned} \tag{2.38}$$

where σ^i_d denotes the force at the phase boundary and Δx^i_- and Δx^i_+ denotes the length in

reference configuration of part of this element in the low strain phase and high strain phase, respectively. $\dot{s}$ is the phase boundary velocity obtained from eqn.(2.11) and eqn.(2.29). In Fig. 2.7 we show the results of integrating the continuum equations (black curves) together with those from the mass-spring calculations (blue lines) for various combinations of pulling velocity and bath temperature. The excellent agreement between the two curves indicates that the kinetic relation extracted using the energy balance method from the Langevin dynamics simulations is reliable.

2.4.2. Estimating the size of fluctuations

In this section we give a statistical mechanical method to estimate the magnitude of thermal fluctuation in the force-extension relation, given the ergodicity and local equilibrium assumption at the microscale. First, our mass-spring chain immersed in a bath is very similar to a Rouse chain model for polymers immersed in liquid[98]. We compare the time scale of pulling τ_p with the fastest mode of the Rouse model (i.e., the one with the shortest wavelength which will be the length of the springs a_0 in the unloaded configuration for our chain) τ_r:

$$\tau_p = \frac{a_0}{v_p} \approx 10,$$
$$\tau_r = \frac{a_0^2 \nu}{3\pi^2 k_B T} \approx 0.37.$$

Since $\tau_p \gg \tau_r$, our masses are in local equilibrium. Second, our computation of three time scales in section 2.2.4 showed that the time scale for in-well minimization is the shortest. Further, we notice that in our Langevin dynamics, the extensional force takes the form

$$\sigma_N = \begin{cases} k(x_N - a_0), & x_N < x_c, \\ k(x_N - a_t), & x_N \geq x_c, \end{cases}$$

where x_N is the extension of the N-th mass and σ_N is the force on the N-th mass. When there is no phase boundary, the force is a linear function of the extension x_N. The fluctuation

in the extensional force could then be written as:

$$\langle(\sigma_N - \bar{\sigma}_N)^2\rangle = k^2\langle(x_N - \bar{x}_N)^2\rangle.$$

Clearly, the fluctuation of the force σ_N depends only on the fluctuation in the length of the n-th spring.

Now, the evolution of the chain is governed by the Langevin equation eqn.(2.13). If we decompose the motion as the average part plus the fluctuating part, $u_i = \langle u_i\rangle + \hat{u}_i$ and make an ensemble average, we find the equation for the fluctuating part:

$$m\ddot{\hat{u}}_i = -\nu\dot{\hat{u}}_i - \left(\frac{\partial\phi}{\partial u_i} - \left\langle\frac{\partial\phi}{\partial u_i}\right\rangle\right) + F_i(t).$$

If we temporarily ignore the propagation of the phase boundary, since the potential is bi-quadratic and the stiffness of the springs in both high strain phase and low strain phase is identical, we can find:

$$m\ddot{\hat{u}}_i = -\nu\dot{\hat{u}}_i - \frac{\partial^2\phi}{\partial u_i^2}\hat{u}_i + F_i(t), \tag{2.39}$$

with boundary conditions $\hat{u}_0 = \hat{u}_N = 0$. Next, we note that the fluctuation of the motion of each mass i of a length-fixed chain with the phase boundary fixed at a specific spring satisfies the same governing equation and boundary condition. For this reason we use the equilibrium fluctuation to approximate the fluctuation of the extensional force during the stretching.

We define a canonical ensemble $Z(N, L, T)$ of the mass-spring chain. Here N is the number of degrees of freedom, which is the number of masses not located at the boundary. L is the total length of the chain. T is the temperature of the system. The microstate of the system is given by $(p_1, u_1, p_2, u_2, ..., p_N, u_N; L, T)$, with the energy:

$$H = \sum_{i=1}^{n}\frac{1}{2m}p_i^2 + \phi(u_1, u_2, ..., u_N; L).$$

Here ϕ is the potential energy stored in the springs. For our bi-linear mass spring chain satisfying eqn.(2.12), the potential energy is given by:

$$\phi = \sum_{i=1}^{N+1} \frac{k}{2}(u_i - u_{i-1} - a_i)^2, u_0 = 0, u_{N+1} = L.$$

The probability for the system to occupy such a microstate in the phase space satisfies the canonical distribution:

$$f(p_i, u_i : i = 1, 2, ..., N; L, T) = \frac{1}{Z} \exp(-\frac{H}{k_B T}),$$

where k_B is the Boltzmann constant. Z, the partition function, is defined as the normalization factor of the probability distribution:

$$Z(L, T) = \int \exp(-\frac{H}{k_B T}) \mathrm{d}p_1 ... \mathrm{d}p_N \mathrm{d}u_1 ... \mathrm{d}u_N, \tag{2.40}$$

with the integration carried out over all degrees of freedom. The free energy of the system is given by:

$$\mathcal{F} = -k_B T \log(Z). \tag{2.41}$$

The average force exerted at the boundary and the variance of the force are given, respectively, by [99]:

$$\langle \sigma \rangle = \frac{\partial \mathcal{F}}{\partial L} = -k_B T \frac{\partial}{\partial L} \log Z, \tag{2.42}$$

$$\langle (\sigma - \langle \sigma \rangle)^2 \rangle = k_B T \left(\langle \frac{\partial^2 H}{\partial L^2} \rangle - \frac{\partial^2 \mathcal{F}}{\partial L^2} \right). \tag{2.43}$$

For bi-linear materials satisfying constitutive relation eqn.(2.12) with the same stiffness for two phases, the partition function from eqn.(2.40) is given by the following [20]:

$$Z = N^{-\frac{1}{2}} (\frac{2\pi k_B T}{h})^N (\frac{m}{k})^{\frac{N}{2}} \sum_{q=0}^{N+1} \frac{(N+1)!}{q!(N+1-q)!} \exp\{-\frac{k}{2k_B T(N+1)}[L-(qa_0+(N+1-q)a_t]\}. \tag{2.44}$$

Further, if the phase boundary is at the q-th mass, with q springs in low strain phase and $N+1-q$ in high strain phase, the partition function is:

$$Z = N^{-\frac{1}{2}}(\frac{2\pi k_B T}{h})^N(\frac{m}{k})^{\frac{N}{2}} \exp\{-\frac{k}{2k_B T(N+1)}[L-(qa_0+(N+1-q)a_t]\}. \tag{2.45}$$

Combining eqns.(2.41),(2.43),(2.45), we find that the variance of the extensional force, given by:

$$\langle(\sigma - \langle\sigma\rangle)^2\rangle = V_\sigma^2 = \frac{Nk}{N+1}k_B T \approx k k_B T. \tag{2.46}$$

In Fig. 2.7 the red dashed lines above and below the black lines show $\sigma_N \pm V_\sigma$. The dashed lines provide a good estimate of the force fluctuations seen in the Langevin dynamics simulations except when the phase boundary first appears when there is a large jump in the extensional force.

2.5. Cyclic loading and hysteresis

In most experiments on phase transforming materials both loading and unloading are performed in a cyclic manner to estimate the hysteresis [17]. Now we will explore the consequences of our stick-slip kinetic relation on loading rate and temperature dependence of hysteresis. Cyclic loading and unloading of an overdamped chain was recently studied by Benichou and Givli [77, 78] and a relationship between hysteresis, loading rate and energy barriers was explained. In our simulations the energy dissipation at the phase boundary depends strongly on the loading rate as well, but to unravel the hysteresis in cyclic loading we must study the kinetic relation in the third quadrant of the $f - \dot{s}$ plane. In our simulations, we use the end state in the extension process for the mass-spring chain as the initial condition for the unloading. We first equilibriate the system at maximum extension, then we unload the chain at the same rate as loading. However, in our simulation if we use the constitutive relation given by eqn.(2.12), we unrealistically get a strain less than -1 in the low strain phase in many springs. To address this we modify our potential in the discrete

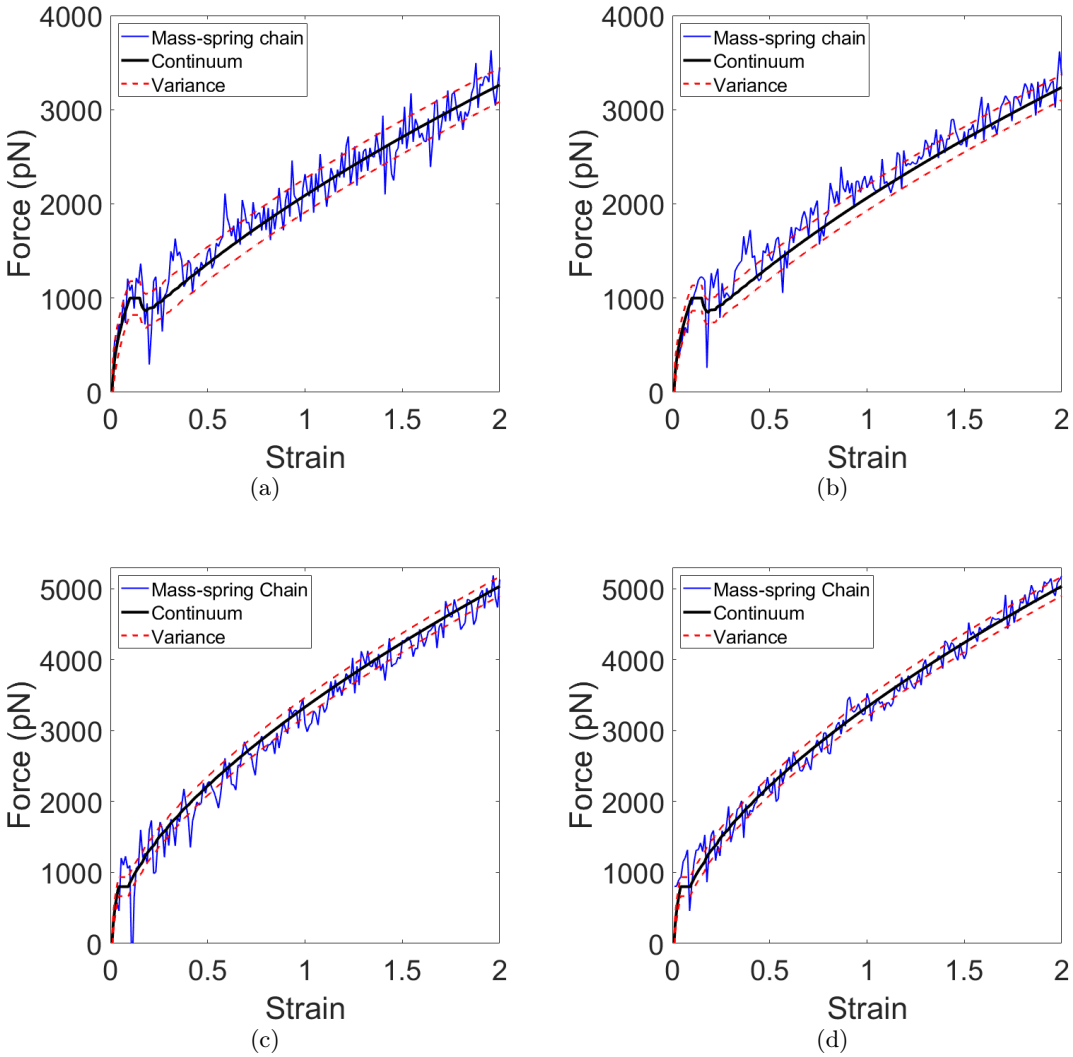

Figure 2.7: The continuum simulation matches the results from Langevin dynamics on a mass-spring chain in a heat bath. The equilibrium approximation for the fluctuation of the extensional force agrees with the the numerical calculation for different temperatures and velocities. (a) $T^* = 0.032$, $v^* = 0.05$; (b) $T^* = 0.018$, $v^* = 0.05$; (c) $T^* = 0.032$, $v^* = 0.10$; (d) $T^* = 0.018$, $v^* = 0.10$;

mass-spring chain to the following:

$$W = \begin{cases} \frac{10^{-3}}{2} k a_0^2 \left((\frac{a_0}{x_i})^2 - 2\frac{a_0}{x_i} + 730 \right), & x < 0.1a_0 \\ \frac{1}{2}k(x_i - a_0)^2, & 0.1a_0 \le x < x_c, \\ \frac{1}{2}k(x_i - a_t)^2, & x \ge x_c. \end{cases} \tag{2.47}$$

Thus, the force in the springs is

$$F = \begin{cases} 10^{-3} k a_0 \left((\frac{a_0}{x_i})^3 - (\frac{a_0}{x_i})^2 \right), & x < 0.1a_0 \\ -k(x_i - a_0), & 0.1a_0 \le x < x_c, \\ -k(x_i - a_t), & x \ge x_c. \end{cases} \tag{2.48}$$

The coefficients are chosen such that the potential energy and the force are continuous at $x = 0.1a_0$. The potential consists of a bi-linear part when $x > 0.1a_0$, and a non-linear part that goes to infinity when $x \to 0$. This ensures that spring length will not be negative in our simulations.

We study the cyclic force-strain relation for the cases $T^* = 0.018$, $v^* = 0.08$ (blue curve) and $v^* = 0.05$ (red curve) in Fig. 2.8(a). We notice that the force-strain curves for loading and unloading are different. The force in the plateau region is smaller in the unloading process than in the loading process at the same strain. Also, during unloading the phase boundary appears later on the right end than when it disappeared at the left end during loading. When the extension reaches 0, the phase boundary has not yet reached the left end. The above phenomenon leads to hysteresis in the loading-unloading cycle (see Fig. 2.8(a)(b)). The hysteresis has two parts, (a) the dissipation due to viscous drag of the fluid, and (b) dissipation due the propagation of the phase boundary. It is rate-dependent as can be seen from the red and blue loops in Fig. 2.8(a) with more hysteresis at higher pulling velocity. In Fig. 2.8(b) we plot the force-strain curves at two different temperatures but the same pulling speed and find that the hysteresis hardly changes. The finding that the magnitude

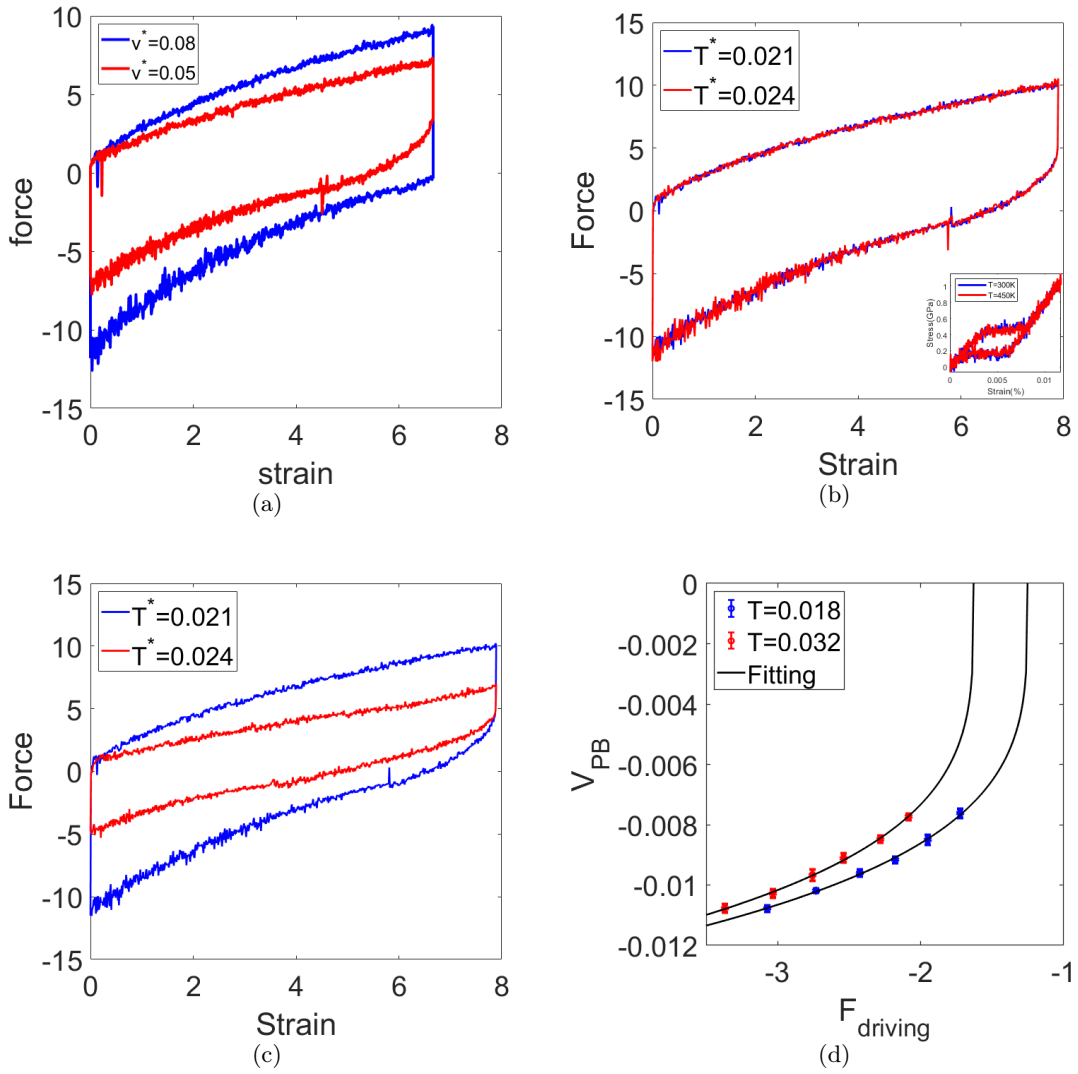

Figure 2.8: Dependence of hysteresis on loading rate and temperature. (a) The force-strain relation for $v_p^* = 0.08$, $T^* = 0.018$ (blue curve) and $v_p^* = 0.05$, $T^* = 0.018$ (red curve). There is lower hysteresis at lower strain rate. (b) The force-strain relation at $v_p^* = 0.08$ and $T^* = 0.024$ (red curve) and $T^* = 0.021$ (blue curve). The hysteresis is hardly affected by the change in bath temperature. The inset shows force-strain curves at two different temperatures with parameters same as in Fig. 2.1(c) in which we used a lower drag coefficient and low pulling velocity. (c) The force-strain relation for $v_p^* = 0.08$, $T^* = 0.021$ (blue curve) and $T^* = 0.024$ (red curve) with the decrease in viscosity of water with increasing temperature accounted for. (d) Kinetic relation inferred from the Langevin dynamics calculations in the third quadrant of the $f - \dot{s}$ plane for the unloading process.

of hysteresis is almost independent of temperature is consistent with experimental results on several shape memory alloys [100]; however, we must not ignore the fact that the hysteresis in our simulations is dominated by fluid drag (whose coefficient was not changed when we changed the bath temperature), not the dissipation due to phase boundary propagation. Therefore, in the inset of Fig. 2.8(b) we perform a simulation with low drag coefficient and low pulling speed and parameters for vanadium oxide used in Fig. 2.1. The inset confirms that hysteresis hardly changes with temperature for this case too in which viscous dissipation is very small and all the dissipation is due to phase boundary propagation. This inset also shows that our mass-spring model can capture rate-independent hysteresis (which implies a stick-slip form of the kinetic law). Finally, in Fig. 2.8(c) we account for the reduction in drag coefficient with temperature (due to decreasing viscosity of water at higher temperatures) and show that hysteresis can decrease with increasing temperature. A decrease in hysteresis with increasing temperature has been observed in experiments on whelk egg capsules by Miserez *et al.* [101]. They performed stress-strain experiments (at constant strain rate) while their specimen was immersed in water held at a fixed temperature. They showed, using wide angle X-ray scattering, that a reversible α-helix to β-sheet transition is the reason for the typical stress-strain curves (with plateaus) seen in their experiments. Although their observation of a decrease in moduli with increasing temperature may be the reason for the decrease in hysteresis with increasing tempeature, we speculate on the basis of Fig. 2.8(c) that the decreasing viscosity of water with increasing temperature should not be ignored.

During unloading the strains lie in the non-linear region in the low strain phase behind the phase boundary. Therefore, the kinetic relation in this case must be different from the extension. Also, eqn.(2.11) is no longer applicable for this non-linear potential. However, we can still use the energy balance method eqn.(2.25) to find the driving force. This allows us to plot the kinetic relation in the third quadrant of the $f - \dot{s}$ plane. The result is shown in Fig. 2.8(d). The form of the kinetic relation in this quadrant is similar to that in the first quadrant. For example, at the same driving force the phase boundary moves slower at higher temperature. The kinetic relation also follows the form of eqn.(2.26) with power

$\alpha = \frac{1}{4}$.

2.6. Concluding remarks

In this paper we have used energy balance to obtain the kinetic relation for a phase boundary in a bistable bar immersed in a heat bath. We performed Langevin dynamic simulations on a mass-spring chain with bistable springs at various pulling velocities and bath temperatures and revealed a jerky motion of the phase boundary due to the discreteness of the system and thermal fluctuations caused by the bath. Yet, we could find a relation between the homogenized phase boundary velocity and an average driving force on it even though the microscopic kinetic law was hard to discern. We found a stick-slip type kinetic relation for the homogenized phase boundary velocity which is characteristic of friction. Our kinetic law bears some similarity to those obtained for phase boundary propagation through a row of imperfections [15] and heterogeneous materials [95] , but we reveal a temperature dependence of the kinetics that had not been seen before. While inertia played an important role in early derivations of stick-slip kinetic laws [31], our chains are dominated by viscous drag and thermal fluctuations that are important for biological macromolecules. The form of the slip part of our kinetic relation is a power law which is different from the Arrhenius form which may be expected for thermally activated phase boundary motion [17]. A result of the stick-slip kinetics is that the force-extension relations are different for the loading and unloading paths which leads to hysteresis. We have also shed light on the role and magnitude of thermal fluctuations in the force-extension response of our bistable bar. The kinetic law derived here may be relevant to the mechanical response of macromolecules, such as, coiled-coil proteins that rely on force-induced structural transitions for their function.

CHAPTER 3

On fluctuation theorems applied to mass-spring chains

This chapter is partially based on work published in [102].

3.1. Introduction

Among all laws of physics, the second law of thermodynamics is most interesting and holds secrets that are yet being uncovered: it gives time an arrow and reveals the asymmetry between past and future. There have been different ways to express this law since 1824 which was first given by Sadi Carnot in his study of heat engines. One of them, given by Rudolf Clausius, separates reversible processes from irreversible processes, and is now known as the Clausius theorem which claims:

$$\langle W \rangle \geq \Delta F, \tag{3.1}$$

where W is the work done on a system and ΔF is its free energy change. Here $\langle \cdot \rangle$ denotes expected value, or equivalently, the ensemble average over multiple realizations. This implies that for a certain loading protocol, there exists small portion of trajectories where $W < \Delta F$, although eqn.(3.1) continues to hold true in the average sense. However, this picture is incomplete by the nature of eqn.(3.1) being an inequality; it is still puzzling to fully characterize non-equilibrium processes.

The past decades have witnessed great advances in a series of fluctuation theorems providing us with new tools to step further in understanding fluctuations, irreversibility, and non-equilibrium processes. The first fluctuation theorem was discovered by Bochkov and Kuzovlev [34] in 1977, which relates the characteristic functional of a stochastic process to the forward and time-reversed processes. Later, based on a numerical finding of the entropy production fluctuation for an isothermal shear-driven fluid[35], the steady-state fluctuation theorem was proved by Gallavotti and Cohen[103] in 1995, which describes the symmetry of

the probability distribution of entropy production. In 1997[36], a remarkable relation was discovered by Jarzynski to obtain equilibrium free energy difference by fluctuations. Speciafically, for systems that are initially sampled from the Boltzmann-Gibbs distribution at temperature T, and driven arbitrarily away from equilibrium, it was shown that the difference between the Helmholtz free energy of the final and initial state (ΔF) and the work W satisfy

$$\left\langle e^{-\frac{W}{k_B T}} \right\rangle = e^{-\frac{\Delta F}{k_B T}}, \tag{3.2}$$

where k_B denotes the Boltzmann constant. By applying Jensen's inequality[104], eqn.(3.1) can be easily obtained from eqn.(3.2). Meanwhile, the equilibrium free energy change between the initial and end states can be found from the non-equilibrium average of the exponential of the work done on the system by

$$\Delta F = -k_B T \ln \langle \mathrm{e}^{-\frac{W}{k_B T}} \rangle. \tag{3.3}$$

This shows that the dimensionless free energy change $\beta \Delta F$ as a function of $\beta = \frac{1}{k_B T}$ represents the cumulant generating function of the distribution of work W. By a cumulant expansion of eqn. 3.3, the free energy change can be calculated as[36],

$$\Delta F = \sum_{i=1}^{\infty} (-\beta)^{n-1} \frac{\omega_n}{n!}, \tag{3.4}$$

where ω_n is the n-th cumulant of the work distribution. Specifically, if the work distribution is Gaussian, all the higher order terms vanish except the first two terms,

$$\Delta F = \langle W \rangle - \frac{1}{2} \beta \sigma_W^2, \tag{3.5}$$

where σ_W^2 is the variance of the work distribution. A closely related relation is the Crooks fluctuation theorem found by Crooks[37] in 1998. It relates the free energy change and the work done for a single trajectory with the corresponding forward and time-reversed path

probabilities:

$$\frac{P_{A\to B}(W)}{P_{A\leftarrow B}(-W)} = \exp\left(\frac{W-\Delta F}{k_B T}\right), \tag{3.6}$$

where A and B denote the initial and end equilibrium canonical states, respectively. The Jarysnski equality eqn.(3.2) can be directly reproduced from Crooks fluctuation theorem by considering

$$\begin{aligned}\left\langle \exp\left(-\frac{W-\Delta F}{k_B T}\right)\right\rangle &= \int_{-\infty}^{+\infty} \exp\left(-\frac{W-\Delta F}{k_B T}\right) P_{A\to B}(W)\mathrm{d}W \\ &= \int_{-\infty}^{+\infty} P_{A\leftarrow B}(-W)\mathrm{d}W \\ &= 1.\end{aligned}$$

Fluctuation theorems were further developed by Hummer and Szabo[105], who extended Jarzynski equality and showed that the free energy can be extracted from repeated non-equilibrium force measurement. Hatano and Sasa[106] proposed a similar relation that can find the free energy difference of two non-equilibrium steady states. More details of fluctuation theorems can be found in following references [107–110].

Both the Jarzynski equality and Crooks fluctuation theorem were verified by single molecule force-extension experiments on bio-molecules[26, 38]. They have been then leveraged to extract free energy changes from work distributions. Here would like to determine if these relations can be used to characterize non-equilibrium material behaviors such as the kinetics of phase transitions. Our effort is analogous to applying fluctuation-dissipation relations, such as the Green-Kubo formulae, to characterize transport coefficients in the linear response regime. In that sense, these fluctuation theorems can be seen as a generalization of Green-Kubo formulae for processes that are driven arbitrarily far away from equilibrium. More details connecting the Jarzynski equality and Green-Kubo relation will be discussed in section 2.

The analysis here will be carried out using model of mass spring chain in a heat bath, which

may be described by over-damped Langevin dynamics with linear or nonlinear interactions (the same as is in the previous chapter). For the linear case, we compare the free energy changes computed from the Jarzynski equality and Crooks fluctuation theorem with theoretical formulae. For the double welled case, we point out the major issues that limit the application of fluctuation theorems.

This chapter is structured as follows. In sections 2 we derived a Green-Kubo relation for Gaussian processes of interest. In section 3 we present the numerical results for a mass-spring system with linear springs. In section 4 we discuss the cases with phase boundary propagation. In section 5 we give a outlook of future work.

3.2. Green-Kubo Relation

We here show that for a near-equilibrium Hamiltonian process, where the probability distribution for work is Gaussian at all times, the Jarzynski relation $\Delta F = \langle W \rangle - \frac{1}{2}\beta\sigma_W^2$ takes the form of a Green-Kubo formula, i.e.

$$\begin{aligned} &\Delta F = \langle W \rangle - \frac{\beta}{2}\int_0^\tau dt\dot{\lambda}^2(t)\int_{-\infty}^{\infty} C(s;\lambda(t))\,ds, \quad \text{where} \\ &C(s;\lambda(t)) = \left\langle \left(\frac{\partial H}{\partial \lambda}(z_0;\lambda) - \left\langle \frac{\partial H}{\partial \lambda}(z_0;\lambda) \right\rangle_\lambda^{eq} \right) \left(\frac{\partial H}{\partial \lambda}(z_s;\lambda) - \left\langle \frac{\partial H}{\partial \lambda}(z_s;\lambda) \right\rangle_\lambda^{eq} \right) \right\rangle_\lambda^{eq} \end{aligned} \tag{3.7}$$

is the equilibrium auto-correlation function at fixed λ, and H is the Hamiltonian of the system dependent on the microscopic variables z (position and momenta of each particle). The ensemble average in C is done according to the equilibrium probability distribution at fixed λ. The proof below follows the main ideas of Section 4 of [111].

For Hamiltonian dynamics, the work done by the protocol $\lambda(t)$ in the interval $[0,\tau]$ is given by

$$W(\tau) = \int_0^\tau \frac{\partial H}{\partial \lambda}\dot{\lambda}(t)\,dt. \tag{3.8}$$

Hence, the variance of the work may be expressed as

$$\begin{aligned}\sigma_W^2 &= \left\langle (W - \langle W \rangle)^2 \right\rangle \\ &= \int_0^\tau dt \dot{\lambda}(t) \int_0^\tau dt' \, \dot{\lambda}(t') C(t,t'), \quad \text{where} \\ C(t,t') &= \left\langle \left(\frac{\partial H}{\partial \lambda}(z_t;\lambda_t) - \left\langle \frac{\partial H}{\partial \lambda}(z_t;\lambda_t) \right\rangle \right) \left(\frac{\partial H}{\partial \lambda}(z_{t'};\lambda_{t'}) - \left\langle \frac{\partial H}{\partial \lambda}(z_{t'};\lambda_{t'}) \right\rangle \right) \right\rangle\end{aligned} \tag{3.9}$$

is the auto-correlation function. Since the process is near-equilibrium, we adopt the classical assumptions for the auto-correlation function from [87], namely

1. $C(t,t')$ depends only on the interval $|t-t'|$, i.e. $C(t,t+s) = C(s)$.
2. $C(0) > 0$.
3. $\forall\, s$, $|C(s)| \leq C(0)$.
4. $C(-s) = C(s) = C(|s|)$.
5. As s is large enough compared to a characteristic time τ_{ac}, $C(s)$ approaches 0. In other words, the magnitude of $C(s)$ is significant only when s is of the same order as τ_{ac}.

Next, we introduce a change of variable $(t,t') \to (t, s = t'-t)$. This results in a change in the integration domain, as shown in Fig. 3.1, from a square area to a parallelogram area. However, for slow processes as those discussed here, the time scale for the decay of the auto-correlation function τ_{ac} is much smaller than the time scale for the process $\tau_{ac} \ll \tau$. Therefore, only a narrow band around $s = 0$ (the area between the red dashed lines in Fig. 3.1(b)) contributes to the integral; larger values of $|s|$ have negligible contribution. Thus, the limit of integration for s can be replaced by $-\infty$ and $+\infty$, $\lambda(t')$ can be approximated by $\lambda(t)$, and the results follow.

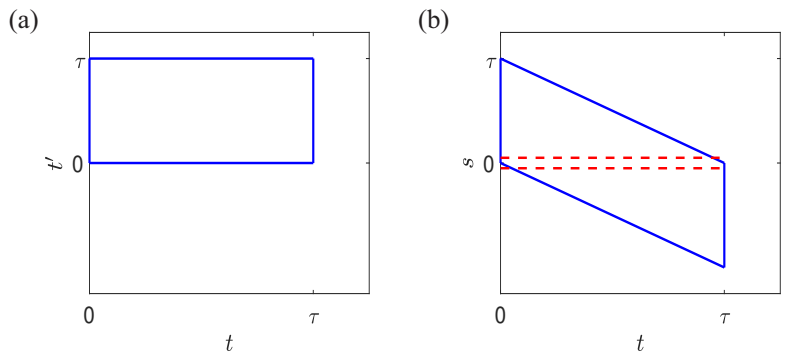

Figure 3.1: By introducing the change of variables $(t, t') \to (t, s = t' - t)$, the integration domain in eqn. (3.7) changes from the square area (a) to the parallelogram area (b).

.

3.3. Linear Spring Calculation

3.3.1. Modeling

We consider a one-dimensional mass-spring chain in contact with heat bath at temperature T. The system is composed of $N + 1$ particles, whose position as a function of time are denoted as $x_i(t)$ $(i = 0, 1, \cdots, N)$, and N identical springs. Each spring has a natural length $l_0 = 1$ and is characterized by a potential energy $V(u_i)$, where $u_i = x_i - x_{i-1} - l_0$ denotes the elongation of the spring. The mass-spring chain is fixed at one end $(x_0 = 0)$ and pulled on the other end under a work protocol, $x_N = \lambda(t)$. The governing Langevin equation for the unconstrained masses are given by

$$m\ddot{x}_i = -\nu\dot{x}_i + f_s(u_{i+1}) - f_s(u_i) + \sqrt{2\eta k_B T}\xi_i, \quad i = 1, \cdots, N-1, \tag{3.10}$$

where $f_s(u_i) = \frac{dV}{du_i}$ is the force in spring i, ν is a damping constant. We use ξ_i to denote independent Gaussian processes obeying $\langle \xi_i \rangle = 0$ and $\langle \xi_i(t)\xi_j(t') \rangle = \delta_{ij}\delta(t - t')$.

We confine our attention to the quadratic potential $V(u) = \frac{1}{2}ku^2$, with various temperatures and damping coefficients. For each of the cases, we start by stretching the mass-spring chain by a length L_{ini}. Then, we fix both ends of the chain to equilibrate it with the heat bath identified by the convergence of the total potential energy. Subsequently, a work protocol

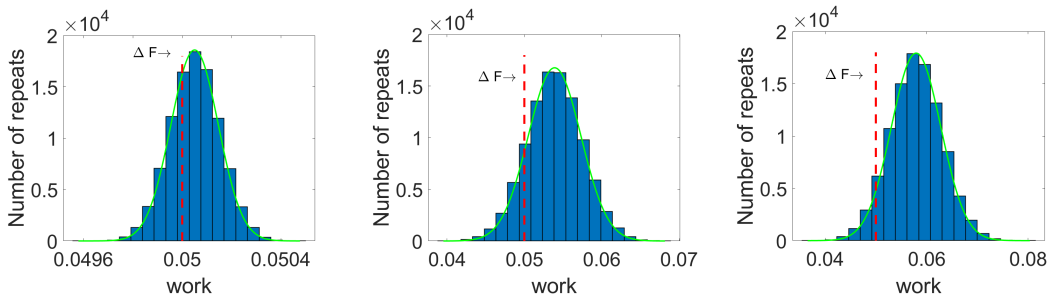

(a) (b) (c)

Figure 3.2: Work distributions at different pulling rates and drag coefficient. (a) $v_p = 0.005$, $\mu = 0.01$; (b)$v_p = 0.005$, $\mu = 0.2$; (c)$v_p = 0.01$, $\mu = 0.01$. All distributions look Gaussian, as verified in the next figure.

with constant rate $\dot{\lambda} = v_p$ is applied till a final total length L_{final} is reached. In the reverse process, the end length L_{final} of the forward loading is used as the initial length and the pulling rate is flipped $\dot{\lambda} = -v_p$.

3.3.2. Distribution

Under the choice of the quadratic potential, the equilibrium free energy change of the mass-spring chain can be computed analytically with a simple quadratic form

$$\Delta F = \frac{1}{2}\frac{k}{N}\Delta L^2, \tag{3.11}$$

where $\Delta L = L - L_0$ is the elongation of the mass-spring system. This works because the entropy of a mass-spring chain with quadratic springs in equilibrium is independent of the force in the springs and depends only on the curvature of the spring potentials.

The work distributions for three different cases are presented in Fig. 3.2. Gaussian distributions are expected given the linearity of the governing equation and the potential[112], and they are observed in Fig. 3.2 and verified by studying the skewness and kurtosis in Fig. 3.3, where the two values lie always in the range of 0.00 ± 0.01 and 3.00 ± 0.02.

Note the the average value of the work deviates from the free energy change due to the irreversibility by the damping. The deviation is larger when we increase the damping coef-

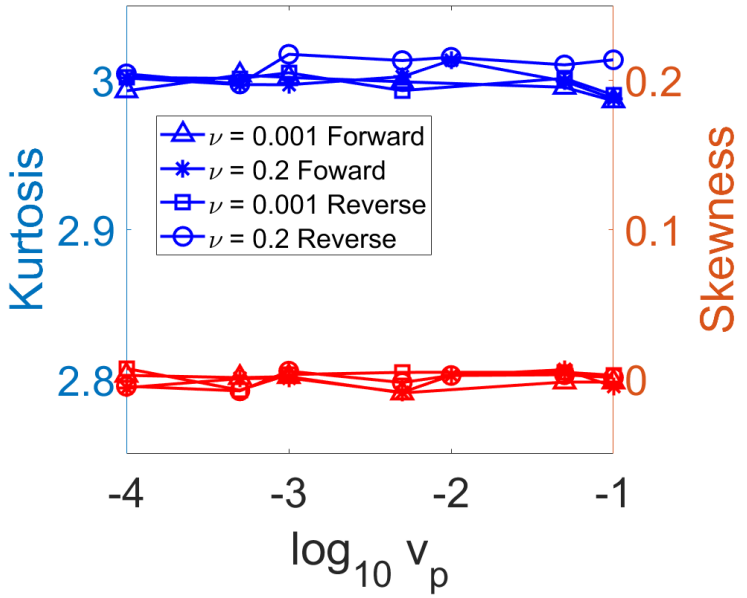

Figure 3.3: Kurtosis and skewness of work distributions at various pulling rates and viscous drags. The kurtosis is around 3 while the skewness is almost 0. This indicates that the work distribution for both forward and reverse processes is Gaussian.

ficient (Fig. 3.2(b)) or the pulling rate in the loading protocol (Fig. 3.2(c)), resulted from larger dissipation. Interestingly, there is still a small portion of the distribution lying to the left of the red dashed line, indicating that the work done for the corresponding realizations is smaller than the free energy change. However, this does not imply that the second law of thermodynamics is violated; the free energy inequality $\langle W \rangle > \Delta F$ is satisfied in an ensemble average sense, but not for individual trajectories or realizations of the process. As the systems go further away from equilibrium, these events are less likely to be observed, as is indicated in Fig. 3.2. A key message of this section is that the Clausius-Duhem[113] inequality of continuum mechanics cannot be applied to every process if the system under consideration is small enough that fluctuations play an important role.

3.3.3. Free Energy

One advantage of the Jarzynski equality is that it allows us to find the free energy change from only the work distribution, without other extra information such as material properties. Since the work distribution is confirmed Gaussian, we will make use of eqn.(3.5) to obtain

the free energy.

An alternative and equivalent way of finding free energy change is to use the Crooks fluctuation theorem eqn.(3.6). The Gaussian probability density function of work for forward and backward processes can be determined by the average and variance obtained from the numerical calculations. Fig. 3.4 (a) shows that the forward work distribution $P_f(W)$ intersects with the reverse work distribution $P_r(-W)$ at the work corresponding to the free energy change ΔF. If we plot the ratio between $P_f(W)$ and $P_r(-w)$ as a function of W, it is a straight line intersecting the x-axis at ΔF shown in Fig. 3.4(b). Under the Gaussian assumption, the work distribution is completely determined by the average and the standard deviation. Thus, by solving $P_f(W) = P_r(-W)$ one can find the free energy change explicitly as

$$\Delta F = \frac{\frac{w_f}{\sigma_f^2} + \frac{w_r}{\sigma_r^2} - \frac{\sqrt{w_f^2+2w_f w_r+w_r^2-2\sigma_f^2\log(\sigma_f/\sigma_r)+2\sigma_r^2\log(\sigma_f/\sigma_r)}}{\sigma_f\sigma_r}}{(1/\sigma_f^2 - 1/\sigma_r^2)}, \tag{3.12}$$

where w_f and w_r are the average work in the forward and reverse process while σ_f and σ_r are the corresponding variances. Note that here even the temperature information is not needed; One can solve for the temperature combining eqn.(3.12) with eqn.(3.5). The free energy change obtained by eqn.(3.12) are compared with the theoretical free energy change and the Jarzynski equality in Fig. 3.4(c).

3.3.4. Dissipation

The Jarzynski equality allows us to obtain the irreversible part of the work of the process using

$$W_{irr} = \langle W \rangle - \Delta F, \tag{3.13}$$

where the free energy change ΔF is found by eqn.(3.2). Yet, this does NOT represent the dissipation D during the process of loading; it also includes the dissipation during relaxation that happens at the final state as it reaches the final *equilibrium* state, i.e.

$$W_{irr} = D + D_r, \tag{3.14}$$

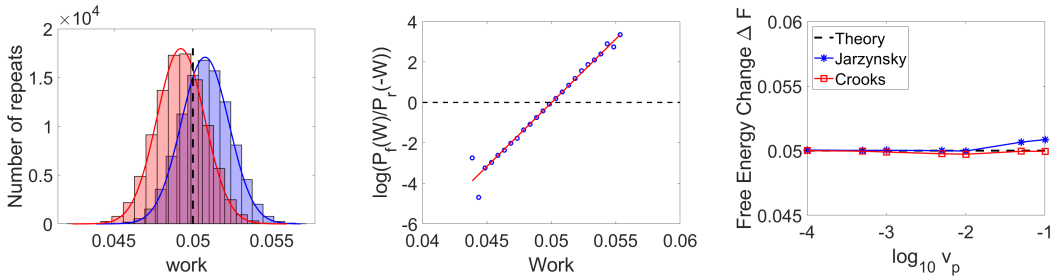

(a) (b) (c)

Figure 3.4: (a)The forward (blue) and reverse (red) work distributions cross each other at the value of free energy change 0.05. (b) $\log \frac{P_f(W)}{P_r(-W)}$ vs. W is a straight line intersecting the x-axis at $W = \Delta F$. (c) Both Jarzynski equality and Crooks fluctuation theorem give good predictions of free energy change at various velocities for a chain with identical quadratic springs.

where D_r is the dissipation that occurs during relaxation. Therefore, the Jarzynski equality does not provide us directly with the dissipation for a process without further analysis. Now, in our mass-spring system immersed in a heat bath, the only source of dissipation is viscous drag since the springs are linear, and therefore the process dissipation can be written as

$$D = \sum_i \int_0^\tau \nu \langle \dot{u}_i \rangle^2 dt, \tag{3.15}$$

which coincides with eqn.(2.24) in chapter 1. On the other hand, by energy conservation, the dissipation during relaxation is nothing but the internal energy change (it is the internal energy change because the entropy of the final state and the final equilibrium state are the same)

$$D_r = \Delta E. \tag{3.16}$$

Combining eqn.(3.5)(3.15)(3.16) with eqn.(3.14) we get

$$\frac{1}{2}\beta\sigma_W^2 = \sum_i \int_0^\tau \nu \langle \dot{u}_i \rangle^2 dt + \Delta E. \tag{3.17}$$

This equation can be seen as an extension of the energy balance method in Chapter 1. We used this equation and the energy balance method of Chapter 1 to estimate the dissipation

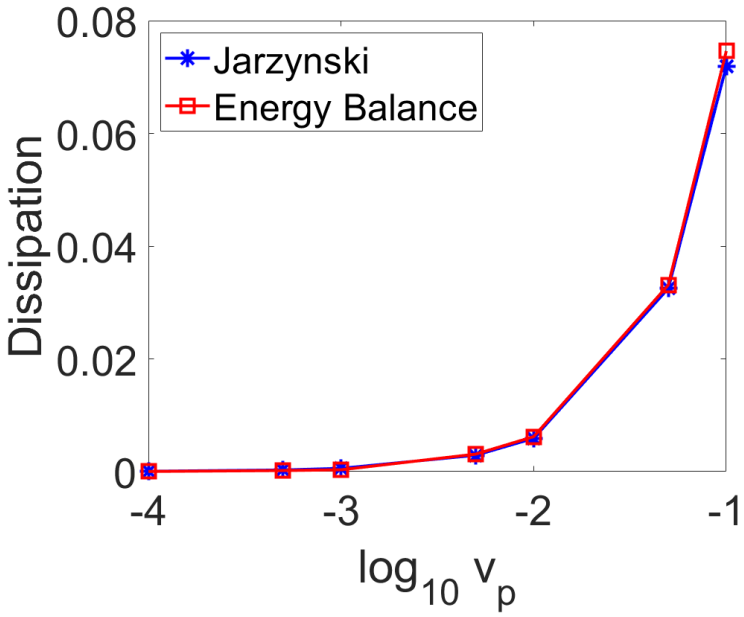

Figure 3.5: Comparison of dissipation obtained from different methods. The blue stars denote the dissipation obtained from the Jarzynski equality $W_{irr} = \frac{1}{2}\beta\sigma_W^2$, while the red squares represent that calculated using the energy balance method $D + D_r$. The two match really closely in the studied cases over a wide range of pulling velocities.

during the process over a large range of pulling velocities and the results are shown by Fig. (). There is excellent agreement between the two methods. Thus, eqn.(3.17) provides a strategy to separate the dissipation during the process and the dissipation during the relaxation from the irreversible work based on kinematic observables. Yet, many open questions still remain to be answered. Particularly, the generalization of the idea presented here to systems far from equilibrium with more dissipation mechanisms is left for future investigations.

3.4. Double-well Springs

The previous section presents the results based on a special case of Gaussian work distribution, where the dissipation is only from the viscous drag of a linear mass-spring chain. We showed in that section that two different fluctuation theorems (Jarzynski equality and Crooks fluctuation theorem) allowed us to accurately estimate the free energy change in going from state A to state B. We therefore would like to investigate the application of fluctuation theorems to more general systems with multiple mechanisms of dissipation, as

was done in reference[26, 38]. In particular, we would like to obtain dissipation in a system with phase transition by means of the Jarzynski equality. If this can be accomplished by using an equality version of the second law of thermodynamics then it will provide us a means to estimate the kinetics of phase transition fronts directly rather than specifying it as constitutive information from outside.

To this purpose, we study the same over-damped mass-spring chain, but with a double-welled potential similar to the one described in Chapter 1, namely:

$$V = \begin{cases} \frac{1}{2}(u-1)^2, & u < 2.5, \\ \frac{1}{2}(u-4)^2, & u \geq 2.5. \end{cases} \tag{3.18}$$

A spring is assumed to be in the high strain phase when $u > 2.5$ and in low strain phase otherwise. We do similar numerical tests as in the previous section. We start with all springs in low strain phase and pull the chain to a length such that all springs are in high strain state in every realization of the pulling process. This is repeated over $N_R = 10^5$ realizations. During this process, a phase transition from low strain state to high strain state will occur which brings a second source of dissipation other than viscous drag. Specifically, we would like the phase transition dominated by a propagating interface instead of thermal nucleation because we are interested in the dissipation at the phase transition front. In the numerical simulation, we perform pulling tests at various dimensionless temperatures and pulling rates. The dimensionless temperature is defined as $T^* = \frac{k_B T}{k a_0^2}$ where a_0 is the unstrained spring length. The initial state is in equilibrium with the heat bath while the end state is not required to be in equilibrium with the bath. We choose the end state for different pulling velocities differently. Although there is no exact analytical expression for the equilibrium free energy change of the chain, it can be approximated as the internal energy change when far from the phase transition. This is because the spring constant for both phases chosen to be the same and therefore the entropy change is zero between two states in which all springs are in the low strain phase or all in the high strain phase. Note that there is no

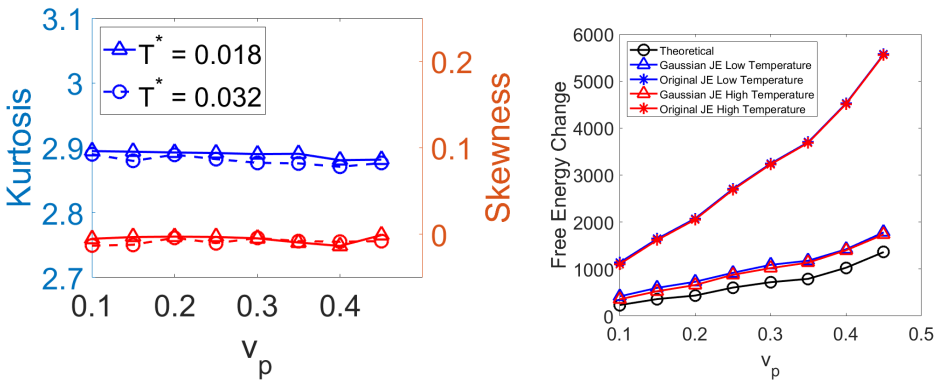

Figure 3.6: (a)Kurtosis and skewness of work distributions at various pulling velocities and temperature. The kurtosis is slightly smaller than 3 while the skewness is almost 0. This indicates that the work distribution is no longer Gaussian, although the distribution is symmetric. (b) Comparison of free energy change obtained by different methods at various pulling rates and temperature. The dimensionless temperature is defined as $T^* = \frac{k_B T}{k a_0^2}$ where a_0 is the unstrained spring length. The least error in the free energy estimated by the Jarzynski equality occurs at high temperatures and low pulling velocities.

configurational entropy associated with the distribution of springs if the phase fraction is either zero or one. The end state for different pulling velocities are not of the same length; instead, we stop when the phase transition finishes, that is when the phase transition front reaches the other end and disappears.

We first examine the Gaussianity of the data by calculating the skewness and kurtosis of the work distribution. In Fig. 3.6(a), we notice that the skewness of our work distribution is still in the range of 0.00 ± 0.01, which indicates that the distribution is still symmetric even when the potential is double-welled. However, the kurtosis deviates from 3. Further, the deviation of kurtosis increases as the temperature increases. This implies that the work distribution is no longer Gaussian, although it is not too different from Gaussian.

We then compare the free energy change obtained from the Jarzyanski equality with the theoretical approximation. The results are presented in Fig. 3.6(b). Unfortunately, neither the original Jarzynski equality nor the Gaussian approximation can give a good match with the theoretical expression; particularly, the results of the original Jarzynski relation

eqn.(3.2) deviate a lot from the theoretical estimate. The error in the estimate of the free energy change from the Jarzynski equality seem to be the least at low pulling velocities and high temperature. There are multiple reasons for this bad behavior. First, rare events are hard to capture. Unlike the previous linear spring case, the work distribution deviates from the theoretical free energy change so much that all the data points lie to the right of it. This means that rare events in which the work done is less than the free energy change are not captured well in our simulations. However, the tail part of the distribution where $W < \Delta F$ contributes most to "drag" the left hand side of eqn.(3.2) to the free energy change. Without these rare observations the free energy change from eqn.(3.2) is then naturally larger. Second, as the distribution deviates from Gaussianity, higher order terms of the cumulent expansion in eqn.(3.4 should be included to correct the deviation. Lastly, the ergodicity of the initial state is violated: we never observe any spring in high strain state initially; instead, the system is trapped in a local minimum where all springs are in the low strain state. Thus, one of the assumptions of the Jarzynski equality (that the initial state is in equilibrium with the bath) is violated. The same is true if we equilibrate the chain in the end state, although equilibration is not required in applying Jarzynski equality.

Thus, a number of issues must be addressed in order to use fluctuation theorems to capture the kinetics of phase transitions.

3.5. Outlook

In this chapter, we extract equilibrium and non-equilibrium information from a system using fluctuation theorems. We show the connection between a fluctuation theorem and a transport coefficient through the derivation of a Green-Kubo relation. Then, we apply the methods to a mass-spring system simulated by over-damped Langevin dynamics. We start by stretching and compressing a chain of linear springs and show perfect match between theoretical analysis and predictions by fluctuation theorems such as those of Jarzyanski and Crooks. In this case, the free energy change can be obtained without knowing the details of the system but only through the work distribution. However, when phase transition

is introduced through a spring with double-welled potential, the prediction by fluctuation theorem deviates from the theoretical formula.

Further investigations are needed due to the flaw in our phase transition calculations. Some major challenges still need to be solved when applying fluctuation theorems to systems with more complicated dissipation mechanisms. Firstly, capturing rare events in highly non-Gaussian probability distributions is difficult, particularly for large systems with heavily tailed distributions. More advanced techniques for capturing the tail distribution such as those of Mohamad and Sapsis[114], are required. Secondly, the fact that the fluctuation theorems behave well in cases with a single dissipation mechanism but fail in the more complicated cases calls for alternate strategies, using for instance, ideas from Li et al.[115] and Montefusco et al.[116]. Finally, the ergodicity of the initial state or the process is often violated during phase transition phenomena since the system may become trapped in local minima. Alternate fluctuation theorems, such as Alemany et al.[117], are needed in these cases.

CHAPTER 4

Fibrous gels modeled as fluid filled continua with double-well energy landscape

This chapter is based on work published in [118].

4.1. Introduction

Fibrous gels are common biological materials. For example, blood clots consist of an isotropic network of fibers about 200 nm in diameter filled with fluid [119]. Cartilage consists of an isotropic network of collagen fibers about 20 nm in diameter filled with fluid [120]. Fibrin and collagen based bio-materials are used as scaffolding in tissue engineering applications [121]. The fluid volume fraction in collagen gels is around 80% while that in plasma blood clots is about 99% justifying their treatment as gels. The network of solid filaments that endows these gels with structural integrity is formed by the polymerization of protein, but it is qualitatively different from the underlying network in many commonly used synthetic hydrogels [50, 122]. Collagen and fibrin fibers appear straight (like rods) when viewed in a confocal microscope [121]; this is in contrast to randomly fluctuating polymer chains that comprise the network of synthetic gels. When subjected to compression fibrin and collagen fibers buckle, and this leads to a different constitutive response compared to the neo-Hookean elasticity of networks of polymer chains [52].

We are particularly interested in the compression of fibrous gels in this manuscript. Experiments on fibrin and collagen gels have revealed that their compression response is hysteretic [52, 120]. We will describe features seen in the compression of fibrin gels since these are familiar to us, although similar observations have been made for collagen gels. Fibrin gels can be formed between the plates of a parallel plate rheometer equipped with a confocal microscope as shown recently by Kim *et al.*[57] and Liang *et al*[52]. When the top plate of the rheometer is moved downwards the stress increases linearly with the strain for small strains. When a critical strain (about 0.05) is reached fibrin fibers buckle and come into

contact with each other resulting in a densified network near the top plate. Fibers near the bottom plate remain straight and the network there is rarefied; an interface separating the two phases can be clearly seen in the confocal images. As the top plate moves down the interface separating the densified and rarefied phases moves towards the bottom plate converting more of the network into the densified phase. During this regime the stress increases slowly and there is a plateau in the stress-strain curve as fluid leaks out of the gel and more and more fibers buckle. Eventually, the interface reaches the bottom plate and the whole network is densified with a large number of contacts between the buckled fibers. Further compression leads to a steeply rising stress. During unloading, as the top plate is moved upwards the compressive stress declines steeply and when it reaches near zero (usually a tensile value) another plateau is observed in the stress-strain curve as the fibers unbuckle and the network goes back into a rarefied phase. During this lower plateau fluid is sucked back into the network, and finally the gel reaches its original state ready for another cycle of compression and decompression. Some damage to the network occurs in the first cycle and its stress-strain curve is different from all subsequent cycles whose stress-strain curves sit on top of each other.

A continuum theory of phase transitions [17] has been used to describe the hysteretic stress-strain response of fibrin gels [52] and carbon-nanotube (CNT) networks [123]. The stress-strain relations for the rarefied and densified phases of the underlying network were borrowed from those of foams [124, 125] and dense yarn [126, 127], respectively. Simple kinetic laws for the evolution of phase fractions were used to capture the plateaus in the stress-strain curves and these worked well for a broad range of strain-rates for CNT networks (which contained no liquid) and low strain-rates for fibrin gels. At higher strain-rates the plateaus during interface propagation became steeper in experiments on fibrin gels, but the kinetic laws used in previous work could not capture this feature [123, 128]. The reason could be that the motion of the fluid in the gel was treated in a rudimentary manner in those works. At high strain-rate fluid flow is expected to make a large contribution to the stress, necessitating the use of a chemo-elastic model. Indeed, continuum chemo-elastic models have

been successfully applied to capture the compression response of polymeric gels [48, 49]. Our primary goal in this paper is to adapt this continuum chemo-elastic model to fibrous gels that can exist in rarefied and densified phases at the same state of stress. This implies that the Helmholtz free energy density of the underlying solid network must have two wells – a low-strain well corresponding to the rarefied network and a high-strain well corresponding to the densified network, just as in the continuum theory of phase transitions [17]. This requires significant modification of the continuum chemo-elastic model [47] because the stored energy function of its polymeric solid phase has only a single well [129].

Our secondary goal is to reduce the fully three-dimensional continuum theory to a one-dimensional form that can be treated without resorting to finite element calculations involving poro-elasticity [130, 131]. One reason to do so is that compression experiments on fibrin (and collagen) gels tend to be axisymmetric (with z-axis as the symmetry axis) with the important stresses and strains corresponding to the z-direction. Another reason is that it is cumbersome to implement a fully three-dimensional model of phase transitions coupled to a large deformation poro-elasticity theory in commercially available finite element software. The process of reaching a one-dimensional model necessarily involves some approximations, but we show here that the result is a tractable model amenable to numerical integration (with no need for finite element calculations) that can capture most of the observations in experiments.

The chapter is arranged as follows. In section 3.2 we set up the continuum theory following closely the work of Chester and Anand [47]. In section 3.3 we specialize the fully three-dimensional theory to one dimension and demonstrate how it can be solved numerically to capture the hysteretic stress-strain response of fibrous gels. In section 3.4 we specialize to an axisymmetric model, which is more complex than the one-dimensional model of section 3.3, but is still numerically solvable without recourse to finite elements. Again, we show that the axisymmetric model can recover experimental observations. In section 3.5 we present experimental evidence for some key features seen in our results of sections 3.3 and 3.4, then

we conclude in section 3.6.

4.2. Continuum modeling

Our theoretical framework is based on the theory by Chester and Anand [47] with one major modification that has to do with the stored energy function for the underlying fibrous network in the gel. Consider a dry fibrous network $\mathcal{B}$ occupying a reference volume Ω, and let $\mathbf{X}$ denote a material point. The motion of the body is given by a smooth mapping $\mathbf{x} = \mathcal{X}(\mathbf{X}, t)$. Following Chester and Anand [47] we assume the deformation gradient, given by $\mathbf{F} = \nabla\mathcal{X}$, has the decomposition

$$\mathbf{F} = \mathbf{F}^e\mathbf{F}^s, \text{ with } \mathbf{F}^s = \lambda^s\mathbf{I}, \ \lambda^s > 0. \tag{4.1}$$

Here $\mathbf{F}^e$ represents a mechanical elastic distortion; $\mathbf{F}^s$ represents the local distortion due to swelling, and λ^s is the swelling stretch. It is assumed that the fibrous network and the fluid are both incompressible, and the swelling stretch is entirely due to the change in the fluid content. Therefore, mass conservation of the fibrous gel can be expressed as:

$$\det \mathbf{F} = 1 + vc_{\mathrm{R}}, \tag{4.2}$$

where v denotes the volume of one fluid molecule, and $c_{\mathrm{R}}(\mathbf{X}, t)$ is the number of fluid molecules per unit reference volume. Mass conservation of the fluid boils down to

$$\dot{c}_{\mathrm{R}} = -\mathrm{Div}\ \mathbf{j}_{\mathrm{R}}, \tag{4.3}$$

where $\mathbf{j}_{\mathrm{R}}$ denotes the fluid flux, measured per unit reference area per unit time. For low Reynolds number flow, $\mathbf{j}_{\mathrm{R}}$ follows Darcy's law

$$\mathbf{j}_{\mathrm{R}} = -m(\mathcal{I}_{\mathbf{C}^e}, c_{\mathrm{R}})\nabla\mu, \tag{4.4}$$

Here μ is the chemical potential. m is mobility of the liquid, $\mathcal{I}_{\mathbf{C}^e} = \{I_1(\mathbf{C}^e), I_2(\mathbf{C}^e), I_3(\mathbf{C}^e)\}$ is the set of invariants of $\mathbf{C}^e$. Given material isotropy and frame indifference, m is a scalar determined by the principal invariants of $\mathbf{C}^e = \mathbf{F}^{e\mathrm{T}}\mathbf{F}^e$ and c_R. Here we assume the dependence of m on c_R is a power-law

$$m \propto c_\mathrm{R}^n. \tag{4.5}$$

Combining eqn.(4.4) with eqn.(4.3) gives

$$\dot{c}_\mathrm{R} = \mathrm{Div}(m\nabla\mu). \tag{4.6}$$

Last, since time scales associated with fluid diffusion are usually longer than those associated with wave propagation, we neglect all inertial effects. Then, balance of forces in the reference configuration gives

$$\mathrm{Div}\ \mathbf{T}_\mathrm{R} + \mathbf{b}_\mathrm{R} = \mathbf{0}. \tag{4.7}$$

Here $\mathbf{T}_\mathrm{R}$ is the first Piola-Kirchhoff stress (P-K stress, henceforth), which represents the true traction force per unit reference area, and $\mathbf{b}_\mathrm{R}$ is the body force.

The P-K stress $\mathbf{T}_\mathrm{R}$ in eqn.(4.7) and the chemical potential μ in eqn.(4.6) are constitutively given by a free energy density function $\psi_\mathrm{R}(\mathbf{C}^e, c_\mathrm{R})$ through

$$\mathbf{T}_\mathrm{R} = 2\mathbf{F}^e \frac{\partial \psi_\mathrm{R}(\mathbf{C}^e, c_\mathrm{R})}{\partial \mathbf{C}^e}\mathbf{F}^{s-T} - P\mathbf{F}^{-T}, \tag{4.8}$$

$$\mu = \frac{\partial \psi_\mathrm{R}(\mathbf{C}^e, c_\mathrm{R})}{\partial c_\mathrm{R}} + \bar{p}v. \tag{4.9}$$

Here $\bar{p} := -\frac{1}{3}\det\mathbf{F}^e \mathrm{tr}\mathbf{T}$ defines a mean normal pressure. $\mathbf{T} = (\det\mathbf{F})^{-1}\mathbf{T}_\mathrm{R}\mathbf{F}^T$ is the Cauchy stress tensor. Due to the incompressibility constraint, we introduce a Lagrange multiplier P, which will be determined by the solution to the mechanical boundary value problem. We interpret here the Lagrange multiplier P as the osmotic pressure, which increases the chemical potential for the liquid to enter the gel.

In order to specialize the free energy function ψ_R, we follow the assumption of Flory, who

gives the decomposition

$$\psi_{\mathrm{R}}(\mathbf{C}^e, c_{\mathrm{R}}) = \mu^0 c_{\mathrm{R}} + \psi_{\mathrm{R,mixing}}(c_{\mathrm{R}}) + \psi_{\mathrm{R,mechanical}}(\mathbf{C}^e, c_{\mathrm{R}}). \tag{4.10}$$

Here μ^0 is the chemical potential of the unmixed pure liquid. In eqn.(4.10) $\psi_{\mathrm{R,mixing}}(c_{\mathrm{R}})$ is the change in free energy due to mixing of the liquid with the polymer network. We adopt the form of Flory-Huggins theory for the mixing [129]

$$\psi_{\mathrm{R,mixing}} = \frac{k_B T}{v}\frac{1}{\phi}\left((1-\phi)\ln(1-\phi) + \chi\phi(1-\phi)\right), \tag{4.11}$$

where k_B is the Boltzmann constant, T is the absolute temperature, $\phi := (1 + v c_{\mathrm{R}})^{-1}$ is the solid volume fraction, and χ is a dimensionless quantity characterizing the difference between the interaction energy of liquid molecule immersed in the pure polymer compared with interaction energy in the pure liquid.

$\psi_{\mathrm{R,mechanical}}(\mathbf{C}^e, c_{\mathrm{R}})$ is the contribution to the change in the free energy due to the deformation of the polymer network. Let $\lambda := \frac{1}{\sqrt{3}}\sqrt{\mathrm{tr}\mathbf{C}} = \frac{1}{\sqrt{3}}(1+vc_{\mathrm{R}})^{1/3}\sqrt{\mathrm{tr}\mathbf{C}^e}$ be the stretch of the fiber network. A typical implementation of $\psi_{\mathrm{R,mechanical}}(\mathbf{C}^e, c_{\mathrm{R}})$ for neo-Hookean material is

$$\psi_{\mathrm{R,mechanical}}(\mathbf{C}^e, c_{\mathrm{R}}) = \frac{1}{2}G_0\left(3\lambda^2 - 3 - 2\ln\det\mathbf{F}\right), \tag{4.12}$$

where G_0 is the shear modulus. The free energy expression of eqn.(4.12) cannot characterize two phase behavior of a fibrous network that can exist in a rarefied phase (with straight fibers) and densified phase (with buckled fibers) at the same stress. Hence, we propose a free energy with quartic λ dependence, i.e.

$$\psi_{\mathrm{R,mechanical}}(\mathbf{C}^e, c_{\mathrm{R}}) = f_4(\lambda) - G_0\ln\det\mathbf{F}, \tag{4.13}$$

The coefficients of f_4 are chosen such that it has two minima corresponding to two phases.

In particular,

$$f_4(\lambda) = c_0 + c_1\lambda + \frac{1}{2}c_2\lambda^2 + \frac{1}{3}c_3\lambda^3 + \frac{1}{4}c_4\lambda^4 = \frac{d_2}{2}(\lambda-1)^2 + \frac{d_3}{3}(\lambda-1)^3 + \frac{d_4}{4}(\lambda-1)^4,$$

where c_0, c_1, c_2, c_3, c_4 and d_2, d_3, d_4 are all constants. Note that $f_4(\lambda) = 0$ at $\lambda = 1$ and the extrema of $f_4(\lambda)$ occur at $\lambda = \lambda_1 = 1$, $\lambda = \lambda_2 = 1 + \frac{-d_3 - \sqrt{d_3^2 - 4d_2d_4}}{2d_4}$ and and $\lambda = \lambda_3 = 1 + \frac{-d_3 + \sqrt{d_3^2 - 4d_2d_4}}{2d_4}$. d_2, d_3, d_4 should be chosen in such a way that the extrema occur at real values of λ. Then, $\lambda = \lambda_1$ is the well corresponding to the dry state in which the fibers are all collapsed on themselves (as in the densified phase), and the other well at a larger $\lambda = \lambda_3$ corresponds to the swollen state in which the fibers are straight (as in the rarefied phase). Then, $f_4(\lambda)$ is valid in the interval $\lambda_1 \leq \lambda \leq \lambda_3$ which corresponds to compression of the network. A double-well free energy as a quartic polynomial in strain was first proposed for fibrin networks in Kim *et al.* [57]. We do not use their values of the coefficients here; instead we take $d_2 = 6.4 \times 10^5$ Pa, $d_3 = -1.6 \times 10^5$ Pa, and $d_4 = 1 \times 10^4$ Pa. We show below that qualitative characteristics of the stress-strain curves based on these values of d_2, d_3 and d_4 are similar to those measured for fibrin and CNT networks.

Let us assume that the deformation gradient takes the simple form $\mathbf{F} = \mathrm{diag}[\lambda_1, 1, 1]$. In this case $\phi = \lambda_1^{-1}$ and $\lambda = \frac{1}{\sqrt{3}}\sqrt{\lambda_1^2 + 2}$. Assuming that the solid network and the fluid are both incompressible the Piola stress T_{11} is given by:

$$T_{11} = \frac{1}{3\lambda\phi}\left(d_2(\lambda-1) + d_3(\lambda-1)^2 + d_4(\lambda-1)^3\right) - P\phi, \tag{4.14}$$

where P is a Lagrange multiplier that enforces the incompressibility constraint as in eqn.4.8. We will let ϕ vary in the range $0.049 \leq \phi \leq 1$, with $\phi = 0.05$ representing the stress-free state of the gel. Thus, P is determined by setting $T_{11} = 0$ at $\phi = 0.05$. Such low solid volume fractions in the stress-free state are typical of fibrin gels [52]. In experiments on fibrin gels (also CNT networks) the compressive strain ε is measured with respect to this stress free state. Thus, for our choice of parameters $\varepsilon = 1 - 0.05\lambda_1$. In Fig. 4.1 we plot the stress $-T_{11}$ (positive in compression) as a function of ε. The curve is up-down-up with T_{11} a local

maximum at $(\varepsilon, T_{11}) = (0.218, 404)$ and T_{11} local minimum at $(\varepsilon, T_{11}) = (0.685, -23)$. Note that T_{11} is tensile at the local minimum which is consistent with experiments on fibrin and CNT networks [52, 123]. The physical reason for this is that fibers adhere to each other in the densified phase and a small tensile force must be applied to unstick and straighten them so that they go back to the rarefied phase. The range $\varepsilon \leq 0.218$ represents the rarefied phase of the solid network and the range $\varepsilon > 0.685$ represents the densified phase. This is similar to the experiments of Kim *et al.* [57] in which the rarefied phase corresponds to $\varepsilon < 0.05$ and the densified phase to $\varepsilon > 0.7$. In both these regions the slope of the stress-strain curve is positive, implying that the material is stable in these phases. For a state of stress in the range $-23 \leq T_{11} \leq 404$ KPa the solid network can co-exist in the densified and rarefied phases. For example, at $-T_{11} = 100$KPa the two values of ε are 0.027 in the rarefied phase and 0.819 in the densified phase.

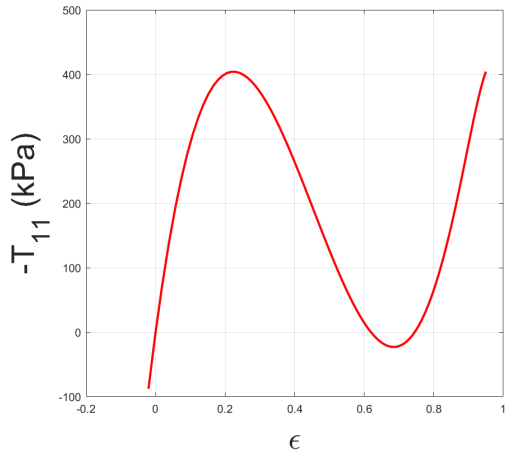

(a)

Figure 4.1: Compressive stress $-T_{11}$ plotted as a function of compressive strain ε using $d_2 = 6.4 \times 10^5$ Pa, $d_3 = -1.6 \times 10^5$ Pa and $d_4 = 1 \times 10^4$ Pa in eqn.4.13. The gel is the assumed to be stress-free ($T_{11} = 0$) at $\phi = 0.05$. The stress-strain curve is up-down-up, typical of phase-changing materials. The gel is in a rarefied phase for $\varepsilon < 0.218$ and in a densified phase for $\varepsilon > 0.685$.

We have made a major departure from the theory of Chester and Anand [47] by assuming a double-well Helmholtz free energy landscape for the solid network in the gel. We will

show in the remainder of this paper that this choice of Helmholtz free energy will give rise to many of the same qualitative behaviors as seen in experiments on fibrous gels. To sum up, the governing partial differential equations consist of eqn.(4.2), eqn.(4.6) and eqn.(4.7), where the P-K stress T_{R} and the chemical potential μ are given by the constitutive relations eqn.(4.8) and eqn.(4.9).

4.3. One-dimensional compression

We now apply our theory to one dimensional cases. Consider a cylinder of fully swollen gel placed in a rigid container with radius R and height H. The gel is constrained by the wall of the container in the radial direction $\mathbf{e}_2$, $\mathbf{e}_3$, and the stretch, and thus the flow, is only in the axial direction $\mathbf{e}_1$. We assume the wall is perfectly smooth, thus no shear force is induced by the wall. In this case, the motion of the body is given by

$$x_1 = x_1(X_1, t),\ x_2 = X_2,\ x_3 = X_3, \tag{4.15}$$

with the deformation gradient being diagonal $\mathbf{F} = \mathrm{diag}\{\lambda_1, 1, 1\}$, where $\lambda_1 = \frac{\partial x_1}{\partial X_1}$. From eqn.(4.2) we have $\phi = \lambda_1^{-1}$.

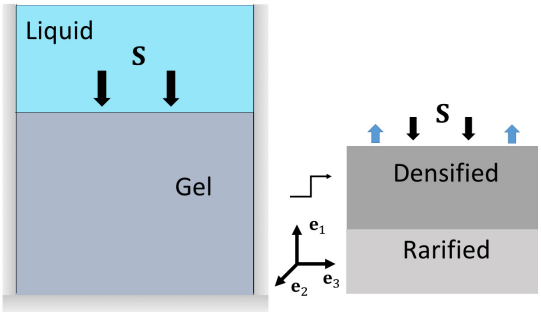

Figure 4.2: A schematic of the 1D compression problem. The left figure shows that the fluid reservoir is in contact with the gel on the top boundary where a stress S (black arrows) is applied. The right figure shows the gel separated into densified and rarefied phases with an interface separating them. The blue arrows on the top show that fluid can go in and out of the gel only from the top boundary.

.

4.3.1. Stress control

We first consider the case with prescribed stress at the boundary. Suppose a stress S is applied uniformly in the axial direction to compress the gel (see Fig. 4.2), i.e.

$$\mathbf{e}_1 \cdot (\mathbf{T}_R \mathbf{e}_1) = -S, \quad \mathbf{e}_1 \cdot (\mathbf{T}_R \mathbf{e}_2) = \mathbf{e}_1 \cdot (\mathbf{T}_R \mathbf{e}_3) = 0 \tag{4.16}$$

at top and bottom boundary. In this case we can establish a one-dimensional equation in terms of ϕ in the following way. The force balance equation eqn.(4.7) in the axial direction gives $(T_R)_{11} = -S$ since $\mathbf{F}$ is diagonal. Combining this with the constitutive equations eqn.(4.8) and eqn.(4.9) we can eliminate P and find the chemical potential μ as a function of ϕ:

$$\begin{aligned}\mu &= \mu^0 + k_B T(\ln(1-\phi) + \phi + \chi\phi^2) - vG_0\phi + \frac{vf'(\lambda)}{3\lambda}\phi^{-1} - vS \\ &= \mu^0 + k_B T(\ln(1-\phi) + \phi + \chi\phi^2) - vG_0\phi + \frac{1}{3}\phi^{-1}(c_1\lambda^{-1} + c_2 + c_3\lambda + c_4\lambda^2) - vS,\end{aligned} \tag{4.17}$$

where $\lambda = \frac{1}{\sqrt{3}}\sqrt{\phi^{-2}+2}$. Combining eqn.(4.17) with eqn.(4.6) a non-linear differential equation in ϕ is obtained:

$$\frac{\partial \phi}{\partial t} = -v\phi^2 \frac{\partial}{\partial X}\left(m(\phi)\frac{\partial}{\partial X}\mu(\phi)\right). \tag{4.18}$$

Now we assume that the top plate is permeable while the bottom is impermeable to fluid flow, i.e.

$$\mu(\phi) = \mu_0 \text{ at } X_1 = H; \quad m(\phi)\frac{\partial \mu(\phi)}{\partial X} = 0 \text{ at } X_1 = 0. \tag{4.19}$$

With these boundary conditions and the initial condition that the gel is fully swollen at $t = 0$, the system is closed and $\phi(X_1, t)$ can be solved numerically. Particularly, since eqn.(4.18)

takes the form

$$c(X,t,u,\frac{\partial u}{\partial X})\frac{\partial u}{\partial t} = X^{-m}\frac{\partial}{\partial X}\left(X^m f(X,t,u,\frac{\partial u}{\partial X})\right) + s(X,t,u,\frac{\partial u}{\partial X}),$$

it can be solved by the MATLAB 'pdepe' solver.

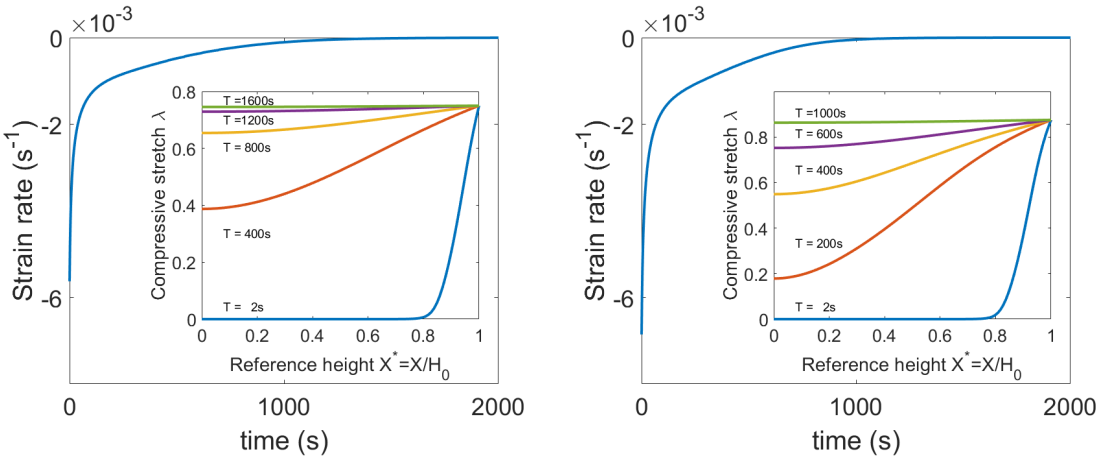

Figure 4.3: The strain rates and compressive stretch profiles under different stress boundary conditions at (a) $S = 1.8$MPa and (b) $S = 18$MPa for the one-dimensional problem depicted in Fig. 4.2. In both cases the strain rate drops with time. The strain profiles depicted in the insets of both figures exhibit a diffusive behavior.

.

To illustrate the calculations, we perform compression of a gel at two different applied stresses $S = 1.8MPa$ and $S = 18MPa$. Fig. 4.3 shows the strain rate at the top plate and the compressive stretch profile throughout the gel under two different applied stresses. Here the strain rate $\dot{\gamma} := V/H_0$ where V is the velocity of the top plate and H_0 is the initial height of the sample. The compressive stretch is $\eta = 1 - \lambda_1/\lambda_1^0$, where $\lambda_1^{(0)}$ is the stretch in the fully swollen gel. In such settings the initial value of η is 0 and for dried gel $\eta = 0.9$. In both cases the strain rate decreases monotonically and reaches an equilibrium state in the end; the higher the applied stress is, the faster the gel is squeezed. The stretch profile shows a diffusive behavior as seen from the insets of the two panels. No obvious interface propagation is observed.

One will notice that if we assume instead that the top plate is permeable and the bottom plate is impermeable, then by the symmetry of the system the strain profile is just $\lambda_1(H - X_1, t)$ where $\lambda_1(X_1, t)$ is the stretch profile in Fig. 4.3.

4.3.2. Velocity control

Now we consider the case with velocity boundary conditions, i.e. we fix the bottom plate and apply a constant velocity condition to the top plate:

$$x_1(0,t) = 0; \quad x_1(H,t) = H - Vt. \tag{4.20}$$

In this case we would like to establish an equation for the displacement $x_1(X_1, t)$. Note that we cannot directly solve the equation obtained through replacing λ_1 in the previous problem by $\lambda_1 = \frac{\partial x_1}{\partial X_1}$. Such an equation, which is in the form

$$\frac{\partial}{\partial t}\frac{\partial x_1}{\partial X_1} = -\frac{1}{v}\frac{\partial}{\partial X_1} j_1(\frac{\partial x_1}{\partial X_1}, \frac{\partial^2 x_1^2}{\partial X_1}; S), \tag{4.21}$$

is numerically unstable. To address this issue, we make use of the continuity of x_1 and integrate over X_1 to get:

$$(v\frac{\partial x_1}{\partial t} + j)\Big|_{X_1^*}^{X_1} = 0. \tag{4.22}$$

Here we assume the same boundary conditions as in eqn.(4.19). Integrating from the boundary at $X_1^* = 0$, with known fluid flux, to X_1, which is an arbitrary location in the reference configuration, we get

$$\frac{\partial x_1}{\partial t} = \frac{m}{v}\frac{\partial \mu}{\partial X}\left(\frac{\partial x_1}{\partial X}; S\right). \tag{4.23}$$

One will notice immediately that if we integrate through the entire body, then eqn.(4.22) gives the mass conservation $vV + J = 0$. Here V is the rate of compression and J is the outward liquid flux. This is a natural result of the incompressibility of the liquid and the fiber network. In eqn.(4.22), the applied stress S is yet unknown. It can be solved by studying the permeable boundary with $\mu = \mu_0$. In fact, by combining eqn.(4.8) and eqn.(4.9) with eqn.(4.13), S is decoupled from eqn.(4.22) and it thus can be solved numerically. Same as

eqn.(4.18), we use the MATLAB 'pdepe' solver to integrate this equation.

We conduct compression and decompression at rates of $\dot{\gamma} = 0.05\text{s}^{-1}$ and $\dot{\gamma} = 0.0005\text{s}^{-1}$. For decompression, we use the end state of the compression as the initial condition and decompression proceeds at the same rate as compression, except the plate is moved up, not down. This corresponds to an immediate pulling after compression without equilibration.

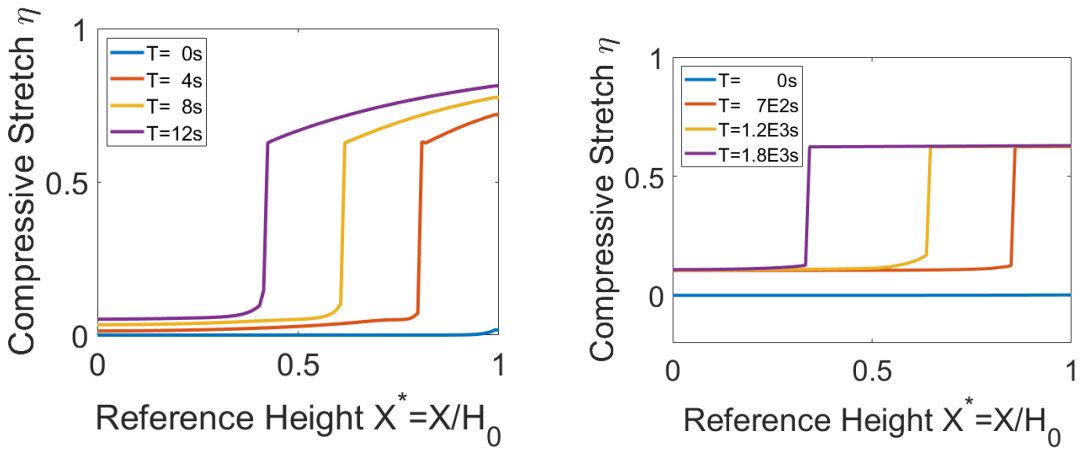

(a) (b)

Figure 4.4: Stretch profile for the compression process at a rate of (a) $\dot{\gamma} = 0.05\ \text{s}^{-1}$ and (b) $\dot{\gamma} = 0.0005\ \text{s}^{-1}$. We notice an interface appearing near the top plate and moving towards the bottom. The stretch profile is diffusive for high rate and (almost) piecewise constant for low rate. This type of stretch profiles are in agreement with experiments in Liang *et al.* [52].

.

For compression under both high and low rate (see Fig. 4.4), we observe an interface appearing at the top moving plate and propagating towards the bottom. Ahead and behind the interface, the stretch shows an obvious diffusive profile for high rate, and remains almost a constant for low rate. In the decompression process (Fig. 4.5), we notice that there is a second interface appearing from the moving plate, and the first interface formed in the compression stays almost stationary. A second interface was not reported in the experiments of Kim *et al.* [57] or Liang *et al.* [52] likely because they focused on interface propagation only during compression. The stress vs. compressive strain relation shows a clear hysteresis due to dissipation associated with the fluid flow. We find a plateau region for low rate

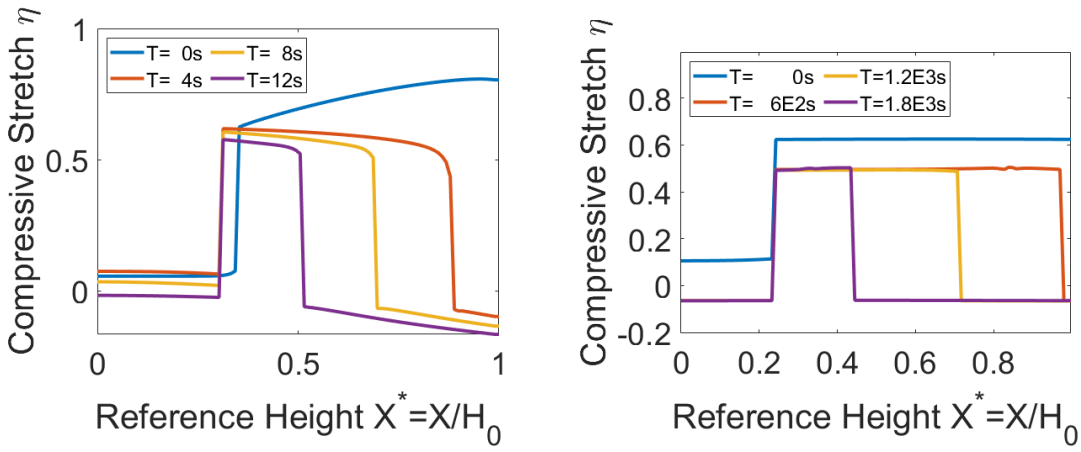

(a) (b)

Figure 4.5: Stretch profile for the decompression process at a rate of (a) $\dot{\gamma} = 0.05$ s^{-1} and (b) $\dot{\gamma} = 0.0005$ s^{-1}. We notice a second interface appearing from the top plate and moving towards the bottom. This is a falsifiable prediction from our theory that can be confirmed in experiments.

.

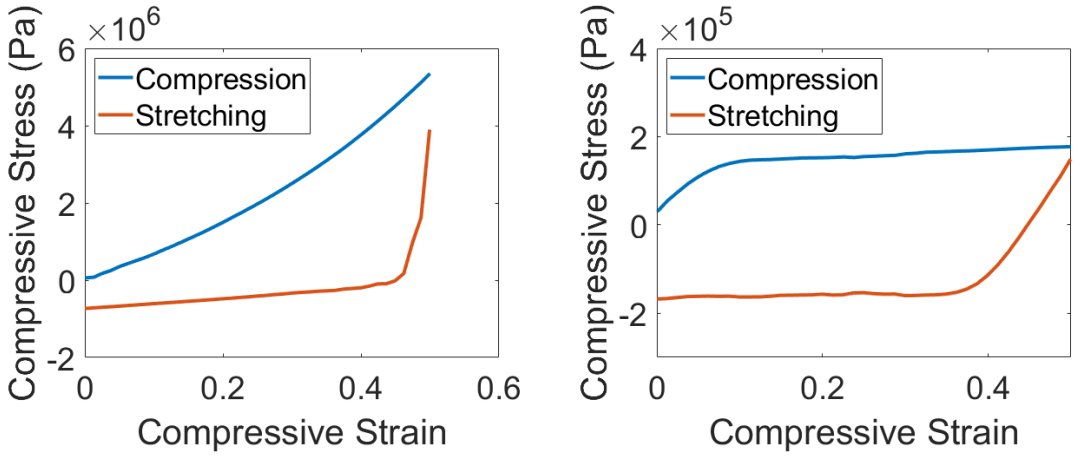

(a) (b)

Figure 4.6: Compressive stress vs. strain relation for (a) $\dot{\gamma} = 0.05$ s^{-1} and (b) $\dot{\gamma} = 0.0005$ s^{-1}. Hysteresis is observed at both high rate and low rate. The stresses are tensile in the bottom plateau, consistent with experiments in Liang *et al.* [52]. The shapes of the hysteresis loops are also similar to experiments in Liang *et al.*

.

compression corresponding to phase boundary propagation, while in high rate compression the plateau has a significant positive slope that depends on the rate of compression. The

piecewise constant strain profiles and flat plateaus are also observed in one-dimensional axial deformation of a bar made of phase transforming material [17]. Liang *et al.* had exploited this observation to model the compression behavior of fibrin gels as a phase-transition[52].

4.4. Three-dimensional axially symmetric problem

In the three-dimensional set up, we assume a cylinder of fully swollen gel of radius R and height H is placed between two impermeable parallel plates immersed in fluid as shown in Fig. 4.7. At the top and bottom boundaries, the gel is attached to the wall such that only displacement in the axial direction $\mathbf{e}_1 = \mathbf{e}_z$ is possible. In cylindrical coordinates, we assume the motion of the body takes the following form:

$$x_z = g(z,t); \quad x_\theta = 0; \quad x_r = r(1 + q(z,t)). \tag{4.24}$$

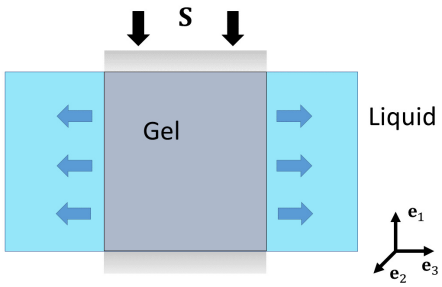

Figure 4.7: A schematic of the axisymmetric problem. The top and bottom plates are impermeable. The cylindrical gel is in contact with fluid along the circumference. Flow is in the radial direction when the gel is compressed.

.

Here we assume that $q(z,t) \ll 1$ and $R\frac{\partial q(z,t)}{\partial z} \ll 1$, i.e. the fluid flux in the radial direction is primarily induced by the radial pressure gradient. Consequently, the solid volume fraction ϕ and the fiber network stretch λ are approximated as being independent of r. By this assumption, only the pressure part in the chemical potential (second term in eqn.(4.9)) depends on r. In order to capture the interface propagation in z direction and further simplify the problem, we integrate eqn.(4.6) over the r direction and average over the cross

sectional area in the reference configuration. This gives

$$\langle \dot{c}_{\mathrm{R}} \rangle = \frac{\partial}{\partial z} \langle m(\phi) \frac{\partial}{\partial z} \mu(\phi) \rangle + \frac{2}{R} j_r \Big|_{r=R}. \tag{4.25}$$

Here, $\langle f \rangle = \frac{1}{\pi R^2} \int_0^R f(r) 2\pi r \mathrm{d}r$ for any function $f(r, z, t)$. The two terms on the right hand side denote the liquid flux in the z and r direction, respectively. Given the assumption for the displacement field in eqn.(4.24), we notice that the solid volume fraction ϕ in the deformed configuration is independent of r. Moreover, by eqn.(4.9) the chemical potential μ is linear in P, and thus the z-flux depends on ϕ and the averaged pressure $\langle P \rangle$. Therefore, the above equation can be written as

$$\frac{\partial}{\partial t} \frac{\partial}{\partial z} g(z,t) = \frac{\partial}{\partial z} m(\phi) \frac{\partial}{\partial z} \mu(\phi, \langle P \rangle) + \frac{2vm(\phi)}{R} \phi \frac{\partial P}{\partial r} \Big|_{r=R}. \tag{4.26}$$

To solve displacement controlled problems, i.e. given boundary conditions

$$\begin{aligned} g(z,t) = 0, \quad q(z,t) = 0 \quad & \text{at } z = 0, \\ g(z,t) = H_0 - Vt, \quad q(z,t) = 0 \quad & \text{at } z = H_0, \\ \mu = \mu_0, \quad T_{rz} = T_{r\theta} = 0 \quad & \text{at } r = R, \end{aligned}$$

we integrate eqn.(4.26) along z-direction from bottom to any arbitrary height h

$$\frac{\partial}{\partial t} g(h,t) = m(\phi) \frac{\partial}{\partial z} \mu(\phi, \langle P \rangle) \Big|_{z=h} + \frac{2v}{R} \int_0^h \phi \frac{\partial P}{\partial r} \mathrm{d}z. \tag{4.27}$$

Eqn.(4.27) is a second order differential-integral equation and can be solved numerically by the finite difference method, with the averaged pressure $\langle P \rangle$ and the pressure gradient at the boundary $r = R$ as yet unknown. To specify the pressure distribution along z-axis, we consider the balance of force equations:

$$(\frac{\partial}{\partial r} + \frac{1}{r}) \left(\frac{f'(\lambda)}{3\lambda} (1+q) - \frac{P}{1+q} \right) + \frac{\partial}{\partial z} \left(\frac{f'(\lambda)}{3\lambda} r \frac{\partial q}{\partial z} \right) = 0, \tag{4.28}$$

$$(\frac{\partial}{\partial r}+\frac{1}{r})\left(\frac{\partial q}{\partial z}(\frac{\partial g}{\partial z})^{-1}\frac{rP}{1+q}\right)+\frac{\partial}{\partial z}\left(\frac{f'(\lambda)}{3\lambda}\frac{\partial g}{\partial z}-\langle P\rangle(\frac{\partial g}{\partial z})^{-1}\right)=0. \tag{4.29}$$

These are components of the conservation of momentum eqn.(4.7) in cylindrical coordinates in the r- and z- directions, respectively. By neglecting the higher order terms and averaging over r-direction, the balance of force in z eqn.(4.29) gives

$$\frac{f'(\lambda)}{3\lambda}\frac{\partial g}{\partial z}-\langle P\rangle(\frac{\partial g}{\partial z})^{-1}=S, \tag{4.30}$$

where S is the applied loading force and is yet undetermined in a velocity controlled problem. Interestingly, eqn.(4.30) is the same as eqn.(4.7) except that P is replaced by $\langle P\rangle$, which will help eliminate the $\langle P\rangle$ in eqn.(4.27). Up to this point, the second term in eqn.(4.27) is still undetermined. In this framework, however, we cannot solve for the pressure distribution. Therefore, we find an approximation of the pressure gradient at the sides as follows. By dimensional analysis,

$$\left.\frac{\partial P}{\partial r}\right|_{r=R}\propto\frac{\langle P\rangle-P_0}{R},$$

while P_0 is the pressure at boundary such that $\mu=\mu_0$. Here we choose the coefficient to be 4, i.e.

$$\left.\frac{\partial P}{\partial r}\right|_{r=R}=-4\frac{\langle P\rangle-P_0}{R}. \tag{4.31}$$

This is equivalent to assuming a quadratic pressure distribution in r-direction. A quadratic pressure distribution has also been observed in other work [132]. Therefore, eqn.(4.27) can be rewritten as

$$\frac{\partial}{\partial t}g(h,t)=m(\phi)\left.\frac{\partial}{\partial z}\mu(\phi,S)\right|_{z=h}-\frac{8v}{R^2}\int_0^h(\mu-\mu_0)\mathrm{d}z. \tag{4.32}$$

$$\frac{VR^2}{8v}=\int_0^{H_0}(\mu-\mu_0)\mathrm{d}z, \tag{4.33}$$

which is again a natural result of the incompresibility of the liquid and the fiber network. Eqn.(4.33) and eqn.(4.32) can be solved for the z-displacement $g(z,t)$ and the applied force $S(t)$. The r-displacement is solved from eqn.(4.28) by averaging over the r-direction.

To solve eqn.(4.32) numerically, we use a forward time central space finite difference scheme. Consider a one-dimensional grid with $N+1$ points spaced uniformly by ΔX. Let g_i^k denote the displacement at node i in time step k, while $z_0 = 0$ and $z_N = H_0$ corresponds to $i = 0$ and $i = N$, respectively. The displacement boundary conditions can be written as

$$\begin{aligned} g_0^k &= 0, \\ g_N^k &= H_0 - Vk\Delta t. \end{aligned} \tag{4.34}$$

The time and spatial derivatives of g for interior points are approximated by the following finite difference equations:

$$\left(\frac{\partial g}{\partial t}\right)_i^k \approx \frac{g_i^{k+1} - g_i^k}{\Delta t} \tag{4.35}$$

$$\left(\frac{\partial g}{\partial z}\right)_i^k \approx \frac{g_{i+1}^k - g_{i-1}^k}{2\Delta X} \tag{4.36}$$

$$\left(\frac{\partial^2 g}{\partial z^2}\right)_i^k \approx \frac{g_{i+1}^k - 2g_i^k + g_{i-1}^k}{\Delta X^2}. \tag{4.37}$$

The solid volume fraction $\phi = (\frac{\partial g}{\partial z})^{-1}$ and the fiber network stretch $\lambda = \sqrt{\frac{\phi^{-2}+2}{3}}$ follow naturally. For the current time step, the applied stress S is a known constant, and thus the derivative of chemical potential can be found by chain rule as

$$\left(\frac{\partial \mu}{\partial z}\right)_i^k = \left(\frac{\partial \mu}{\partial \phi}\frac{\partial \phi}{\partial z}\right)_i^k = \left(-\frac{\partial \mu}{\partial \phi}\phi^2\right)_i^k \left(\frac{\partial^2 g}{\partial z^2}\right)_i^k.$$

We use the trapezoidal rule to approximate the integral term

$$\left(\int_0^{z_i} (\mu - \mu_0)\mathrm{d}z\right)_i^k \approx \sum_{n=0}^{i} \Delta X(\mu_n^k - \mu_0) - \frac{1}{2}\Delta X(\mu_0^k + \mu_i^k). \tag{4.38}$$

With the above approximations, the displacement at the k+1-th step, given the displacement field g and the applied stress S at the k-th step, is given by

$$g_i^{k+1} = g_i^k + \Delta t \left(m(\phi)\frac{\partial}{\partial z}\mu(\phi, S)\right)_i^k - \Delta t \frac{8v}{R^2}\left(\sum_{n=0}^{i} \Delta X(\mu_n^k - \mu_0) - \frac{1}{2}\Delta X(\mu_0^k + \mu_i^k)\right). \tag{4.39}$$

After the displacement field is obtained, the applied stress S can be found from the compatibility condition eqn.(4.33).

We conduct compression and decompression at rates of $\dot{\gamma} = 0.05\text{s}^{-1}$ and $\dot{\gamma} = 0.005\text{s}^{-1}$. Similar to the 1D case, decompression is an immediate pulling after compression without equilibration. Hysteresis can be observed in the compressive stress vs. strain profiles in Fig. 4.8 due to fluid flow and a dissipative phase transition. For comparison, we re-plot experimental data on fibrin gels from Kim *et al.*[57] and Liang *et al.* [52] in Fig. 4.8. The data from compression experiments of Kim *et al.* at strain rate 0.05 s^{-1} are shown in Fig. 4.8(c). The loading curve of Fig. 4.8(a) looks qualitatively similar to that in Fig. 4.8(c) and the range of stress is also similar. Liang *et al.* peformed compression and decompression experiments at strain rate 0.00025 s^{-1} and their data appears in Fig. 4.8(d). The dip at the beginning of unloading, the tensile stress in the lower plateau, and the overall hysteresis are the features shared by curves in (b) and (d), although the upper plateau in (b) is much flatter thant that in (d).

For both the rates we notice an interface propagating from the moving plate towards the fixed plate as shown in Fig. 4.9(a) and (b). For comparison, we re-plot experimental data on interface propagation from Kim *et al.*[57] and Liang *et al.*[52] in Fig. 4.9(c) and (d). In both these papers the authors had fluorescently labeled the fibrin fibers; this allowed them to distinguish the densified phase from the rarefied phase of the network simply by identifying the regions of high and low fluorescence intensity. For the low strain rate (about 0.00025 s^{-1}) experiments a fluorescence intensity profile in Figure 2D of Liang *et al.* is re-plotted as a fucntion of position in Fig. 4.9(c). The sharp phase boundary seen in (a) and the relatively flatter strain profiles ahead and behind it are similar to the sharp phase boundary seen in (c). For the high strain rate (about 0.05 s^{-1}) experiments the fluorescence intensity profile of Figure 3a of Kim *et al.* is re-plotted as function of reference position in Fig. 4.9(d). A less sharp (or more diffuse) interface between the densified and rarefied phases is apparent in this figure which is somewhat similar to that in (b).

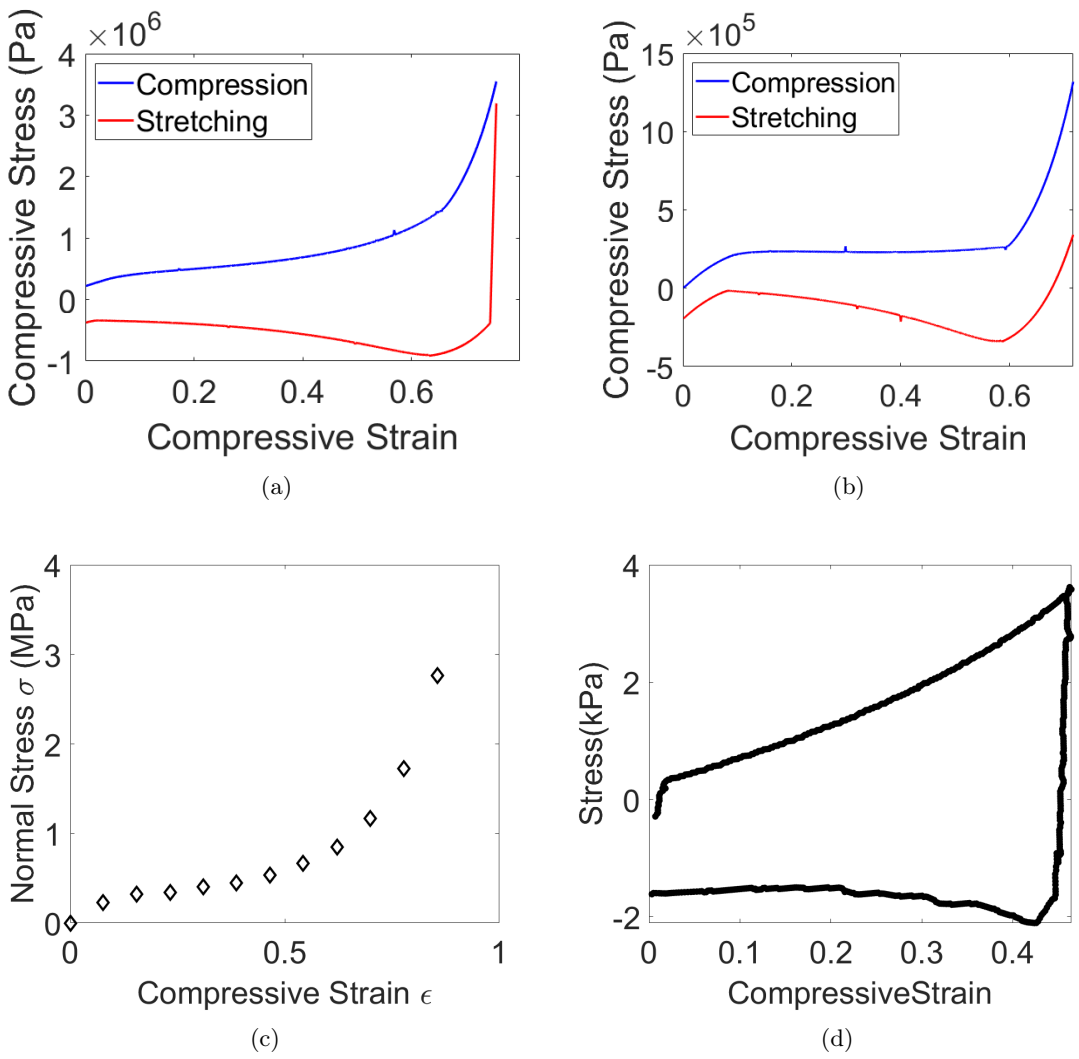

Figure 4.8: Compressive stress vs. strain plots for (a) $\dot{\gamma} = 0.05$ s^{-1} and (b) $\dot{\gamma} = 0.005$ s^{-1} for the axisymmetric problem depicted in Fig. 4.7. Hysteresis is observed at both high rate and low rate. Notice the peculiar drop in compressive stress just when decompression starts. This feature is absent in the purely one-dimensional model, but it is present in experiments depicted in section 5 of this paper. (c) Experimental data on compression of fibrin gels from Figure 5 of Kim *et al.* [57] (black diamonds) are replotted for comparison with the loading curve in (a). The strain rate in experiments of Kim *et al.* was approxmately 0.05 s^{-1}. The scale of stresses and the shape of the loading curve are similar in (a) and (c). (d) Experimental data points on the compression and decompression of plasma clots from Figure 6 (black points) of Liang *et al.*[52] are replotted for comparison with (b). The strain rate in the experiment of Liang *et al.* was approximately 0.00025 s^{-1}, much lower than that in (b). The dip at the beginning of unloading and the tensile stresses in the lower plateau are common features of (b) and (d).

.

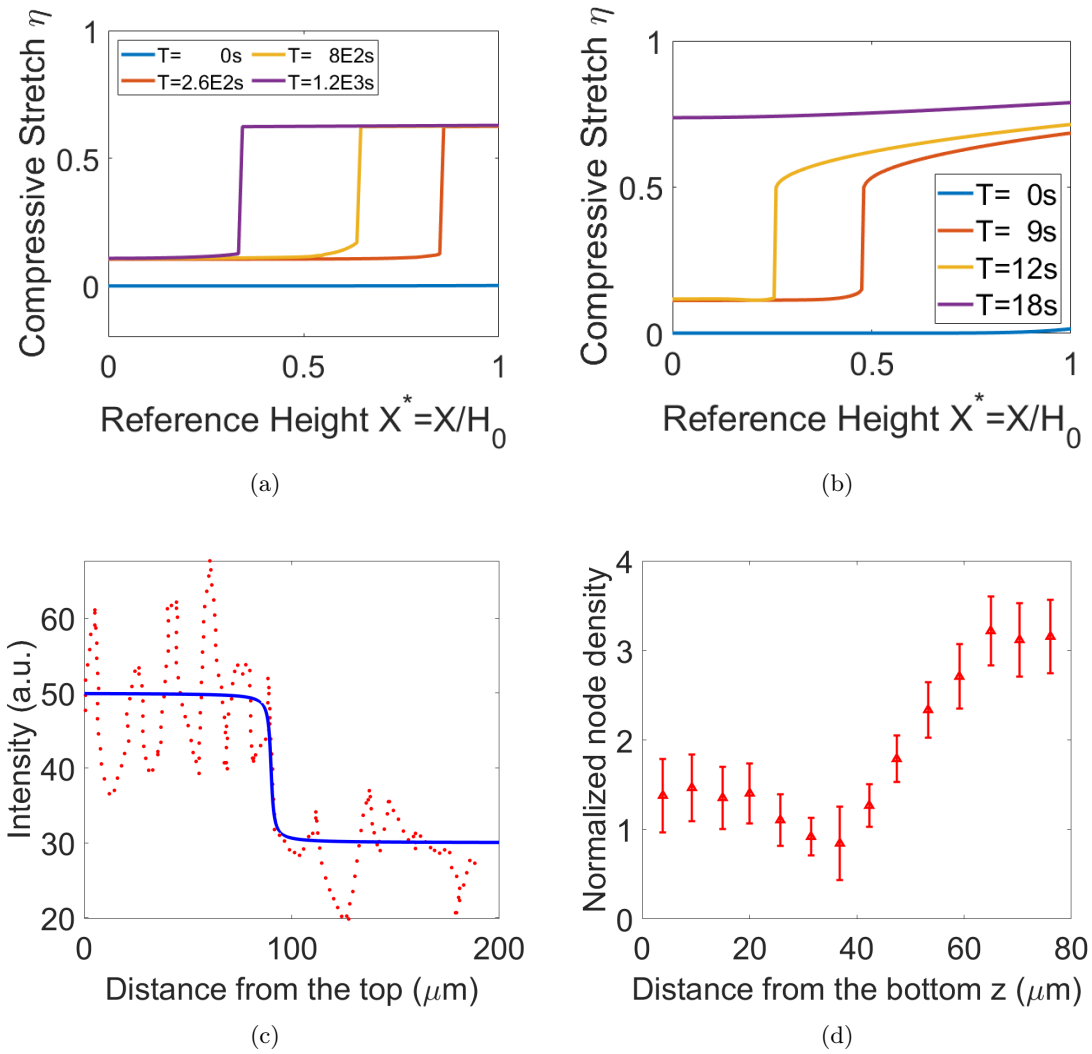

Figure 4.9: Stretch profile for the compression process at a rate of (a) $\dot{\gamma} = 0.005$ s^{-1} and (b) $\dot{\gamma} = 0.05$ s^{-1}. A propagating interface appears at the moving end and goes towards the fixed end. (c) Experimental data showing a moving interface in compressed plasma clot from Figure 2D of Liang *et al.* [52] (red dots) are re-plotted for comparison with the stretch profile in (a). A sharp phase boundary and flat strain profiles ahead and behind it are observed similar to (a) at low strain rate. (d) Experimental data showing a moving interface in compressed fibrin gel from Figure 3a (red triangles) of Kim *et al.*[57] are re-plotted for comparison with (b). At high rate (about 0.05 s^{-1}) a more diffuse interface between the densified and rarefied phases appears.

.

In the compression process, three regions can be observed in the stress-strain curve: (1) a linearly increasing stress where the gel is in rarefied phase, (2) an intermediate region where the gel undergoes phase transition, and (3) a steeply increasing region where the

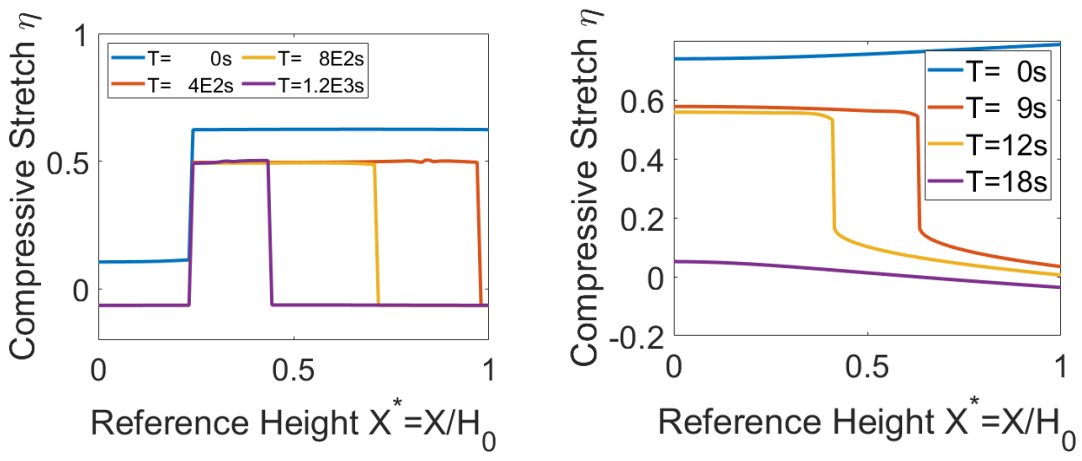

(a) (b)

Figure 4.10: Stretch profile for the decompression process at a rate of (a) $\dot{\gamma} = 0.005$ s^{-1} and (b) $\dot{\gamma} = 0.05s^{-1}$. A propagating interface appears at the moving plate seperating the densified phase and the rarified phase. A diffusive strain distribution is found in the densified phase.

.

gel is entirely in the densified phase. The decompression is conducted after the interface reaches the fixed plate and the material is entirely in densified phase. The decompression curve is different from the compression. We notice a dramatic increase in the tensile stress followed by a flat decrease. The tip of the decompression curve denotes the position at which the interface appears at the moving top plate and moves towards the bottom plate. The propagating interface during the decompression process can be seen in Fig. 4.10. The strain profiles and hysteresis loops for the axisymmetric problem share some (but not all) features with those of the one-dimensional problem. In particular, there is a big dip in the compressive stress just when decompression starts in the axisymmetric problem that is absent in the one dimensional problem.

4.5. Stress-strain response of blood clots during compression decompression cycles

Liang *et al.* [52] document the stress-strain curves for low strain-rate cyclic compression/decompression of blood clots. The hysteretic stress-strain curves computed in sections 3 and 4 above have been experimentally demostrated in Liang *et al.* where the flat plateau

during interface propagation is shown. They also confirm the existence of a sharp interface between rarefied and densified phases of the fibrin network via confocal microscopy for low-strain rate compression as shown in Fig. 4.9(c). More diffuse interaces for high strain rate compression can be found in Kim *et al.* [57] and Liang *et al.* [52] and this is consistent with stretch profiles in Fig. 4.9. Here we report a limited set of experiments on cyclic compression/decompression of fibriin gels with the objective of verifying some features observed in the stress-strain curves that are peculiar to higher strain-rates and are not easily seen at lower rates.

Whole blood from healthy volunteers was collected with informed consent into 12 mM sodium citrate ($Na_3C_6H_5O_7$) added to prevent coagulation, and from this blood platelet-poor plasma (PPP) and platelet-rich plasma (PRP) were obtained. Clots 600μm thick were formed at 37°C directly between rheometer plates (ARG2; TA Instruments, New Castle, DE) by adding $CaCl_2$ (25mM final concentration) and human α-thrombin (1U/mL final).

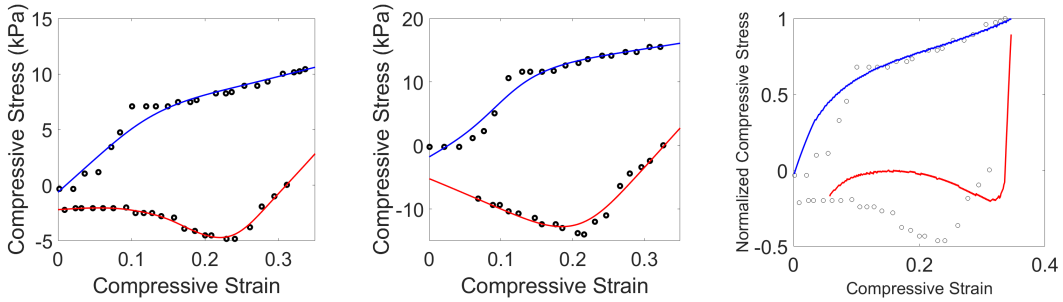

Figure 4.11: High rate cyclical loading for (a) PPP clots and (b) PRP clots. The peculiar stress drop in the unloading plateau and the upward sloping loading plateau are seen in numerical simulations of the axisymmetric problem. The blue (compression) and red (decompression) lines are guides to the eye. They are not the results of numerical calculation. (c) Normalized compressive stress plotted as function of compressive strain from both experiment and computation. The qualitative features in the experimental data are captured by the computations.

.

Compression and decompression were performed continuously at the rates of 100μm/min, as the upper rheometer plate moved down and went back to the same position to exert an

axial force on the upper surface of the clot. Three cycles of compression and decompression were performed on a clot. The clots were compressed and decompressed vertically up to $\frac{1}{2}$ or $\frac{3}{4}$ of their initial thickness. A compressive strain (degree of compression) was defined as the absolute fractional changes in fibrin clot thickness, $\eta = |\frac{\Delta H}{H_0}|$, where $\Delta H = H - H_0$, and H_0 and H are the initial and reduced thickness dimensions of the uncompressed and compressed clots, respectively. During compression and decompression a normal stress was measured and stress-strain curves were plotted for further analysis as shown in Fig. 4.11 for both PPP and PRP clots. Notice the upward sloping plateau during compression as in Fig. 4.8(b). The peculiar drop in stress near the start of the decompression seen in Fig. 4.8(b) can be seen clearly in panels (a) and (b) of Fig. 4.11. In the lower plateau (during decompression) the stresses are tensile in the experiment just as in our numerical computations in Fig. 4.8. To show that our computations are predictive we have plotted stress-strain curve with stresses normalized by the corresponding maximum from our computations and experiments together in Fig. 4.11(c). The strain rate in the numerical calculation is $\dot{\gamma} = 0.02\ \mathrm{s}^{-1}$. In this case, the decompression starts before the phase transition finishes. We do not expect an exact match between experiment and computations, but it is clear that the qualitative characteristics of the experimental loading/unloading curve are captured by the computational loading/unloading curve. These experiments and those documented in Liang *et al.* [52] show that a chemoelastic model with a double-well stored energy function for the solid network is appropriate to study the mechanical behavior of blood clots.

4.6. Conclusion

We have shown in this paper that fibrous gels, such as blood clots (or fibrin gels), can be treated using a chemo-elastic continuum model. We depart from well-established chemo-elastic models for gels (that use neo-Hookean constitutive laws for the polymer) by using a double-well energy landscape for the underlying solid network. One of the wells represents the low-strain rarefied phase of the fibrous network and the other well represents the high-strain densified phase. Under compressive loads the fibers can buckle and the network converts from a rarefied phase to a densified phase accompanied by a dramatic reduction

of volume and release of fluid. A host of features in the experimentally observed stress-strain behavior of fibrous gels under compression can be captured by our chemo-mechanical model including (a) formation and propagation of an interface separating rarefied and densified phases of the network, (b) rate-dependent sharpness of the propagating interface (c) rate-dependent hysteresis, and (d) rate-dependent features in the plateaus of the stress-strain curves observed during loading and unloading. Some of these features have also been captured in an earlier continuum model of these gels which was based on the Abeyaratne-Knowles theory of phase transitions[52]. That model required the specification of a *kinetic law* for interface propagation in addition to the stress-strain relations of the rarefied and densified phases of the network. The chemo-mechanical model described here does not require the specification of a kinetic law since the motion of the interface is controlled by the flow of the fluid trapped in the gel. Similar models may be applied to other tissues that also have a fibrous structure.

A feature of the work described above is that finite element calculations were not required to obtain experimentally relevant results, unlike prior work on compression of gels [47, 133]. This was accomplished by considering specific problems that could be reduced to one dimension or had axial symmetry. Finite difference techniques were used to solve the resulting partial differential equations and this gave results that were in qualitative agreement with experiments. In doing so we have gone beyond analytically solvable problems that require assumptions of small strains [132], but have stopped short of writing a fully three dimensional continuum theory for the compression of fibrous gels. A fully three dimensional continuum calculation can be done using finite elements, but not without significant effort in developing appropriate elements to handle poro-elasticity with large deformations and phase transitions.

CHAPTER 5

Rheology of Fibrous Gels under Compression

This chapter is based on work published in [134].

5.1. Introduction

Fibrous gels are substances that consist of a network of fibers infused with fluid [130, 135]. A number of biological materials such as fibrin [57], collagen [120], gelatin [136] and agarose [137] that form filamentous networks belong to this class of gels. The solid network that endows these gels with structural integrity is formed by the polymerization of proteins or polysaccharides, but it is different from the polymer network of synthetic elastomeric gels. The fibers in the fibrous gels behave like struts of a foam – for low applied stresses they appear relatively straight like rods under a confocal microscope, but they buckle under large compressive stress [57, 137, 138]. No such buckling is known to happen in elastomeric gels, which behave like rubbers or neo-Hookean polymers in their dry state [122]. Fibrous gels have recently been modeled using a continuum theory of gels under the assumption that the stored energy function of the underlying solid is multi-welled [118]. Such multi-well stored energy functions are characteristic of materials that undergo phase transitions [17, 139, 140]. In the case of fibrous gels one well in the stored energy function corresponds to the rarefied phase with straight fibers while the other well corresponds to the densified phase with buckled fibers [123]. The compressive stress-strain relations of the two phases are different [52, 57]. The fluid flow behavior in the two phases is also different; the pore-size of the polymer network is much smaller in the densified phase than that in the rarefied phase. Thus, fluid motion through the gel is more hindered in the densified phase than the rarefied phase.

Rheometry is a commonly used method to measure the mechanical properties of soft materials like gels [141, 142]. It is particularly suited to the measurement of properties of biological gels because they can be polymerized between the rheometer plates. As such,

storage and loss moduli of a number of biological gels have been measured and there is a rich literature on the variation of these moduli as a function of material parameters such as mesh size, cross-linking, etc [58–60]. In the case of fibrin gels, which are of interest to us, the storage and loss moduli (in oscillatory shear) have been measured as a function of applied compressive strain [57], compressive stress [143], and shear stress [144]. It has been shown that the storage and loss moduli decrease initially as function of applied compressive strain, then they stay on a long plateau, and then finally increase steeply as the compressive strain increases. Similar trends in the storage and loss moduli as a function of compressive strain were demonstrated for agarose gels [137] although the regime of steep increase was not reached in these experiments. This trend has been explained using a model of phase transitions mentioned above [57]. Initially, at low applied strains the fiber network is in the rarefied phase with fibers mostly straight and deformation accomodated mostly by fiber rotation; at a critical strain the fibers buckle creating an interface that separates the gel into two compartments, one in which the fibers are straight and another in which the fibers are buckled. Such an interface has been observed in both fibrin gels [52] and collagen gels [120]. A re-plot of Fig. 3a of [57] showing the interface in a compressed fibrin gel appears in Fig. 5.1(a). This interface, or phase transition front separating the rarefied and densified phases, propagates through the thickness of the sample as more compressive strain is applied [52, 118]. Multiple local buckling events that lead to formation of multiple bands is also possible and this has been demonstrated in experiments and simulations of fiber networks in [145, 146]. Note, however, that these latter experiments and simulations did not have any liquid infusing the fiber networks. From a different perspective, multiple local buckling events would be similar to a phase transition proceeding by many nucleation events, where as in our fibrin gels the phase transition proceeds by the motion of an interface after a single nucleation event near the moving plate. Eventually, the interface reaches the other end converting the entire network into a densified state. As a result, the compressive stress-strain curve has three regions – a short linear region near zero strain, a long plateau region corresponding to the propagation of the phase transition front, and a region with stress

increasing steeply with strain near compressive strain of 1. These three regions correspond closely with the three regions seen in the plots of the storage and loss moduli as a function of strain [57]. In particular, the storage modulus in the plateau region is low because the gel accomodates deformation by moving the interface, which is an extra degree of freedom that is not available to it when the network is purely in the rarefied or densified phases. The moduli in the densified phase are high because the stress-strain curve is steep and the fluid motion through small pores is difficult, while the moduli in the rarefied phase are low because the fibers can rotate and fluid motion through large pores is easy. Importantly, the models in [57, 118] ignore the evolution of micro-structure of the filament network in response to cyclic compression. There is damage and re-arrangement of fibers in the cyclic compression of fibrin gels. In fact, Liang *et al.*, [52] have shown in their Figure 1 (see also their figures 5 and 6) that the first cycle of compression and decompression has larger hysteresis than all subsequent cycles. The stress-strain curves in compression/decompression sit on top of each other in the second, third and subsequent cycles. Our model does not take account of damage, so it applies to the second and subsequent cycles of loading/unloading. We do not have direct experimental evidence like the above for other fibrous gels (such as collagen gels), but damage has been observed in carbon-nanotube foams [123] subject to cyclic compression.

A curious observation in fibrin gels is that the storage and loss moduli depend on whether a particular state of overall compressive strain has been reached during loading or during unloading the sample. This observation is documented in Liang *et al.* [52] (a re-plot of Figure 8 of [52] can be seen in Fig. 5.1(b)), but it remains a conundrum that has not been resolved. Our goal in this paper is to explain trends in the storage modulus as a function of applied compressive strain and a possible origin of the differences between loading and unloading. We build upon a model of phase transforming gels that has been published previously in Sun *et al* [118].

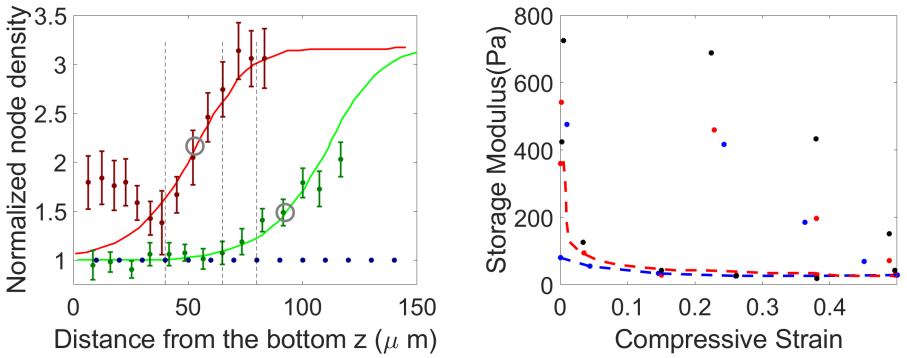

(a) (b)

Figure 5.1: (a) The node density as a function of height from the bottom of a compressed clot at two different overall strains re-plotted (as red and green points with error bars) from Figure 3a of [57]. The node density is low near the bottom plate (corresponding to rarefied network) and high near the top plate (corresponding to the densified network). A propagating interface (red and green curves) separates these two regions. (b) The storage modulus during loading and unloading over three cycles of compressing and decompressing a fibrin gel re-plotted from Figure 8 of [52]. The storage modulus is higher during unloading than during loading at the same overall strain. The dashed lines are fits given in [52] based on a rudimentary visco-elastic model.

.

5.2. Theoretical Framework

We seek to find the storage modulus and loss modulus of a gel as a function of applied normal strain. First, the gel is compressed to a (possibly large) compressive strain, and then infinitesimal oscillations in the same direction as the normal strains are applied to deduce the storage and loss modulus. Our framework to compute the storage and loss moduli is based on the derivations in the Sun *et al.* [118] for a three-dimensional axially symmetric gel confined between two plates (as in a parallel plate rheometer) as shown in Fig. 5.2. This framework follows earlier work by Chester and Anand [47] as well as Hong *et al.* [50].

For the convenience of readers, we will repeat some of the key steps in Sun *et al.*[118]. Consider a dry fibrous network $\mathcal{B}$ occupying a reference volume Ω, and let $\mathbf{X}$ denote a material point. The deformation of the network is characterized by $\mathbf{x} = \mathcal{X}(\mathbf{X}, t)$, the motion of the body, and $c_{\mathrm{R}}(\mathbf{X}, t)$, the number of fluid molecules per unit reference volume. Suppose the fibrous network and the fluid are both incompressible, then the conservation laws of

mass and momentum require that

$$\det \mathbf{F} = 1 + v c_{\mathrm{R}}, \tag{5.1}$$

$$\dot{c}_{\mathrm{R}} = \mathrm{Div}(m \nabla \mu), \tag{5.2}$$

$$\mathrm{Div}\ \mathbf{T}_{\mathrm{R}} + \mathbf{b}_{\mathrm{R}} = \mathbf{0}. \tag{5.3}$$

Here $\mathbf{F} = \nabla \mathcal{X}$ is the deformation gradient, v is the volume of one fluid molecule, where we choose $v = 1.7 \times 10^{-28}$ m^3 for water; μ is the chemical potential; $\mathbf{T}_{\mathrm{R}}$ is the first Piola-Kirchhoff stress and $\mathbf{b_R}$ is a body force. In this work the body force is assumed to be 0. Here m is the mobility of the fluid, which depends on the fluid concentration c_{R} (which is directly connected to the pore-size of the network). For simplicity we assume $m = \frac{D c_{\mathrm{R}}}{k_B T}$ where $D = 5.0 \times 10^{-9} \mathrm{m}^2/\mathrm{s}$ is a diffusion coefficient and k_B is the Boltzmann constant and $T = 300\mathrm{K}$ is the absolute temperature. The P-K stress $\mathbf{T}_{\mathrm{R}}$ in eqn.(5.3) and the chemical potential μ in eqn.(5.2) are constitutively given by a free energy density function $\psi_{\mathrm{R}}(\mathbf{C}^e, c_{\mathrm{R}})$ through

$$\mathbf{T}_{\mathrm{R}} = 2\mathbf{F}^e \frac{\partial \psi_{\mathrm{R}}(\mathbf{C}^e, c_{\mathrm{R}})}{\partial \mathbf{C}^e} \mathbf{F}^{s-T} - P\mathbf{F}^{-T}, \tag{5.4}$$

$$\mu = \frac{\partial \psi_{\mathrm{R}}(\mathbf{C}^e, c_{\mathrm{R}})}{\partial c_{\mathrm{R}}} + \bar{p} v. \tag{5.5}$$

Here $\bar{p} := -\frac{1}{3} \det \mathbf{F}^e \mathrm{tr} \mathbf{T}$ defines a mean normal pressure. $\mathbf{T} = (\det \mathbf{F})^{-1} \mathbf{T}_{\mathrm{R}} \mathbf{F}^T$ is the Cauchy stress tensor. Due to the incompressibility constraint eqn.(5.1), we introduce a Lagrange multiplier P, which will be determined by the solution to the mechanical boundary value problem.

The free energy function $\psi_{\mathrm{R}}(\mathbf{C}^e, c_{\mathrm{R}})$ is assumed to have the decomposition

$$\psi_{\mathrm{R}}(\mathbf{C}^e, c_{\mathrm{R}}) = \mu^0 c_{\mathrm{R}} + \psi_{\mathrm{R,mixing}}(c_{\mathrm{R}}) + \psi_{\mathrm{R,mechanical}}(\mathbf{C}^e, c_{\mathrm{R}}), \tag{5.6}$$

with

$$\psi_{\mathrm{R,mixing}} = \frac{k_B T}{v}\frac{1}{\phi}\left((1-\phi)\ln(1-\phi) + \chi\phi(1-\phi)\right), \tag{5.7}$$

$$\psi_{\mathrm{R,mechanical}}(\mathbf{C}^e, c_{\mathrm{R}}) = f_4(\lambda) - G_0 \ln\det\mathbf{F}, \tag{5.8}$$

denoting the contribution to the free energy function from mixing of fluid and solid, and the deformation of the network, respectively. Here $\phi := (1 + vc_{\mathrm{R}})^{-1}$ is the solid volume fraction, χ is a material parameter, which takes value 0.1 here for a high degree of swelling, and $\lambda := \frac{1}{\sqrt{3}}\sqrt{\mathrm{tr}\mathbf{C}} = \frac{1}{\sqrt{3}}(1 + vc_{\mathrm{R}})^{1/3}\sqrt{\mathrm{tr}\mathbf{C}^e}$ is the stretch of the fiber network. f_4 is a quartic function in λ and $G_0 = 0.1$MPa is a constant. In Sun *et al.*[118] it has been shown that a quartic f_4 can capture propagating phase transition fronts during compression-decompression cycles of fibrous gels. The phase transition front separates a densified phase (with buckled and bent fibers) of the fibrous gel from a rarefied phase (with straight fibers). Combining eqns. (5.5), (5.7) and (5.8) gives

$$\mu = \mu^0 + k_B T(\ln(1-\phi) + \phi + \chi\phi^2) - vG_0\phi + vP\phi. \tag{5.9}$$

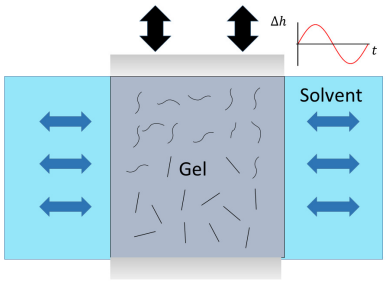

Figure 5.2: A schematic of the axisymmetric problem of the compression of a fibrous gel. The top and bottom plates are impermeable. The cylindrical gel is in contact with fluid along the circumference. The top plate is oscillating sinusoidally at small amplitude around an overall large compressive strain while the response force is recorded.

.

Next, we consider the 3D oscillatory compression problem. We assume that a cylinder of fully swollen gel of radius R and height H_0 is placed between two impermeable parallel plates

immersed in fluid. At the top and bottom boundaries, the gel is attached to the wall such that only displacement in the axial direction $\mathbf{e}_1 = \mathbf{e}_z$ is possible. In cylindrical coordinates (r, θ, z), we assume the motion of the body takes the following form:

$$x_z = g(z,t); \quad x_\theta = 0; \quad x_r = r(1 + q(z,t)). \tag{5.10}$$

In the above, $q(z,t)$ captures the Poisson effect. If the gel is not attached to the top and bottom walls then $q(z,t)$ will be independent of z. An analysis of Poisson ratio is beyond the scope of this paper, but experimental measurements of Poisson ratio at small strains for agarose gels were made in [137] and theoretical analysis of the Poisson ratio in fiber networks can be found in [147]. We assume further that the fluid flux in the radial direction is primarily induced by the radial pressure gradient. Note that the solid volume fraction ϕ in the deformed configuration is independent of r under this assumption. Then, we average the fluid conservation equation eqn.(5.2) over the cross-section area and combine it with the solid conservation equation eqn.(5.1) to get

$$\frac{\partial}{\partial t}\frac{\partial}{\partial z}g(z,t) = \frac{\partial}{\partial z}m(\phi)\frac{\partial}{\partial z}\mu(\phi, \langle P \rangle) + \frac{2vm(\phi)}{R}\phi\left.\frac{\partial P}{\partial r}\right|_{r=R}. \tag{5.11}$$

The boundary value problem to be solved is

$$\begin{aligned} g(z,t) = 0, \quad q(z,t) = 0 \quad &\text{at } z = 0, \\ g(z,t) = H - H_0\epsilon(t), \quad q(z,t) = 0 \quad &\text{at } z = H_0, \\ \mu = \mu_0, \quad T_{rz} = T_{r\theta} = 0 \quad &\text{at } r = R, \end{aligned}$$

where $\epsilon(t) = \epsilon_0 \sin(\omega t)$ is a sinusoidal oscillation with amplitude ϵ_0 and frequency $\omega/(2\pi)$. To specify the last term in eqn.(5.11), we assume a quadratic pressure distribution in r-direction [132], in which case

$$\left.\frac{\partial P}{\partial r}\right|_{r=R} = -4\frac{\langle P \rangle - P_0}{R}. \tag{5.12}$$

We combine a quadratic pressure distribution eqn.(5.12) with eqn.(5.11) and integrate eqn.(5.11) along the z-direction from bottom to any arbitrary height h

$$\frac{\partial}{\partial t}g(h,t) = m(\phi)\frac{\partial}{\partial z}\mu(\phi,S)\bigg|_{z=h} - \frac{8}{R^2}\int_0^h m(\phi)(\mu-\mu_0)\mathrm{d}z, \tag{5.13}$$

where S is the applied stress and is yet unknown in a velocity controlled problem. By neglecting the higher order terms and averaging over r-direction, the balance of force in z gives

$$\frac{f'(\lambda)}{3\lambda}\frac{\partial g}{\partial z} - \langle P\rangle(\frac{\partial g}{\partial z})^{-1} = S. \tag{5.14}$$

Next, we combine eqn.(5.14) with averaged eqn.(5.9) to eliminate the $\langle P\rangle$ term

$$\mu = \mu^0 + k_BT(\ln(1-\phi)+\phi+\chi\phi^2) - vG_0\phi + v\frac{f'(\lambda)}{3\lambda}\phi^{-1} - vS = \mu^0 + \hat{\mu}(\phi) - vS. \tag{5.15}$$

Note that by doing this, the deformation effect ϕ and the stress effect S are decoupled in the expression of μ, given by $\hat{\mu}(\phi)$ and $-vS$, respectively. We choose h to be H_0 in eqn.(5.13) and plug in eqn.(5.15) to get

$$S = \frac{\int_0^{H_0} m(\phi)\hat{\mu}(\phi)\mathrm{d}z}{\int_0^{H_0} m(\phi)\mathrm{d}z} - \frac{R^2}{8\int_0^{H_0} m(\phi)\mathrm{d}z}V(t). \tag{5.16}$$

Up to this point the boundary value problem can be solved numerically by a finite difference method. We have performed this exercise in Sun *et al.*[118] for various values of H and $\epsilon_0 = 0$ after taking $f_4(\lambda) = \frac{d_2}{2}(\lambda-1)^2 + \frac{d_3}{3}(\lambda-1)^3 + \frac{d_4}{4}(\lambda-1)^4$, where d_2, d_3, d_4 are constants. These constants are chosen such that the quartic polynomial free energy function f_4 has two local minima at λ_1 and λ_3 ($\lambda_1 < \lambda_3$). Then we assume $\lambda = \lambda_1$ is the dry state in the densified phase, and $\lambda = \lambda_3$ is the swollen state in the rarified phase. Particularly, we take $d_2 = 6.4\times10^5$ Pa, $d_3 = -1.6\times10^5$ Pa, and $d_4 = 1\times10^4$ Pa. With these parameters we get $\lambda_1 = 1$ and $\lambda_3 = 9$. For convenience the global compressive strain is defined as $\varepsilon = 1 - \frac{H}{H_0}$. We have shown that a phase transition front nucleates at the top plate for large enough values of ε and it moves toward the bottom plate as ε is increased. A snapshot

of the strain profile at steady state for a given ε showing a (sharp) phase transition front appears in Fig. 5.3(a). Experimental evidence for the presence of such a phase transition front in fibrin gels can be found in Liang *et al.* [52]. The inset shows the steady state value of the stress S_0 as a function of given ε. As ε increases from zero S_0 first increases, then it reaches a plateau and stays there over an interval of ε, and then for $\varepsilon > 0.685$, S_0 increases rapidly as ε increases (see inset of Fig. 5.3(a)). This strain is determined by the constants d_2, d_3, d_4 in our double-well strain energy function and the initial solid volume fraction , which is taken to be 0.05 here. The constants d_2, d_3, d_4 will in general be determined by the gel microstructure. In particular, we expect that the compressive strain where the stress-strain curve rises rapidly will be larger when the solid volume fraction is smaller. The plateau region corresponds to the propagation of the phase transition front from the top of the specimen to the bottom during which the stress does not change very much.

What happens when $\epsilon_0 \neq 0$ so that a sinusoidal oscillation is superimposed on an overall compressive strain? In this case we can record the time-dependent stress $S(t) = S_0 + S'(t)$, which contains an oscillation $S'(t)$ around the equilibrium value S_0. The oscillatory part is assumed to take the trigonometric form $S'(t) = E\epsilon \sin(\omega t + \alpha)$, and thus the storage modulus and loss modulus are given by $E' = E\epsilon\cos(\alpha)$, $E'' = E\epsilon\sin(\alpha)$, respectively.

We notice that the time dependent stress response function in eqn.(5.16) is very similar to the stress-strain relation of a Voigt material. Particularly, the first term in eqn.(5.16) represents the elastic effect and the second term represents the viscous effect in the compression. When $V = 0$, we get the equilibrium response $S_0 = \frac{\int_0^{H_0} m(\phi)\hat{\mu}(\phi)\mathrm{d}z}{\int_0^{H_0} m(\phi)\mathrm{d}z}$. On the other hand, the rheological properties can be written as

$$E' = H_0 \frac{\mathrm{d}}{\mathrm{d}h}\left(\frac{\int_0^{H_0} m(\phi)\hat{\mu}(\phi)\mathrm{d}z}{\int_0^{H_0} m(\phi)\mathrm{d}z}\right), \tag{5.17}$$

$$E'' = \frac{R^2 H_0 \omega}{8\int_0^{H_0} m(\phi)\mathrm{d}z}. \tag{5.18}$$

Note that the permeability $m(\phi)$ in the densified phase is smaller than that in the rarified

phase, and thus we should expect the loss modulus to increase as the phase transition progresses because more of the material converts to the densified phase.

5.3. Numerical Method

We follow the numerical method in Sun *et al.* [118] and use a forward time central space finite difference scheme to solve the boundary value problem in the previous section. Particularly, the discretization of eqn.(5.13) is given by

$$g_i^{k+1} = g_i^k + \Delta t \left(m(\phi) \frac{\partial}{\partial z} \mu(\phi, S) \right)_i^k - \Delta t \frac{8v}{R^2} \left(\sum_{n=0}^{i} \Delta X (\mu_n^k - \mu_0) - \frac{1}{2} \Delta X (\mu_0^k + \mu_i^k) \right), \quad (5.19)$$

where g_i^k denotes the displacement at the i-th node at time step k. The corresponding boundary conditions are

$$\begin{aligned} g_0^k &= 0, \\ g_N^k &= H_0 - \epsilon_0 \sin(\omega k \Delta t). \end{aligned} \quad (5.20)$$

First, we load the cylindrical sample to a certain global compressive strain $\varepsilon = 1 - \frac{H}{H_0}$ until it reaches steady state. Recall that H_0 is the reference height of the cylindrical sample and H is the current height. Next, we conduct normal oscillation around this strain value and record the time evolution of the resultant stress obtained by eqn.(5.16) to compute storage and loss moduli later. We repeat this process for various values of strain ε and plot the storage and loss moduli as a function of applied compressive strain. A typical plot of the applied global compressive strain $\varepsilon(t)$ together with the computed stress $S(t)$ appears in Fig. 5.3(b). A phase difference between the two curves is clearly seen; this suggests that our fibrous gel behaves like a visco-elastic material.

To fully characterize the viscoelasticity we provide two methods to obtain the storage and loss moduli. In the first method, we assume the stress is a trigonometric function of time with the same frequency ω as is in the boundary condition, i.e. $S(t) = S_0 \sin(\omega t + \delta)$. By definition, the storage and loss moduli are given by $E' = \frac{S_0}{\epsilon_0} \cos\delta$, $E'' = \frac{S_0}{\epsilon_0} \sin\delta$, respectively.

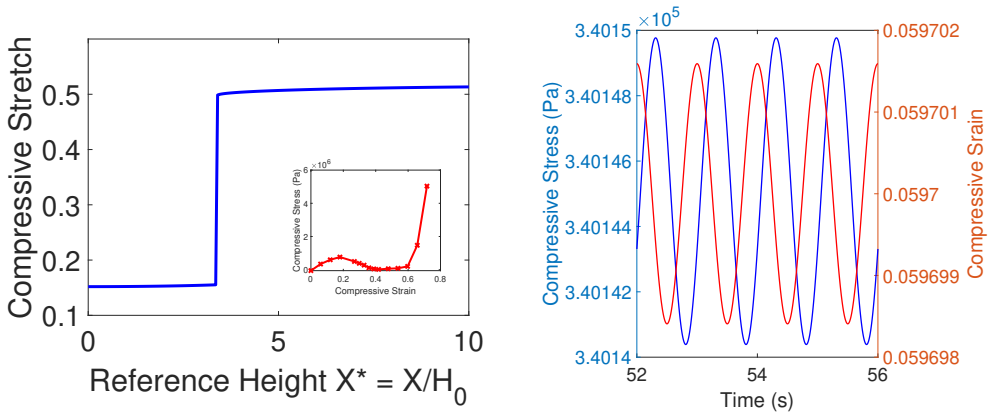

(a) (b)

Figure 5.3: (a) There is a sharp phase transition front separating the rarefied (low strain) on the bottom and the densified (high strain) phase on the top. The phase transition front moves when the top plate moves to change the overall strain. The inset shows the steady state stress S_0 as a function of applied overall strain ε. (b) The input oscillation strain (red) and the stress response (blue) plotted as function of time. Both plots are sinusoidal but a phase difference can be observed due to the dissipation caused by liquid flow.

.

In our numerical calculation, we use an inner product technique – we define the storage and loss basis as $e' = \epsilon_0 \sin(\omega t)$, $e'' = \epsilon_0 \cos(\omega t)$ respectively; then the moduli are given by

$$\begin{aligned} E' &= \frac{\langle S(t), e' \rangle}{\langle e', e' \rangle}, \\ E'' &= \frac{\langle S(t), e'' \rangle}{\langle e'', e'' \rangle}, \end{aligned} \tag{5.21}$$

where $\langle a, b \rangle = \int_{T_s}^{T_s+MT} a(t)b(t)dt$ defines an inner product over M periods of oscillation after the system reaches a steady state at T_s.

A second numerical technique to compute storage and loss moduli is based on the theoretical formulae eqn.(5.17) and eqn.(5.18). The loss modulus is directly given by discretization of eqn.(5.18), i.e.

$$E'' = \frac{R^2 H_0 \omega}{8 \sum_{i=0}^{n} m_i(\phi) \Delta X}. \tag{5.22}$$

For the storage modulus, we use a differential method in terms of $\Delta g_i, \quad i = 0, 1, 2, ..., N$

to carry out the numerical derivative in eqn.(5.17). For simplicity, let $S_e = \frac{\int_0^{H_0} m(\phi)\hat{\mu}(\phi)\mathrm{d}z}{\int_0^{H_0} m(\phi)\mathrm{d}z}$, then the storage modulus is given by

$$E' = H_0 \frac{\Delta S_e}{\Delta h} = H_0 \frac{\sum_{i=0}^{N} \frac{\partial S_e}{\partial g_i} \Delta g_i}{\Delta h}. \tag{5.23}$$

The moduli obtained by the first method will be labeled 'simulation' and those from the second method will be called 'theory' in Fig. 5.4 below. We compared the moduli obtained

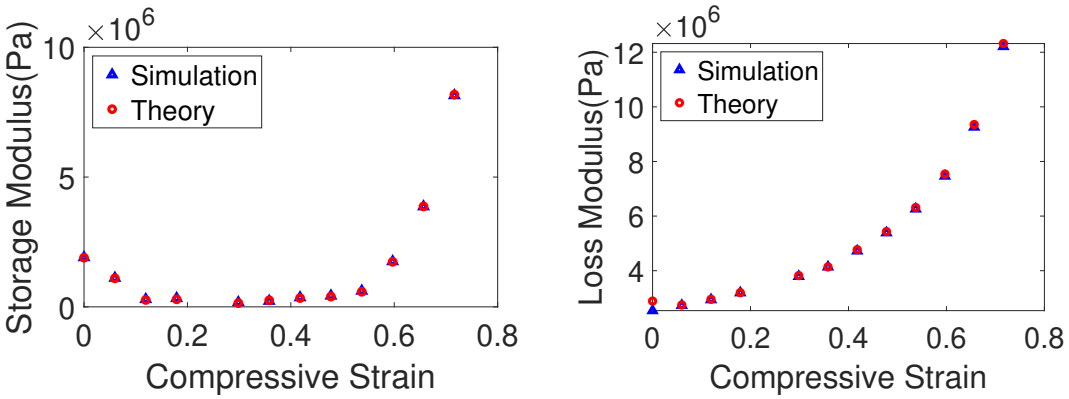

Figure 5.4: The comparison of the (a) storage modulus and (b) loss modulus obtained from two different methods at various compressive strains.

.

by these two methods described above at different compressive strains, with one or no phase transition fronts present in the cylindrical sample in Fig. 5.4. The excellent agreement between the moduli obtained from the two methods indicates that our techniques to compute them are robust.

5.4. Results

5.4.1. Effects of loading and unloading

We first investigate the behavior of storage and loss moduli under one cycle of loading and unloading. As before, we load the cylindrical sample to a certain global compressive strain $\varepsilon = 1 - \frac{H}{H_0}$ until it reaches steady state and extract the storage and loss moduli using the inner product method. The results are shown in Fig. 5.5 as the red markers.

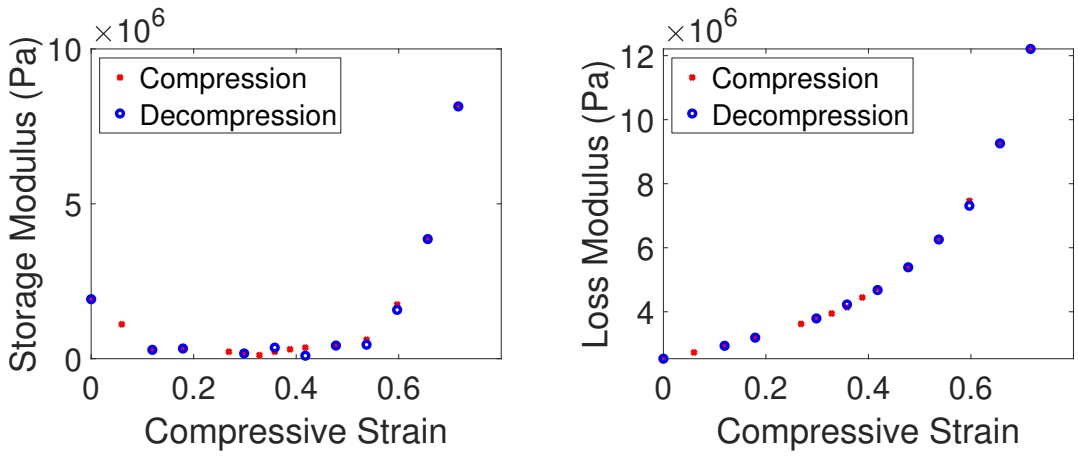

(a) (b)

Figure 5.5: The comparison of (a) storage modulus and (b) loss modulus in loading and unloading as a function of overall compressive strain ε obtained at an oscillation frequency 1Hz. The storage and loss moduli are the same for a given ε irrespective of whether this state was reached while loading or unloading. There is either one or no phase transition front present in the sample for each computation.

.

The storage modulus decreases by one order of magnitude over the region $0 \leq \varepsilon \leq 0.12$. Then, it stays at a plateau over the region $0.12 \leq \varepsilon \leq 0.55$. Then, it increases steeply for $\varepsilon \geq 0.55$. This trend correlates with the progression of a phase transition from rarefied to densified phase of the gel as described in detail in Sun et al[118]. For $\varepsilon < 0.12$ the gel is fully in the rarefied phase and the decrease of storage modulus is due to the change of curvature of the energy well representing the rarefied phase as ε is increased. At larger ε a phase transition front is nucleated at the top plate, which moves to a steady state location $s(\varepsilon)$ such that $0 < s(\varepsilon) < H_0$. In the presence of the phase transition front the gel has an extra degree of freedom to accommodate any change in ε by simply moving the front. As a result, the storage modulus is low and it remains at a plateau until the phase transition front moves downwards and disappears at the bottom plate converting the whole gel into the densified phase. Once the whole sample is converted to the densified phase the storage modulus increases with increasing ε because the curvature of the energy well representing the densified phase increases. The trend in storage modulus seen in Fig. 5.5(a) has also

been observed in experiments on fibrin networks, which suffer a rarefied to densified phase transition under compression[57].

The loss modulus is plotted as a function of ε in Fig. 5.5(b). The loss modulus increases monotonically with ε. This is because it is determined by the permeability m, which decreases as the strain increases.

Next, we unload the sample by decreasing ε in steps. At each ε during unloading we let the sample reach steady state and then perform oscillations around it to extract the storage and loss moduli using the inner product method. The results appear as blue markers in Fig. 5.5. There are no major differences between the moduli obtained during loading and unloading. This is because the steady state stress-strain curve of the sample and the variation of strain as a function of reference position in the sample during loading and unloading are exactly the same in equilibrium and are determined entirely by $\psi_{R,mechanical}$. A graph of the steady state stress-strain curve during loading and unloading appears in the inset of Fig. 5.3(a).

5.4.2. Frequency dependence

Equation(5.16) suggests that the rheological behavior of our phase-transforming gel is like a Kelvin-Voigt visco-elastic material. Here we will show that this indeed holds true in the plateau region, which coincides with the presence of a propagating phase transition front. First, we generate equilibrium configurations of the gel with phase transition fronts at different locations s in the reference configuration with $0 < s < H_0$. These equilibria correspond to a constant compressive stress. The strains corresponding to this stress in the rarefied phase and densified phase appear on the two sides of the phase transition front and the location of the phase transition front is determined by the overall ε; a change in s corresponds to a change in ε. Having chosen an equilibrium state of the gel like this we conduct oscillations around it at various frequencies. The moduli are obtained by the inner product method and the results are shown in Fig. 5.6.

The storage moduli appear in Fig. 5.6(a) for three different frequencies and they all show a

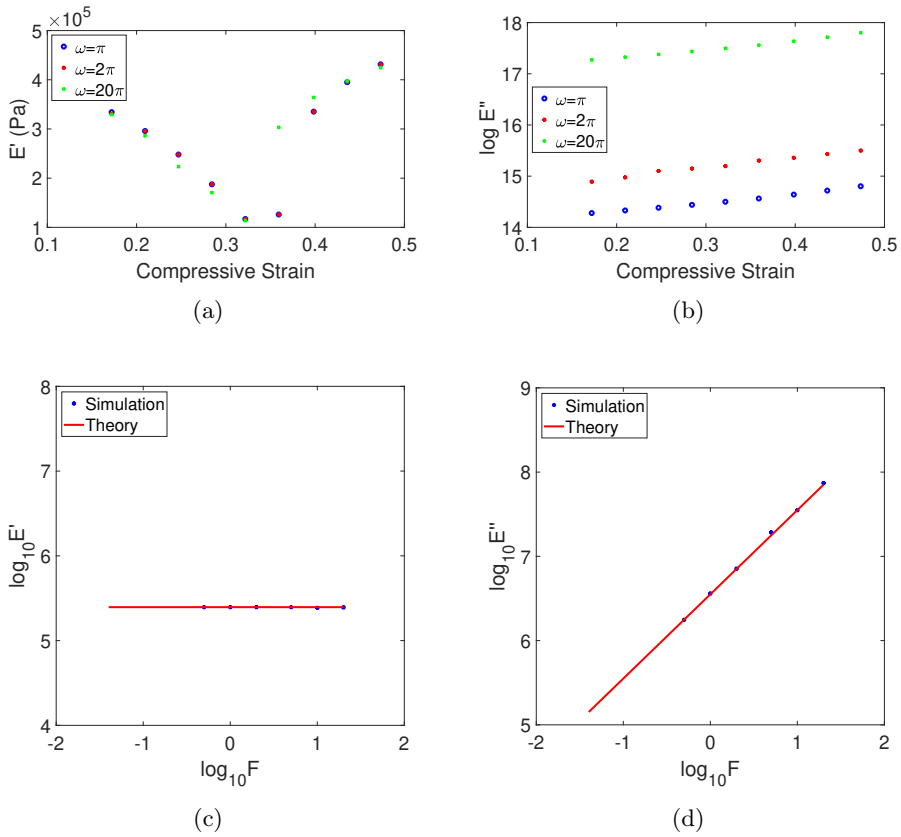

Figure 5.6: The frequency dependence of the (a) storage modulus and (b) loss modulus at various compressive strains. The independence of storage modulus and the linear dependence of loss modulus on frequency is demonstrated in (c) and (d) correspondingly for a fixed overall $\varepsilon = 0.25$. In log-log plot the logarithm of storage modulus $\log_{10} E'$ remains almost a constant, and the logarithm of loss modulus $\log_{10} E''$ is linear in the logarithm of frequency $\log_{10} F$ with slope 1. The trends seen here are reminiscent of a Kelvin-Voigt visco-elastic material.

similar trend – they decrease as the phase transition front propagates and reaches a minimum when $s = \frac{H_0}{2}$, then increase again. This trend is observed also in experiments on fibrin gels as shown in Liang *et al.* (see their Fig. 8 in [52]) although there is no discussion about the presence of a minimum in that paper. The storage moduli show no significant differences for different frequencies. On the other hand, the loss moduli shown in Fig. 5.6(b) increase dramatically as frequency increases and as ε increases. This is because more energy must be dissipated to move fluid through the growing densified phase of the gel. In fact, the storage modulus is independent of frequency as seen in Fig. 5.6(c), and the loss modulus

is proportional to the frequency in the range tested as seen in Fig. 5.6(d). These moduli correspond to $\varepsilon = 0.25$, so that both rarefied and densified phases are present. In the pure rarefied or densified phase, the storage and loss moduli can be predicted using eqn.(5.17) and eqn.(5.18) respectively, by assuming a uniform equilibrium stretch through the sample and small amplitude of oscillation. For example, at $\varepsilon = 0.06$ when the gel is entirely in rarefied phase $E'(F) = 1.1108 \times 10^6$ Pa and $E''(F) = 2.7296 \times 10^6 F$ Pa; at $\varepsilon = 0.66$ when the gel is entirely in densified phase $E'(F) = 3.8676 \times 10^6$ Pa and $E''(F) = 9.2589 \times 10^6 F$ Pa. These results from numerical simulations and analysis are in agreement with our predictions in eqn.(5.16), which align with those for a Kelvin-Voigt visco-elastic material.

5.4.3. Effects of two interfaces

Finally, we address a conundrum that was reported in Liang *et al.*[52] without explanation. The experiments of Liang *et al.* showed that both storage and loss moduli of fibrin gels are significantly different for a given overall strain depending on whether this overall strain is reached during loading or unloading [52]. Recall from our predictions in Fig. 5.5 that the storage and loss moduli are the same at a given overall strain in steady state whether we reach that strain while loading or unloading. In the numerical experiments of Fig. 5.5 there was only one phase transition front. Here we show that multiple fronts could be a cause for the differences in rheological moduli in loading and unloading.

We have pointed out earlier that a given overall strain ε in the plateau region of the stress-strain curve corresponds to a unique fraction of the rarefied and densified phases; this is irrespective of the number of phase transition fronts present. Thus, we can achieve a given overall strain by having two interfaces in a cylindrical sample at steady state. In fact, two propagating fronts were demonstrated in Sun *et al.* [118] during unloading a fibrous gel sample. This second interface was nucleated from the top (moving) plate and moved downwards even as the front produced during loading remained stationary near the bottom plate. Keeping this in mind, we started with an initial condition with two fronts, performed oscillatory experiments, and calculated the storage and loss moduli using the second method

(which we called 'theory' in Fig. 5.5). The results appear in Fig. 5.7 as a function of the overall strain ε. In the presence of two fronts the storage moduli are lower than those when only one interface is present. There is no significant difference in the loss moduli in the presence of one or two interfaces. These results demonstrate that the rheological properties of fibrous gels depend not just on the material, overall strain and frequency, but also on other parameters such as the number of phase transition fronts present in the sample.

While we have found a possible cause for the lack of reversibility in loading/unloading seen in experiments on fibrin gels, there still remains a gap in our understanding. The experimental data from Liang *et al.* [52] re-plotted as Fig. 5.1(b) shows that the storage moduli during unloading are larger than those during loading. This would mean that two interfaces are present during loading and one interface during unloading, based on Fig. 5.7. This is the opposite of the result in Sun *et al.* [118], which showed one interface during loading and two during unloading. Experiments have definitely revealed the presence of a front during loading, but confocal images of multiple fronts during loading or unloading have yet to be investigated. All of these points suggest that a more thorough study is needed (a) to determine the number of interfaces seen in experiments, and (b) to incorporate mechanisms for micro-structural evolution in theoretical models. These studies could potentially reveal dissipation mechanisms that elude simple rheological measurements.

5.5. Conclusion

In this work we use a chemo-elastic continuum model to study the rheological behavior of fibrous gels. We obtain the storage and loss modulus of fibrous gels by performing small amplitude oscillatory compression around various levels of deformation. The dynamic response reveals a Kelvin-Voigt visco-elastic response, where the cause of dissipation is the liquid flow through pores of the gel. A plateau can be found in the storage modulus curve as the phase transition front moves through the sample. Our result for the storage modulus is similar to the trends seen in experiments [52, 57, 137]. On the other hand, the loss modulus is unaffected by the phase transition and increases monotonically during

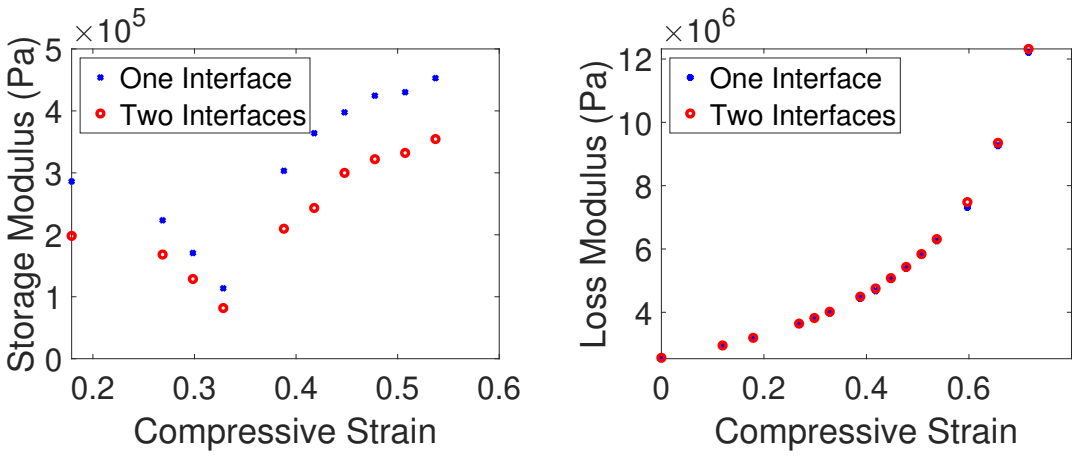

(a) (b)

Figure 5.7: The comparison of storage and loss moduli in the presence of one and two phase transition fronts. (a) storage modulus and (b) loss modulus at various compressive strains. In the case when there are two fronts, the storage modulus is lower while the overall trend is similar to the one front case.

.

compression. Our result for the loss modulus is different from that observed in experiments because we perform oscillations in compression (which changes the volume) where as the experiments perform oscillations in shear (which does not change volume). As such the loss modulus in our computations characterizes dissipation due to fluid flow, whereas the loss modulus in experiments [52, 57] corresponds to friction of the fibers with each other and the fluid. We have shown that when only a single phase transition front is present in the sample then there are no major differences in storage and loss moduli between loading and unloading. However, the storage moduli decrease significantly when more than one interface appears. The loss modulus does not change with the number of interfaces, or equivalently the loading/unloading. To better capture the behavior of the loss modulus shear oscillation is needed together with other mechanisms of dissipation in the constitutive model. We leave this to future work.

CHAPTER 6

Conclusion

In this thesis, we study the stress-induced phase transitions in rod-like macromolecules and fibrin gels. We base our theoretical framework on a continuum theory [17]. In this theory the strain energy function that characterizes the thermoelasticity of the material is assumed to be non-convex in the deformation gradient; multiple local minima represent different phases of the material. We then implement different strategies in solving the continuum equations for macromolecules and fibrous gels, respectively.

In chapter 2 the kinetic relation for a phase boundary in a bistable bar immersed in a heat bath is obtained by the method of energy balance. A series of Langevin dynamic simulations at various pulling velocities and bath temperatures are performed on a mass-spring chain with bistable springs. Although the microscopic motion of the phase boundary is jerky due to thermal fluctuations and discreteness of the mass-spring chain, we could still find a relation between the homogenized phase boundary velocity and an average driving force. The stick-slip type kinetic relation that we found shares some similarity to those obtained for phase boundary propagation through a row of imperfections [15] and heterogeneous materials [95], but with a temperature dependence of the kinetics that had not been seen before. The form of the slip part of our kinetic relation follows a power law, which is different from the Arrhenius form that may be expected for thermally activated phase boundary motion [17]. A direct inference of the stick-slip kinetics is that force-extension relations are different for the loading and the unloading paths, which leads to hysteresis. We also clarify the role and magnitude of thermal fluctuations in the force-extension response of our bistable bar. The kinetic law derived here may be applicable to the mechanical response of macromolecules, such as coiled-coil proteins that rely on force-induced structural transitions for their function.

In chapter 3, we combine the Langevin dynamics simulations described in chapter 2 it with fluctuation theorems to extract equilibrium and non-equilibrium information, such as free

energy change and dissipation. We show a connection between transport coefficients and a fluctuation theorem through the establishment of a Green-Kubo formula. Then, we carry out a series of mass-spring simulations using over-damped Langevin dynamics. In the linear springs case, we find a perfect match between analytical estimates of free energy change during a process and predictions of the Jarzynski equality [36] and Crook's fluctuation theorem [37]. For non-linear springs characterized by double-well potentials, we notice large discrepancy between the free energy change estimated by analytical formulae and those predicted by fluctuation theorems. Further research is needed for obtaining useful equilibrium and kinetic information using fluctuation theorems in systems with complicated dissipation mechanisms. This will require future investigations to, for example, better capture the tail of the work distribution [114], better model multiphysics processes (such as, dissipation due to fluid drag and phase transition) [116], and improve or use other fluctuation theorems that are applicable to coexisting states [148].

In chapter 4, we use a chemo-elastic continuum model to study fibrous gels such as blood clots. We implement a double-well energy landscape for the solid network to capture the co-existence of a densified phase and a rarefied phase of the network over a range of stresses. Two phases of the network are possible because under compression the fibers can buckle and the network transforms from a rarefied phase to a densified phase. Often, a moving interface separates the rarefied and densified phases of a compressed network. During compression, the volume of the gel reduces dramatically, accompanied by release of fluid. The motion of the interface is controlled by the flow of the fluid in the gel this case and thus a kinetic relation for the motion of the interface is not required. This is different from an earlier continuum model of these gels that was based on the Abeyaratne-Knowles theory of phase transitions[52] in continua which did accounted for the effects of fluid in a rudimentary way. The chemo-elastic model studied here is also capable of capturing several features that are observed in experiments. A feature of the work here is that finite element calculations are not required to obtain experimentally relevant results, under appropriate assumptions that reduce the problem to one dimensional or axially symmetric. Yet, a fully three dimensional

continuum calculation can be done using finite elements to confirm and justify the theory, and we leave this to future work.

In chapter 5, we further develop the chemo-elastic continuum model to study the rheological behavior of fibrous gels. The storage and loss modulus of fibrous gels are obtained by performing small amplitude oscillatory compression around various levels of deformation. We found a Kelvin-Voigt visco-elastic response, where the main source of dissipation is the liquid flow through pores of the gel. A plateau can be found in the storage modulus curve as the phase transition front moves through the sample. Our result for the storage modulus is similar to the trends seen in experiments [52, 57, 137]. On the other hand, the loss modulus is unaffected by the phase transition and increases monotonically during compression. This difference resulted from the compressive oscillation instead of shear oscillation as was performed by experiments. To better capture the behavior of the loss modulus, shear oscillation together with other mechanisms of dissipation in the constitutive model is needed in further works.

In summary, we have studied two different problems involving phase transitions, one molecular and the other macroscopic. We use both statistical mechanical and continuum mechanical methods and focus on dissipation in the loading/unloading response. Some new findings are reported in this thesis, but these lead to questions that must be tackled in future research.

BIBLIOGRAPHY

[1] D. A. Porter, K. E. Easterling, Phase transformations in metals and alloys (revised reprint), CRC press, 2009.

[2] A. Cavalleri, C. Tóth, C. W. Siders, J. Squier, F. Ráksi, P. Forget, J. Kieffer, Femtosecond structural dynamics in vo 2 during an ultrafast solid-solid phase transition, Physical review letters 87 (23) (2001) 237401.

[3] Y. Jiang, E. Ding, G. Li, Study on transition characteristics of peg/cda solid–solid phase change materials, Polymer 43 (1) (2002) 117–122.

[4] A. Richter, S. Howitz, D. Kuckling, K.-F. Arndt, Influence of volume phase transition phenomena on the behavior of hydrogel-based valves, Sensors and Actuators B: Chemical 99 (2-3) (2004) 451–458.

[5] W. D. Callister, et al., Fundamentals of materials science and engineering, Vol. 471660817, Wiley London, 2000.

[6] L. Tskhovrebova, J. Trinick, J. Sleep, R. Simmons, Elasticity and unfolding of single molecules of the giant muscle protein titin, Nature 387 (1997) 308–12.

[7] M. Rief, M. Gautel, F. Oesterhelt, J. Fernandez, H. Gaub, Reversible unfolding of individual titin immunoglobulin domains by afm, Science 276 (1997) 1109–12.

[8] A. Oberhauser, P. Hansma, M. Carrion-Vazquez, J. Fernandez, Stepwise unfolding of titin under force-clamp atomic force microscopy, Proc. Natl. Acad. Sci. 98 (2001) 468–72.

[9] Y. Zhang, F. Lu, D. van der Lelie, O. Gang, Continuous phase transformation in nanocube assemblies, Physical Review Letters 107 (13) (2011) 135701.

[10] J. E. Spanier, A. M. Kolpak, J. J. Urban, I. Grinberg, L. Ouyang, W. S. Yun, A. M. Rappe, H. Park, Ferroelectric phase transition in individual single-crystalline batio3 nanowires, Nano letters 6 (4) (2006) 735–739.

[11] J. L. Silverberg, J.-H. Na, A. A. Evans, B. Liu, T. C. Hull, C. D. Santangelo, R. J. Lang, R. C. Hayward, I. Cohen, Origami structures with a critical transition to bistability arising from hidden degrees of freedom, Nature materials 14 (4) (2015) 389–393.

[12] V. Brunck, F. Lechenault, A. Reid, M. Adda-Bedia, Elastic theory of origami-based metamaterials, Physical Review E 93 (3) (2016) 033005.

[13] J. L. Ericksen, Equilibrium of bars, Journal of elasticity 5 (3) (1975) 191–201.

[14] R. Abeyaratne, C. Chu, R. D. James, Kinetics of materials with wiggly energies: Theory and application to the evolution of twinning microstructures in a cu-al-ni shape memory alloy, Philosophical Magazine A 73 (2) (1996) 457–497.

[15] R. Abeyaratne, C. Chu, R. D. James, Kinetics of materials with wiggly energies: theory and application to the evolution of twinning microstructures in a cu-al-ni shape memory alloy, Philosophical Magazine A 73 (2) (1996) 457–497.

[16] R. Abeyaratne, J. K. Knowles, On the driving traction acting on a surface of strain discontinuity in a continuum, Journal of the Mechanics and Physics of Solids 38 (3) (1990) 345–360.

[17] R. Abeyaratne, J. K. Knowles, Evolution of Phase Transitions: A Continuum Theory, New York: Cambridge University Press, 2006.

[18] P. K. Purohit, K. Bhattacharya, Dynamics of strings made of phase-transforming materials, Journal of the Mechanics and Physics of Solids 51 (3) (2003) 393–424.

[19] L. Truskinovsky, A. Vainchtein, Kinetics of martensitic phase transitions: lattice model, SIAM J. APPL. Math 66 (2) (2005) 533–53.

[20] Y. R. Efendiev, L. Truskinovsky, Thermalization of a driven bi-stable fpu chain, Continuum Mechanics and Thermodynamics 22 (2010) 679–98.

[21] M. Caruel, L. Truskinovsky, Bi-stability resistant to fluctuations, Journal of the Mechanics and Physics of Solids 109 (2017) 117–141.

[22] G. Puglisi, L. Truskinovsky, Thermodynamics of rate-independent plasticity, Journal of the Mechanics and Physics of Solids 53 (3) (2005) 655–679.

[23] A. K. Efremov, R. S. Winardhi, J. Yan, Theoretical methods for studying dna structural transitions under applied mechanical constraints, Polymers 9 (2) (2017) 74.

[24] A. Marin-Gonzalez, J. Vilhena, R. Perez, F. Moreno-Herrero, Understanding the mechanical response of double-stranded dna and rna under constant stretching forces using all-atom molecular dynamics, Proceedings of the National Academy of Sciences 114 (27) (2017) 7049–7054.

[25] A. Zhmurov, O. Kononova, R. I. Litvinov, R. I. Dima, V. Barsegov, J. W. Weisel, Mechanical transition from α-helical coiled coils to β-sheets in fibrin (ogen), Journal of the American Chemical Society 134 (50) (2012) 20396–20402.

[26] D. Collin, F. Ritort, C. Jarzynski, S. B. Smith, I. Tinoco, C. Bustamante, Verification of the crooks fluctuation theorem and recovery of rna folding free energies, Nature 437 (7056) (2005) 231–234.

[27] K. A. Minin, A. Zhmurov, K. A. Marx, P. K. Purohit, V. Barsegov, Dynamic transition from α-helices to β-sheets in polypeptide coiled-coil motifs, Journal of the American Chemical Society 139 (45) (2017) 16168–16177.

[28] A. Torres-Sánchez, J. M. Vanegas, P. K. Purohit, M. Arroyo, Combined molecular/continuum modeling reveals the role of friction during fast unfolding of coiled-coil proteins, Soft matter (2019).

[29] R. Abeyaratne, S. Vedantam, Propagation of a front by kink motion, in: IUTAM Symposium on Variations of Domain and Free-Boundary Problems in Solid Mechanics, Springer, 1999, pp. 77–84.

[30] R. Bhattacharya, V. Patrangenaru, et al., Large sample theory of intrinsic and extrinsic sample means on manifolds, The Annals of Statistics 31 (1) (2003) 1–29.

[31] W. Atkinson, N. Cabrera, Motion of a frenkel—kontorowa dislocation in a one-dimensional crystal, Phys. Rev. 138 (1965) A763–A766.

[32] V. L. Popov, J. Gray, Prandtl-tomlinson model: History and applications in friction, plasticity, and nanotechnologies, ZAMM-Journal of Applied Mathematics and Mechanics/Zeitschrift für Angewandte Mathematik und Mechanik 92 (9) (2012) 683–708.

[33] D. D. Tommasi, N. Millardi, G. Puglisi, G. Saccomandi, An energetic model for macromolecules unfolding in stretching experiments, Journal of The Royal Society Interface 10 (88) (2013) 20130651.

[34] G. Bochkov, Y. E. Kuzovlev, General theory of thermal fluctuations in nonlinear systems, Zh. Eksp. Teor. Fiz 72 (1977) 238–243.

[35] D. J. Evans, E. G. D. Cohen, G. P. Morriss, Probability of second law violations in shearing steady states, Physical review letters 71 (15) (1993) 2401.

[36] C. Jarzynski, Nonequilibrium equality for free energy differences, Physical Review Letters 78 (14) (1997) 2690.

[37] G. E. Crooks, Nonequilibrium measurements of free energy differences for microscopically reversible markovian systems, Journal of Statistical Physics 90 (5) (1998) 1481–1487.

[38] J. Liphardt, S. Dumont, S. B. Smith, I. Tinoco Jr, C. Bustamante, Equilibrium information from nonequilibrium measurements in an experimental test of jarzynski's equality, Science 296 (5574) (2002) 1832–1835.

[39] F. Douarche, S. Ciliberto, A. Petrosyan, I. Rabbiosi, An experimental test of the jarzynski equality in a mechanical experiment, EPL (Europhysics Letters) 70 (5)

(2005) 593.

[40] P. Visco, A. Puglisi, A. Barrat, E. Trizac, F. Van Wijland, Fluctuations of power injection in randomly driven granular gases, Journal of statistical Physics 125 (3) (2006) 533–568.

[41] K. Y. Lee, D. J. Mooney, Hydrogels for tissue engineering, Chemical reviews 101 (7) (2001) 1869–1880.

[42] J. Li, D. J. Mooney, Designing hydrogels for controlled drug delivery, Nature Reviews Materials 1 (12) (2016) 1–17.

[43] A. J. Engler, S. Sen, H. L. Sweeney, D. E. Discher, Matrix elasticity directs stem cell lineage specification, Cell 126 (4) (2006) 677–689.

[44] G. Gerlach, K.-F. Arndt, Hydrogel sensors and actuators: engineering and technology, Vol. 6, Springer Science & Business Media, 2009.

[45] O. Chaudhuri, L. Gu, D. Klumpers, M. Darnell, S. A. Bencherif, J. C. Weaver, N. Huebsch, H.-p. Lee, E. Lippens, G. N. Duda, et al., Hydrogels with tunable stress relaxation regulate stem cell fate and activity, Nature materials 15 (3) (2016) 326–334.

[46] E. E. Leonhardt, N. Kang, M. A. Hamad, K. L. Wooley, M. Elsabahy, Absorbable hemostatic hydrogels comprising composites of sacrificial templates and honeycomb-like nanofibrous mats of chitosan, Nature communications 10 (1) (2019) 1–9.

[47] S. A. Chester, L. Anand, A coupled theory of fluid permeation and large deformations for elastomeric materials, J. Mech. Phys. Solids 58 (11) (2010) 1879 – 1906.

[48] S. A. Chester, L. Anand, A thermo-mechanically coupled theory for fluid permeation in elastomeric materials: application to thermally responsive gels, J. Mech. Phys. Solids 59 (10) (2011) 1978–2006.

[49] S. A. Chester, C. V. Di Leo, L. Anand, A finite element implementation of a coupled diffusion-deformation theory for elastomeric gels, Int. J. Solids Struct. 52 (2015) 1–18.

[50] W. Hong, X. Zhao, J. Zhou, Z. Suo, A theory of coupled diffusion and large deformation in polymeric gels, J. Mech. Phys. Solids 56 (5) (2008) 1779–1793.

[51] W. Hong, Z. Liu, Z. Suo, Inhomogeneous swelling of a gel in equilibrium with a solvent and mechanical load, International Journal of Solids and Structures 46 (17) (2009) 3282–3289.

[52] X. Liang, I. Chernysh, P. K. Purohit, J. W. Weisel, Phase transitions during compression and decompression of clots from platelet-poor plasma, platelet-rich plasma and

whole blood, Acta Biomater. 60 (2017) 275–290.

[53] Z. Shoujing, L. Zishun, Phase transition of temperature-sensitive hydrogel under mechanical constraint, Journal of Applied Mechanics 85 (2) (2018).

[54] X. Wang, H. J. Kim, C. Wong, C. Vepari, A. Matsumoto, D. L. Kaplan, Fibrous proteins and tissue engineering, Materials today 9 (12) (2006) 44–53.

[55] J. W. Weisel, The mechanical properties of fibrin for basic scientists and clinicians, Biophysical chemistry 112 (2-3) (2004) 267–276.

[56] S. Hosseini, W. Wilson, K. Ito, C. Van Donkelaar, A numerical model to study mechanically induced initiation and progression of damage in articular cartilage, Osteoarthritis and cartilage 22 (1) (2014) 95–103.

[57] O. V. Kim, X. Liang, R. I. Litvinov, J. W. Weisel, M. S. Alber, P. K. Purohit, Foam-like compression behavior of fibrin networks, Biomech. Model. Mechan. 15 (1) (2016) 213–228.

[58] C. P. Broedersz, F. C. MacKintosh, Modeling semiflexible polymer networks, Reviews of Modern Physics 86 (3) (2014) 995.

[59] D. T. Chen, Q. Wen, P. A. Janmey, J. C. Crocker, A. G. Yodh, Rheology of soft materials, Annu. Rev. Condens. Matter Phys. 1 (1) (2010) 301–322.

[60] C. Tekog, L. Gibson, T. Pardoen, P. Onck, et al., Size effects in foams: Experiments and modeling, Progress in Materials Science 56 (2) (2011) 109–138.

[61] C. Sun, P. K. Purohit, Stick-slip kinetics in a bistable bar immersed in a heat bath, International journal of solids and structures 180 (2019) 205–220.

[62] J. Gore, Z. Bryant, M. Nollmann, M. Le, N. Cozzarelli, C. Bustamante, Dna overwinds when stretched, Nature 442 (2006) 836–39.

[63] S. Koster, D. Weitz, R. Goldman, U. Aebi, H. Herrmann, Intermediate filament mechanics in vitro and in the cell: from coiled coils to filaments, fibers and networks, Curr. Opin. Cell Biol. 32 (2015) 82–91.

[64] J. Block, H. Witt, A. Candelli, E. J. G. Peterman, G. J. L. Wuite, A. Janshoff, S. Köster, Nonlinear loading-rate-dependent force response of individual vimentin intermediate filaments to applied strain, Phys. Rev. Lett. 118 (2017) 048101.

[65] C. Peng, Y. Zhong, Y. Lu, S. Narayanan, T. Zhu, L. J, Strain rate dependent mechanical properties in single crystal nickel nanowires, Appl. Phys Lett. 14 (2015) 707–13.

[66] G. A. King, P. Gross, U. Bockelmann, M. Modesti, G. J. Wuite, E. J. Peterman, Revealing the competition between peeled ssdna, melting bubbles, and s-dna during dna overstretching using fluorescence microscopy, Proceedings of the National Academy of Sciences 110 (10) (2013) 3859–3864.

[67] J. van Mameren, P. Gross, G. Farge, P. Hooijman, M. Modesti, M. Falkenberg, G. J. Wuite, E. J. Peterman, Unraveling the structure of dna during overstretching by using multicolor, single-molecule fluorescence imaging, Proceedings of the National Academy of Sciences (2009) pnas–0904322106.

[68] Z. Qin, M. J. Buehler, Molecular dynamics simulation of the α-helix to β-sheet transition in coiled protein filaments: Evidence for a critical filament length scale, Physical Review Letters 104 (19) (2010) 198304.

[69] M. Rief, M. Gautel, F. Oesterhelt, J. M. Fernandez, H. E. Gaub, Reversible unfolding of individual titin immunoglobulin domains by afm, science 276 (5315) (1997) 1109–1112.

[70] D. De Tommasi, N. Millardi, G. Puglisi, G. Saccomandi, An energetic model for macromolecules unfolding in stretching experiments, Journal of The Royal Society Interface 10 (88) (2013) 20130651.

[71] X. Zhang, H. Chen, S. Le, I. Rouzina, P. S. Doyle, J. Yan, Revealing the competition between peeled ssdna, melting bubbles, and s-dna during dna overstretching by single-molecule calorimetry, Proceedings of the National Academy of Sciences 110 (10) (2013) 3865–3870.

[72] T. Bornschlögl, M. Rief, Single molecule unzipping of coiled coils: sequence resolved stability profiles, Physical Review Letters 96 (11) (2006) 118102.

[73] R. Raj, P. K. Purohit, Phase boundaries as agents of structural change in macromolecules, Journal of the Mechanics and Physics of Solids 59 (10) (2011) 2044–2069.

[74] R. Raj, P. K. Purohit, Moving interfaces in rod-like macromolecules, EPL (Europhysics Letters) 91 (2) (2010) 28003.

[75] H. Guo, K. Chen, Y. Oh, K. Wang, C. Dejoie, S. A. Syed Asif, O. L. Warren, Z. W. Shan, J. Wu, A. M. Minor, Mechanics and dynamics of the strain-induced m1–m2 structural phase transition in individual vo2 nanowires, Nano Letters 11 (8) (2011) 3207–3213.

[76] Q. Zhao, P. K. Purohit, Extracting a kinetic relation from the dynamics of a bistable chain, Modelling and Simulation in Materials Science and Engineering 22 (4) (2014) 045004.

[77] I. Benichou, S. Givli, Rate dependent response of nanoscale structures having a multiwell energy landscape, Physical review letters 114 (9) (2015) 095504.

[78] I. Benichou, Y. Zhang, O. K. Dudko, S. Givli, The rate dependent response of a bistable chain at finite temperature, Journal of the Mechanics and Physics of Solids 95 (2016) 44–63.

[79] S. L. Thomas, K. Chen, J. Han, P. K. Purohit, D. J. Srolovitz, Reconciling grain growth and shear-coupled grain boundary migration, Nature communications 8 (1) (2017) 1764.

[80] A. Dittmore, K. C. Neuman, Evidence for a solenoid phase of supercoiled dna, arXiv preprint arXiv:1804.06442 (2018).

[81] Y. Min, P. K. Purohit, Discontinuous growth of dna plectonemes due to atomic scale friction, Soft matter 14 (37) (2018) 7759–7770.

[82] G. Puglisi, L. Truskinovsky, Thermodynamics of rate-independent plasticity, Journal of the Mechanics and Physics of Solids 53 (3) (2005) 655 – 679.

[83] D. D. Tommasi, G. Puglisi, G. Saccomandi, Multiscale mechanics of macromolecular materials with unfolding domains, Journal of the Mechanics and Physics of Solids 78 (2015) 154 – 172.

[84] V. Ivanov, Y. Mishin, Dynamics of grain boundary motion coupled to shear deformation: An analytical model and its verification by molecular dynamics, Physical Review B 78 (6) (2008) 064106.

[85] Y.-c. Fung, Foundations of solid mechanics (1965).

[86] Q. Zhao, P. K. Purohit, (adiabatic) phase boundaries in a bistable chain with twist and stretch, Journal of the Mechanics and Physics of Solids 92 (2016) 176–194.

[87] R. K. Pathria, P. D. Beale, Statistical Mechanics, New York, 2011.

[88] G. N. Milstein, Y. M. Repin, M. V. Tretyakov, Symplectic integration of hamiltonian systems with additive noise, SIAM J. Numer. Anal. 39 (6) (2002) 2066–88.

[89] K. Minin, A. Zhmurov, K. Marx, P. Purohit, V. Barsegov, Dynamic transition from α-helices to β-sheets in polypeptide superhelices, J. Am. Chem. Soc. 139 (45) (2017) 16168–77.

[90] F. Incropera, D. Dewitt, Fundamentals of Heat and Mass Transfer, New York, 1996.

[91] G. Puglisi, Hysteresis in multi-stable lattices with non-local interactions, Journal of

the Mechanics and Physics of Solids 54 (10) (2006) 2060 – 2088.

[92] L. Truskinovsky, A. Vainchtein, Peierls-nabarro landscape for martensitic phase transitions, Phys. Rev. B 67 (2003) 172103.

[93] G. Florio, G. Puglisi, Unveiling the influence of device stiffness in single macromolecule unfolding, Scientific Reports 9 (March 2019).

[94] N. V. KAMPEN, Stochastic Processes in Physics and Chemistry, third edition Edition, Elsevier, 2007.

[95] K. Bhattacharya, Phase boundary propagation in a heterogeneous body, Proceedings: Mathematical, Physical and Engineering Sciences (1999) 757–766.

[96] D. T. Gillespie, Markov processes: an introduction for physical scientists, Elsevier, 1991.

[97] Q. Zhao, P. K. Purohit, Phase boundaries with discontinuous stretch and twist in dna, International Journal of Solids and Structures 94 (2016) 238–246.

[98] M. Doi, S. F. Edwards, The theory of polymer dynamics, Vol. 73, oxford university press, 1988.

[99] J. H. Weiner, Statistical mechanics of elasticity, Courier Corporation, 2012.

[100] D. Stoeckel, W. Yu, Superelastic ni-ti wire, Wire Journal International (1992) 45–50.

[101] C. C. A. Miserez, S. Wasko, J. Waite, Kinetics of materials with wiggly energies: Theory and application to the evolution of twinning microstructures in a cu-al-ni shape memory alloy, Nature Materials 8 (2) (2009) 910–916.

[102] S. Huang, C. Sun, P. K. Purohit, C. Reina, Harnessing fluctuation theorems to discover free energy and dissipation potentials from non-equilibrium data, Journal of the Mechanics and Physics of Solids 149 (2021) 104323.

[103] G. Gallavotti, E. G. D. Cohen, Dynamical ensembles in nonequilibrium statistical mechanics, Physical review letters 74 (14) (1995) 2694.

[104] L. C. Evans, Graduate studies in mathematics (1998).

[105] G. Hummer, A. Szabo, Free energy reconstruction from nonequilibrium single-molecule pulling experiments, Proceedings of the National Academy of Sciences 98 (7) (2001) 3658–3661.

[106] T. Hatano, S.-i. Sasa, Steady-state thermodynamics of langevin systems, Physical

review letters 86 (16) (2001) 3463.

[107] U. M. B. Marconi, A. Puglisi, L. Rondoni, A. Vulpiani, Fluctuation–dissipation: response theory in statistical physics, Physics reports 461 (4-6) (2008) 111–195.

[108] C. Jarzynski, Equalities and inequalities: Irreversibility and the second law of thermodynamics at the nanoscale, Annu. Rev. Condens. Matter Phys. 2 (1) (2011) 329–351.

[109] U. Seifert, Stochastic thermodynamics, fluctuation theorems and molecular machines, Reports on progress in physics 75 (12) (2012) 126001.

[110] R. Klages, W. Just, C. Jarzynski, H. Schuster, Nonequilibrium Statistical Physics of Small Systems: Fluctuation Relations and Beyond, Reviews of Nonlinear Dynamics and Complexity, Wiley, 2013.

[111] C. Jarzynski, Diffusion equation for energy in ergodic adiabatic ensembles, Physical Review A 46 (12) (1992) 7498.

[112] T. Speck, U. Seifert, Integral fluctuation theorem for the housekeeping heat, Journal of Physics A: Mathematical and General 38 (34) (2005) L581.

[113] M. E. Gurtin, E. Fried, L. Anand, The mechanics and thermodynamics of continua, Cambridge University Press, 2010.

[114] M. A. Mohamad, T. P. Sapsis, Sequential sampling strategy for extreme event statistics in nonlinear dynamical systems, Proceedings of the National Academy of Sciences 115 (44) (2018) 11138–11143.

[115] X. Li, N. Dirr, P. Embacher, J. Zimmer, C. Reina, Harnessing fluctuations to discover dissipative evolution equations, Journal of the Mechanics and Physics of Solids 131 (2019) 240–251.

[116] A. Montefusco, M. A. Peletier, H. C. Öttinger, A framework of nonequilibrium statistical mechanics. ii. coarse-graining, Journal of Non-Equilibrium Thermodynamics 46 (1) (2021) 15–33.

[117] A. Alemany, A. Mossa, I. Junier, F. Ritort, Experimental free-energy measurements of kinetic molecular states using fluctuation theorems, Nature Physics 8 (9) (2012) 688–694.

[118] C. Sun, I. N. Chernysh, J. W. Weisel, P. K. Purohit, Fibrous gels modelled as fluid-filled continua with double-well energy landscape, Proc. Roy. Soc. London A 476 (2244) (2020) 20200643.

[119] J.-P. Collet, H. Shuman, R. E. Ledger, S. Lee, J. W. Weisel, The elasticity of an

individual fibrin fiber in a clot, PNAS 102 (26) (2005) 9133–9137.

[120] T. Novak, B. Seelbinder, C. M. Twitchell, C. C. van Donkelaar, S. L. Voytik-Harbin, C. P. Neu, Mechanisms and microenvironment investigation of cellularized high density gradient collagen matrices via densification, Adv. Funct. Mater. 26 (16) (2016) 2617–2628.

[121] O. Kim, R. Litvinov, J. Chen, D. Chen, J. Weisel, M. Alber, Compression-induced structural and mechanical changes of fibrin-collagen composites, Matrix Biol. 60 (2017) 141–156.

[122] J.-Y. Sun, X. Zhao, W. R. Illeperuma, O. Chaudhuri, K. H. Oh, D. J. Mooney, J. J. Vlassak, Z. Suo, Highly stretchable and tough hydrogels, Nature 489 (7414) (2012) 133–136.

[123] X. Liang, J. Shin, D. Magagnosc, Y. Jiang, S. J. Park, A. J. Hart, K. Turner, D. S. Gianola, P. K. Purohit, Compression and recovery of carbon nanotube forests described as a phase transition, Int. J. Solids Struct. 122 (2017) 196–209.

[124] L. J. Gibson, M. F. Ashby, Cellular solids: structure and properties, Cambridge university press, 1999.

[125] R. Picu, Mechanics of random fiber networks—a review, Soft Matter 7 (15) (2011) 6768–6785.

[126] C. Van Wyk, 20—note on the compressibility of wool, J. Text. I. Transactions 37 (12) (1946) T285–T292.

[127] S. Toll, Packing mechanics of fiber reinforcements, Polym. Eng. Sci. 38 (8) (1998) 1337–1350.

[128] I. N. Chernysh, R. Spiewak, C. L. Cambor, P. K. Purohit, J. W. Weisel, Structure, mechanical properties, and modeling of cyclically compressed pulmonary emboli, J. Mech. Behav. Biomed. 105 (2020) 103699.

[129] L. R. G. Treloar, The physics of rubber elasticity, Oxford University Press, USA, 1975.

[130] A. E. Ehret, K. Bircher, A. Stracuzzi, V. Marina, M. Zündel, E. Mazza, Inverse poroelasticity as a fundamental mechanism in biomechanics and mechanobiology, Nat. Commun. 8 (1) (2017) 1–10.

[131] A. Stracuzzi, E. Mazza, A. E. Ehret, Chemomechanical models for soft tissues based on the reconciliation of porous media and swelling polymer theories, ZAMM-Z. Angew. Math. Me. 98 (12) (2018) 2135–2154.

[132] M. T. Punter, B. E. Vos, B. M. Mulder, G. H. Koenderink, Poroelasticity of (bio) polymer networks during compression: theory and experiment, Soft Matter 16 (5) (2020) 1298–1305.

[133] N. Bouklas, C. M. Landis, R. Huang, A nonlinear, transient finite element method for coupled solvent diffusion and large deformation of hydrogels, J. Mech. Phys. Solids 79 (2015) 21–43.

[134] C. Sun, P. K. Purohit, Rheology of fibrous gels under compression, Extreme Mechanics Letters (2022).

[135] M. Oyen, Mechanical characterisation of hydrogel materials, International Materials Reviews 59 (1) (2014) 44–59.

[136] A. L. Butcher, C. T. Koh, M. L. Oyen, Systematic mechanical evaluation of electrospun gelatin meshes, Journal of the mechanical behavior of biomedical materials 69 (2017) 412–419.

[137] A. Ed-Daoui, P. Snabre, Poroviscoelasticity and compression-softening of agarose hydrogels, Rheologica Acta 60 (6) (2021) 327–351.

[138] O. V. Kim, R. I. Litvinov, J. W. Weisel, M. S. Alber, Structural basis for the nonlinear mechanics of fibrin networks under compression, Biomaterials 35 (25) (2014) 6739–6749.

[139] R. Lakes, P. Rosakis, A. Ruina, Microbuckling instability in elastomeric cellular solids, Journal of materials science 28 (17) (1993) 4667–4672.

[140] K. Bhattacharya, et al., Microstructure of martensite: why it forms and how it gives rise to the shape-memory effect, Vol. 2, Oxford University Press, 2003.

[141] G. Koenderink, M. Atakhorrami, F. MacKintosh, C. F. Schmidt, High-frequency stress relaxation in semiflexible polymer solutions and networks, Physical review letters 96 (13) (2006) 138307.

[142] A. S. Van Oosten, M. Vahabi, A. J. Licup, A. Sharma, P. A. Galie, F. C. MacKintosh, P. A. Janmey, Uncoupling shear and uniaxial elastic moduli of semiflexible biopolymer networks: compression-softening and stretch-stiffening, Scientific reports 6 (1) (2016) 1–9.

[143] T. Lamer, B. Thomas, D. Curtis, N. Badiei, P. Williams, K. Hawkins, The application of large amplitude oscillatory stress in a study of fully formed fibrin clots, Physics of Fluids 29 (12) (2017) 121606.

[144] N. Badiei, A. Sowedan, D. Curtis, M. Brown, M. Lawrence, A. Campbell, A. Sabra,

P. Evans, J. Weisel, I. Chernysh, et al., Effects of unidirectional flow shear stresses on the formation, fractal microstructure and rigidity of incipient whole blood clots and fibrin gels, Clinical Hemorheology and Microcirculation 60 (4) (2015) 451–464.

[145] M. R. Islam, G. Tudryn, R. Bucinell, L. Schadler, R. Picu, Morphology and mechanics of fungal mycelium, Scientific reports 7 (1) (2017) 1–12.

[146] M. Islam, G. Tudryn, R. Bucinell, L. Schadler, R. Picu, Stochastic continuum model for mycelium-based bio-foam, Materials & Design 160 (2018) 549–556.

[147] T. Komori, M. Itoh, A. Takaku, A model analysis of the compressibility of fiber assemblies, Textile research journal 62 (10) (1992) 567–574.

[148] I. Junier, A. Mossa, M. Manosas, F. Ritort, Recovery of free energy branches in single molecule experiments, Physical review letters 102 (7) (2009) 070602.